

# Robustness of the Inflationary Perturbation Spectrum to Trans-Planckian Physics<sup>1</sup>

A. A. Starobinsky

Research Center for the Early Universe, The University of Tokyo, 113-0033 Tokyo, Japan  
Landau Institute for Theoretical Physics, Russian Academy of Sciences, Moscow, 117334 Russia  
e-mail: alstar@landau.as.ru

Received April 3, 2001

It is inspected whether the predictions of the inflationary scenario regarding the spectra of scalar and tensor perturbations generated by quantum vacuum fluctuations are robust with respect to the modification of the dispersion law for frequencies beyond the Planck scale. For a large class of such modifications of special and general relativity, for which the WKB condition is not violated at ultrahigh frequencies, the predictions remain unchanged. The opposite possibility is excluded because of the absence of a large amount of particles created due to the Universe expansion. The creation of particles in the quantum state minimizing the energy density of a given mode at the moment of Planck boundary crossing is also prohibited by the latter argument (contrary to the creation in the adiabatic vacuum state, which is very small now). © 2001 MAIK “Nauka/Interperiodica”.

PACS numbers: 04.62.+v; 98.70.Vc; 98.80.Cq

The approximately flat spectrum of scalar and tensor perturbations generated by quantum vacuum fluctuations at a quasi-de Sitter (inflationary) state in the early Universe is certainly the most important prediction of the inflationary scenario, because it can be directly tested and falsified using observational data. Fortunately, all existing and continuously accumulated data, instead of falsifying, confirm these predictions (within observation errors). Another observational prediction of the simplest variants of the inflationary scenario—the approximate flatness of the Universe,  $|\Omega_{\text{tot}} - 1| \ll 1$ —is actually a consequence of the first one, since an isotropic part of the spatial curvature can be considered as a monopole perturbation with respect to the spatially flat Friedmann–Robertson–Walker (FRW) background. Note that the first quantitatively correct derivation of perturbation spectra *after* inflation was obtained in [1] for the case of tensor perturbations (gravitational waves) and in [2] for the case of scalar (adiabatic) perturbations. For completeness, one should mention two important intermediate steps made between 1979 and 1982 on the way to the correct answer as to scalar perturbations: in [3], the first estimate of scalar perturbations after inflation was made according to which scalar and tensor perturbations are of the same order of magnitude, while the spectrum of scalar perturbations *during* inflation was calculated in [4] using the Starobinsky inflationary model [5] (however, the actual amplitude of scalar perturbations *after* inflation was still significantly underestimated in both these papers).

Therefore, it is very important to investigate the validity of assumptions on which this prediction is based.<sup>2</sup> All derivations of perturbation spectra use quantum field theory in classical curved space–time or semi-classical quantum cosmology. Both these approaches are valid and essentially equivalent if  $H \ll M_p$ , where  $H \equiv \dot{a}/a$ ,  $a(t)$  is the scale factor of a flat FRW cosmological model, the dot denotes time derivative,  $M_p = \sqrt{G}$ , and  $\hbar = c = 1$  is put throughout the paper. On the other hand, comparison of the predicted spectrum with observational data shows that  $H$  should be less than  $\sim 10^{-5}M_p$  at least during last 70 e-folds of inflation. So, the assumption  $H \ll M_p$  is *required* and *self-consistent*, if we are speaking about inflationary models having relation to reality. Recently it was questioned whether the inflationary predictions are robust with respect to a change in the so-called “trans-Planckian physics.” What is meant by this term is some *ad hoc* modification of special and general relativity leading to violation of the Lorentz invariance and to deviation of the dispersion law  $\omega(k)$  from the linear one for field quanta with frequencies (energies)  $\omega > M_p$ , where  $k$  is the particle wave number (momentum). In the absence of the Lorentz invariance, a preferred system of reference appears (in which this dispersion law is written). Usually, it is identified with the basic cosmological system of reference which is at rest with respect to spatially averaged matter in the Universe.

<sup>2</sup> Results of this paper partially overlap with those obtained in recent papers [6, 7] (which appeared when this paper was prepared for publication) and are in general agreement with them whenever they overlap.

<sup>1</sup> This article was submitted by the author in English.

Initially, trans-Planckian physics was introduced to obtain a new way to derive Hawking radiation from black holes. In this case, it was shown that the spectrum of Hawking radiation does not depend on a particular form of dispersion law  $\omega(k)$  at  $k \rightarrow \infty$  [8–10]. On the other hand, an opposite result was recently claimed in [11] regarding the inflationary perturbation spectrum. No self-consistent theory of such a modification exists leading to a certain unique dispersion law  $\omega(k)$ , but arguments showing that this possibility should not be considered as logically impossible are based either on higher dimensional models of the Universe (see, e.g., recent paper [12]) or on the condensed matter analogues of gravity [13, 14] which do not have too much symmetry at the most fundamental level. So,  $\omega(k)$  should be considered as some fixed but unknown function at the present state-of-the-art level.

The very possibility of trans-Planckian physics affecting the (supposedly known) sub-Planckian physics is due to the expansion of the Universe. This expansion gradually shifts all modes of quantum fields from the former region to the latter one. Indeed, for a FRW model with metric

$$ds^2 = dt^2 - a^2(t)dl^2, \quad (1)$$

where  $dl^2$  is the 3D Euclidean space interval (spatial curvature can be always neglected), the spatial dependence of a given quantum field mode can be taken as  $\exp(in_\mu x^\mu)$ ,  $\mu = 1, 2, 3$ . Then the frequency  $\omega = n/a(t)$ ,  $n = |\mathbf{n}| = \text{const}$  in the ultrarelativistic (but still Lorentzian) limit. This redshifting occurs equally well in the early and the present-day Universe. So, any effect connected with trans-Planckian physics can also be observed now; inflation (i.e., the epoch when  $|\dot{H}| \ll H^2$ ) is not specific for that at all.

I will model metric fluctuations by a massless minimally coupled scalar field satisfying the equation  $\nabla_i \nabla^i \phi = 0$ . This form is sufficient both for scalar perturbations for which the effective mass satisfies the condition  $|m^2| \ll H^2$  necessary for inflation and for tensor perturbations because their amplitude satisfies the same wave equation in the FRW Universe filled by any matter with no nondiagonal pressure perturbations ( $\delta p_{\mu\nu} \propto d_{\mu\nu}$ ). It is also assumed that  $H \ll M_p$ . Then the equation for the time-dependent part of  $\phi_n$  reads

$$\ddot{\phi}_n + 3H\dot{\phi}_n + \omega^2 \left( \frac{n}{a} \right) \phi_n = 0, \quad (2)$$

with  $\omega(k) = k$  for  $\omega \ll M_p$ . Solutions of this equation have the WKB form for  $H \ll \omega \ll M_p$ :

$$\phi_n = \frac{\alpha_n}{\sqrt{2na}} e^{-in\eta} + \frac{\beta_n}{\sqrt{2na}} e^{in\eta}, \quad \eta = \int \frac{dt}{a(t)}, \quad (3)$$

where  $\alpha_n, \beta_n = \text{const}$ , and  $|\alpha_n|^2 - |\beta_n|^2 = 1$  for any quantum state if the quantum field  $\hat{\phi}$  is second-quantized and

$\phi_n \exp(in_\mu x^\mu) (2\pi)^{-3/2}$  is the c-number coefficient of the Fock annihilation operator  $\hat{a}_n$ . The average number of created pairs is  $N(n) = |\beta_n|^2$ . Therefore, whatever the trans-Planckian physics is (namely, whatever the form of  $\omega(k)$  and the initial condition for  $\phi_n$  at  $t \rightarrow -\infty$ ), once  $\omega \ll M_p$ , we can say that field mode (3) emerges from the Planck boundary  $n = M_p a$  in some quantum state that is characterized by  $\alpha_n$  and  $\beta_n$ . In particular, the rate of growth of the average energy density of particles with  $\omega \ll M_p$  is

$$\frac{d(\langle \varepsilon \rangle a^4)}{a^4 dt} = \frac{gM^4 H}{2\pi^2} N(n)|_{n=Ma}, \quad (4)$$

where  $g = 1$  for scalars and  $g = 2$  for gravitons.  $M$  is an auxiliary mass satisfying  $H \ll M < M_p$  for which  $\omega(M) = M$  with sufficient accuracy (for estimates, we will take  $M = M_p$ ). It follows from time translation invariance that  $N^{(0)}(n)$  is independent of  $n$ . Here,  $N^{(0)}$  means the part of  $N(n)$  which does not depend on the background space-time curvature at the moment of Planck boundary crossing ( $n = M_p a$ ).

Let us first consider the case where the WKB condition for  $\phi_n$  is satisfied for all  $n \gg Ha$  including the trans-Planckian region  $n > M_p a$ . Then the natural and self-consistent choice of the initial condition for  $\phi_n$  is the adiabatic vacuum at  $t \rightarrow -\infty$ :

$$\phi_n = \frac{1}{\sqrt{2\omega_n a^3}} \exp(-i \int \omega_n dt). \quad (5)$$

Note that this mode is not in the minimum energy-density state at finite  $t$ , in particular, at the moment of Planck boundary crossing (I will return to the discussion of this point below). Equation (5) reduces to Eq. (3) with  $\beta_n = 0$  and  $\alpha_n = 1$  in the sub-Planckian region. Then it just coincides with the initial condition for  $\phi_n$  used in the standard calculation of the spectrum of inflationary perturbations. Thus, no correction to the standard result arises in this case, irrespective of the form of  $\omega(n/a)$ .

The necessary condition for the WKB behavior is  $|\dot{\omega}| \ll \omega^2$  or

$$\frac{H|d(1/\omega(k))|}{d \ln k} \ll 1, \quad k = n/a \quad (6)$$

for all  $k > M_p$ . Since  $H/M_p$  is already a small parameter and  $\omega(k)$  presumably does not depend on  $H$  for  $k \gg H$ , this inequality is satisfied practically always if  $\omega$  does not become zero either for  $k \rightarrow \infty$  or at some finite  $k_0 > M_p$  [another dangerous case is when  $d\omega/dk$  diverges at a finite  $k = k_0$ , in particular, if  $\omega \propto (k_0 - k)^\gamma$  with  $-1 < \gamma < 0$  or  $\omega \approx \omega_0 + \omega_1(k_0 - k)^\gamma$ ,  $0 < \gamma < 1$ ]. As a consequence,  $N^{(0)} = 0$  for the dispersion law  $\omega(k) = M \tanh^{1/m} [(k/M)^m]$ ,  $m > 0$  proposed by Unruh [8], for  $\omega^2 = k^2 [1 + b_m (k/M)^{2m}]$  with positive  $m$  and  $b_m$  consid-

ered in [10, 11], and for the  $\omega^2 = [M \ln(1 + k/M)]^2$  dependence introduced in [15].

There still exist exceptional forms of  $\omega(k)$  for which the WKB behavior is not valid for some  $k > M_p$ . In particular, this refers to the case  $\omega^2 = k^2[1 + b_m(k/M)^{2m}]$  with  $b_m < 0$  and to the dispersion law introduced in recent paper [16], for which  $\omega(k) \rightarrow 0$  at  $k \rightarrow \infty$ . Such a possibility should not be excluded *a priori*. Then there is *no* preferred initial condition for  $\phi_n$ , and it is impossible to define a unique initial vacuum state. So, in this case  $N^{(0)} \neq 0$  generically; i.e., creation of pairs in the expanding Universe occurs due to trans-Planckian physics.

However, nature tells us that such an effect is infinitesimally small, if exists at all. Indeed, from the evident condition that the created ultrarelativistic particles do not contribute significantly to the present energy density in the Universe, it follows that  $N^{(0)} \lesssim H_0^2/M_p^2 \sim 10^{-122}$ , where  $H_0 = H(t = t_0)$  is the Hubble constant. Thus, curvature-independent particle creation due to trans-Planckian physics in the expanding Universe is very strongly suppressed, in any case because of observational data. Of course, the corresponding change in the inflationary perturbation spectrum is also negligible (relative correction is  $\sim |\beta_n| = \sqrt{N^{(0)}}$ ).

Finally, let us consider a more subtle effect: creation of particles due to both trans-Planckian physics and background space-time curvature in the expanding Universe. Then  $N(n) \sim H^2/M_p^2$ , where  $H$  is estimated at the moment of high-energy boundary crossing  $n = Ma(t)$ . Certainly, corrections to the inflationary spectrum are negligible ( $\sim H/M_p < 10^{-5}$ ) in this case. Nevertheless, even such a small effect can be significantly restricted. An example of this effect arises if one assumes that modes crossing the boundary  $n = Ma$  are in the exactly minimum energy-density state just at this moment; i.e.,  $\phi_n = -in\phi_n/a = -i\sqrt{n/2}a^{-2}$  and  $\epsilon_n \equiv (|\dot{\phi}_n|^2 + n^2 a^{-2}|\phi_n|^2)/2 = n/2a^4$  for each mode at the moment  $t = t_n$  when  $n = Ma$ . On the other hand, the adiabatic vacuum for each mode has the larger energy density

$$\epsilon_n = \frac{n}{2a^4} \left( 1 + \frac{H^2 a^2}{2n^2} \right) \quad (7)$$

(see, e.g., [17, 18]). Note that this excess is due only to vacuum polarization. Of course, this assumption may be immediately criticized from the logical point of view because such a state ceases to diagonalize the mode Hamiltonian and minimize its energy density for all other moments of time  $t \neq t_n$ . Nevertheless, let us consider its implications.

Writing, as, e.g., in [17],

$$\begin{aligned} \phi_n(t) &= (2\omega_n a^3)^{-1/2} \\ &\times (\alpha_n(t) \exp(-i \int \omega_n dt) + \beta_n(t) \exp(i \int \omega_n dt)), \end{aligned} \quad (8)$$

$$\begin{aligned} \dot{\phi}_n(t) &= -i \left( \frac{\omega_n}{2a^3} \right)^{1/2} \\ &\times (\alpha_n(t) \exp(-i \int \omega_n dt) - \beta_n(t) \exp(i \int \omega_n dt)), \end{aligned} \quad (9)$$

so that  $\alpha_n(t_n) = 1$  and  $\beta_n(t_n) = 0$  for the Heisenberg quantum state of each mode  $|\psi_n\rangle$  which minimizes its Hamiltonian and energy density at the moment  $t = t_n$  when  $n = Ma$ , we obtain the following system of equations for  $\alpha_n(t)$  and  $\beta_n(t)$ :

$$\dot{\alpha}_n = \frac{1}{2} \left( \frac{\dot{\omega}}{\omega} + 3 \frac{\dot{a}}{a} \right) e^{2i \int \omega_n dt} \beta_n, \quad (10)$$

$$\dot{\beta}_n = \frac{1}{2} \left( \frac{\dot{\omega}}{\omega} + 3 \frac{\dot{a}}{a} \right) e^{-2i \int \omega_n dt} \alpha_n, \quad (11)$$

with the additional condition  $|\alpha_n|^2 - |\beta_n|^2 = 1$ . If  $\omega \gg H$ ,  $\beta_n$  is small and  $\alpha_n \approx 1$ . For  $t \geq t_n$ , one may take  $\omega_n \approx n/a$ . Then  $\beta_n = -(iH(t_n)/2M) \exp(-2i\eta(t_n))$  plus a strongly oscillating term. So,

$$N(n) = |\beta_n(\infty)|^2 = H^2(t_n)/4M^2. \quad (12)$$

If the cosmological constant is neglected and the present law of the Universe expansion is taken as  $a(t) \propto t^{2/3}$ , then  $N(n) \propto n^{-3}$  for particle energies close to  $M_p$  at the present time. Integrating Eq. (4) with  $N(n)$  from Eq. (12), one obtains  $\epsilon_g = M^2/9\pi^2 t^2$  for gravitons. For  $M \sim M_p$  one has  $\epsilon_g \sim H^2/G$ , which contradicts the assumption that  $a(t) \propto t^{2/3}$ . In other words, this model of particle creation by trans-Planckian physics results in a significant part of the present total energy density of matter in the Universe being contained in gravitons with energies  $\sim M_p$ , which is not compatible with the observed behavior of  $a(t)$ . Similar arguments show that there may be no term

$$N(n) = N^{(1)}(n) \frac{|R(t_n)|}{M_p^2} \quad (13)$$

with  $N^{(1)} \sim 1$  in Eq. (4). Here,  $R$  is the scalar curvature.

On the other hand, for the adiabatic vacuum state in the WKB regime, the quantity  $\beta_n = iH(t)a(t)\exp(-2im\eta)/2n$  in the leading order, so that it approaches zero at  $t \rightarrow \infty$ . Note that the creation of real gravitons does occur in the next order ( $N = N^{(2)}(n)R^2/M_p^2$ ) and even without any violation of the Lorentz invariance [19]. In the latter case, the effect is due to the violation of the WKB approximation at ultralow, and not ultrahigh, frequencies  $\omega \sim H$ . Also, the notion of ‘‘vacuum’’ as a state of minimum energy density may be restored in the follow-

ing nonrigorous sense: the adiabatic vacuum for each mode  $n$  in the WKB regime has the lowest energy density, compared to other quantum states, if the energy density is averaged (“coarse grained”) over a time interval  $\Delta t \gg \omega_n^{-1}$ , in accordance with the energy uncertainty relation.

So, whatever occurs in the trans-Planckian region, observational evidence shows that creation of particles due to mode transition from the trans-Planckian region to the sub-Planckian one is absent with a very high accuracy. The standard predictions about perturbations generated during inflation are not altered by this hypothetical mechanism either.

I am thankful to Prof. K. Sato and M. Kawasaki for hospitality in RESCEU, the University of Tokyo. This work was supported in part by the Russian Foundation for Basic Research, project nos. 99-02-16224 and 00-15-96699.

#### REFERENCES

1. A. A. Starobinsky, Pis'ma Zh. Éksp. Teor. Fiz. **30**, 719 (1979) [JETP Lett. **30**, 682 (1979)].
2. S. W. Hawking, Phys. Lett. B **115B**, 295 (1982); A. A. Starobinsky, Phys. Lett. B **117B**, 175 (1982); A. H. Guth and S. Y. Pi, Phys. Rev. Lett. **49**, 1110 (1982).
3. V. N. Lukash, Zh. Éksp. Teor. Fiz. **79**, 1601 (1980) [Sov. Phys. JETP **52**, 807 (1980)].
4. V. F. Mukhanov and G. V. Chibisov, Pis'ma Zh. Éksp. Teor. Fiz. **33**, 549 (1981) [JETP Lett. **33**, 532 (1981)].
5. A. A. Starobinsky, Phys. Lett. B **91B**, 99 (1980).
6. T. Tanaka, astro-ph/0012431 (2000).
7. J. C. Niemeyer and R. Parentani, astro-ph/0101451 (2001).
8. W. G. Unruh, Phys. Rev. D **51**, 2827 (1995).
9. R. Brout, S. Massar, R. Parentani, and P. Spindel, Phys. Rev. D **52**, 4559 (1995).
10. S. Corley and T. Jacobson, Phys. Rev. D **54**, 1568 (1996).
11. R. H. Brandenberger and J. Martin, astro-ph/0005432 (2000); J. Martin and R.H. Brandenberger, hep-th/0005209 (2000).
12. D. J. H. Chung, E. W. Kolb, and A. Riotto, hep-ph/0008126 (2000).
13. G. E. Volovik, Phys. Rep. (2001) (in press); gr-qc/0005091 (2000).
14. G. E. Volovik, Pis'ma Zh. Éksp. Teor. Fiz. **73**, 182 (2001) [JETP Lett. **73**, 162 (2001)]; hep-ph/0101286 (2001).
15. J. Kowalski-Glikman, Phys. Lett. B **499**, 1 (2001).
16. L. Mersini, M. Bastero-Gil, and P. Kanti, hep-ph/0101210 (2001).
17. Ya. B. Zeldovich and A. A. Starobinsky, Zh. Éksp. Teor. Fiz. **61**, 2161 (1971) [Sov. Phys. JETP **34**, 1159 (1972)].
18. S. A. Fulling, L. Parker, and B. L. Hu, Phys. Rev. D **10**, 3905 (1974).
19. Ya. B. Zeldovich and A. A. Starobinsky, Pis'ma Zh. Éksp. Teor. Fiz. **26**, 373 (1977) [JETP Lett. **26**, 252 (1977)].

# Mesoscopic Casimir Forces in Quantum Vacuum<sup>1</sup>

G. E. Volovik

*Low Temperature Laboratory, Helsinki University of Technology, FIN-02015 HUT, Finland  
Landau Institute for Theoretical Physics, Russian Academy of Sciences, Moscow, 117940 Russia*

Received March 14, 2001

Traditionally, it is assumed that the Casimir vacuum pressure does not depend on the ultraviolet cutoff. There are, however, some arguments that the effect actually depends on the regularization procedure and thus on trans-Planckian physics. We provide the condensed matter example where the Casimir forces do explicitly depend on microscopic (correspondingly trans-Planckian) physics due to the mesoscopic finite- $N$  effects, where  $N$  is the number of bare particles in condensed matter (or correspondingly the number of elements comprising the quantum vacuum). The finite- $N$  effects lead to mesoscopic fluctuations of the vacuum pressure. The amplitude of the mesoscopic fluctuations of the Casimir force in a system with linear dimension  $L$  is a factor of  $N^{1/3} \sim L/a_p$  larger than the traditional value of the Casimir force given by effective theory, where  $a_p = \hbar/p_p$  is the interatomic distance which plays the role of the Planck length. © 2001 MAIK “Nauka/Interperiodica”.

PACS numbers: 67.20.+k; 11.10.-z

## INTRODUCTION

The attractive force between two parallel metallic plates in vacuum induced by vacuum fluctuations of an electromagnetic field was predicted by Casimir in 1948 [1]. The calculation of vacuum pressure is based on regularization schemes, which allows one to separate the effect of low-energy modes of the vacuum from a huge diverging contribution of the high-energy degrees of freedom. There are different regularization schemes: Riemann's zeta-function regularization, introduction of the exponential cutoff, dimensional regularization, etc. People are happy when different regularization schemes give the same results. But this is not always so (see, e.g., [2–4]; in particular, the divergences occurring for spherical geometry in even spatial dimension are not canceled [5, 6]). This raises some criticism against the regularization methods [7] or even some doubts concerning the existence and the magnitude of the Casimir effect.

The Casimir effect of the same type arises in condensed matter due to thermal (see review paper [8]) or/and quantum fluctuations. When considering the analogue of the Casimir effect in condensed matter, the following correspondence must be taken into account. The ground state of quantum liquid corresponds to the vacuum of quantum field theory. The low-energy bosonic and fermionic quasiparticles in quantum liquid correspond to matter. The low-energy modes with linear spectrum  $\omega = c_s p$  can be described by the relativistic-type effective theory. The speed of sound  $c_s$  or of other collective modes (spin waves, etc.) plays the role

of the speed of light. This “speed of light” is the “fundamental constant” which enters the effective theory (quantum hydrodynamics in quantum liquids or electromagnetic theory in real vacuum). The fundamental constants of the effective theory can be in principle calculated using microscopic physics, an analogue of trans-Planckian physics. The effective theory is valid only at low energy that is much smaller than the “Planck cutoff.” In quantum liquids, the analogue of the Planck energy scale  $E_p$  is determined either by the mass  $m$  of the atom in the liquid,  $E_p \equiv mc_s^2$ , or by the Debye energy,  $E_p \equiv \hbar c_s/a_p$ , where  $a_p$  is the interatomic distance which plays the role of Planck length [9].

In some cases, the analogy between effective theories in quantum vacuum and in quantum liquids becomes exact. For example, the low-energy fermionic and bosonic collective modes can correspond to the chiral fermions and gravitational and gauge fields. This allows one to simulate in condensed matter the phenomena such as chiral anomaly and event horizon (see review [9]).

The advantage of the quantum liquid is that the structure of the quantum vacuum is known at least in principle. That is why one can calculate everything starting from the first principle microscopic theory. For example, one can calculate the vacuum energy under different external conditions without invoking any cutoff or regularization scheme. Then one can compare the results with what can be obtained within the effective theory dealing only with the low-energy phenomena. The latter requires the regularization scheme in order to cancel the ultraviolet divergency, and thus one can judge whether and which of the regularization schemes are physically relevant.

<sup>1</sup> This article was submitted by the author in English.

The traditional Casimir effects deal with the low energy massless modes. The typical massless modes in quantum liquid are sound waves. The acoustic field is described by the effective theory and corresponds to the massless scalar field. The walls provide the boundary conditions for the sound wave mode; usually these are the Neumann boundary conditions. Because of the quantum hydrodynamic fluctuations, there must be the Casimir force between two parallel plates immersed in the quantum liquid. Within the effective theory, the Casimir force is given by the same equation as the Casimir force acting between the conducting walls due to quantum electromagnetic fluctuations. The only modifications are (i) the speed of light must be replaced by the spin of sound  $c_s$  and (ii) the factor 1/2 must be added, since we have the scalar field of a longitudinal sound wave instead of two polarizations of light. If  $a$  is the distance between the plates and  $A$  is their area, then the  $a$ -dependent contribution to the ground-state energy of the quantum liquid at  $T = 0$  in the effective theory must be

$$E_C = -\frac{\hbar c_s \pi^2 A}{1440 a^3}. \quad (1)$$

The microscopic quantities of the quantum liquid such as the mass of atom  $m$  and interatomic space  $a_p$  do not explicitly enter Eq. (1); the traditional Casimir force is completely determined by the “fundamental” parameter  $c_s$  of the effective scalar field theory.

However, I will show that Eq. (1) is not always true. I will give here an example where the effective theory is not able to predict the Casimir force, because the microscopic high-energy degrees of freedom become important. In other words, the trans-Planckian physics shows up, and the “Planck” energy scale explicitly enters the result. In this situation, the Planck scale is physical and cannot be removed by any regularization.

Equation (1) gives a finite-size contribution to the energy of quantum liquid. It is inversely proportional to the linear dimension of the system,  $E_C \propto 1/L$ . However, it is important for us that it is not only the finite-size effect but also the finite- $N$  effect,  $E_C \propto N^{-1/3}$ , where  $N$  is the number of atoms in the liquid in the slab, which is a discrete quantity. Since the main contribution to the vacuum energy is  $\propto L^3 \propto N$ , the relative correction of order  $N^{-4/3}$  means that the Casimir force is the mesoscopic effect. I will show that in quantum liquids the essentially larger mesoscopic effects of the relative order  $N^{-1}$  can be more pronounced. Such a finite- $N$  effect cannot be described by the effective theory dealing with the continuous medium, even if the theory includes the real boundary conditions with the frequency dependence of dielectric permeability.

I will start with the simplest quantum “liquid”—one-dimensional Fermi gas—where the mesoscopic Casimir forces can be calculated exactly without invoking any regularization procedure.

## VACUUM ENERGY FROM MICROSCOPIC THEORY

I consider a system of  $N$  one-dimensional massless fermions, whose continuous energy spectrum is  $\omega(p) = cp$ , with  $c$  playing the role of speed of light. Let us start with the microscopic theory, which is extremely simple: at  $T = 0$  fermions merely occupy all energy levels below chemical potential  $\mu$ . In the continuous limit, the total number of particles  $N$  and the total energy in a one-dimensional “cavity” of size  $a$  are expressed in terms of the Fermi momentum  $p_F = \mu/c$  in the following way:

$$N = na = a \int_{-p_F}^{p_F} \frac{dp}{2\pi\hbar} = \frac{ap_F}{\pi\hbar}, \quad (2)$$

$$E = \epsilon(n)a = a \int_{-p_F}^{p_F} \frac{dp}{2\pi\hbar} cp = \frac{acp_F^2}{2\pi\hbar} = \frac{\pi}{2} \hbar c a n^2. \quad (3)$$

Here,  $n$  is the particle density. The vacuum energy density of this condensed matter as a function of  $n$  is  $\epsilon(n) = (\pi\hbar c/2)n^2$ . The equation of state comes from the thermodynamic identity relating the pressure  $P$  to the energy:

$$P = \mu n - \epsilon, \quad (4)$$

where  $\mu = d\epsilon/dn = cp_F$  is the chemical potential. In our case  $\mu = cp_F$ , and one obtains the equation of state for our vacuum

$$P = \epsilon, \quad (5)$$

which is conventional for the system of 1 + 1 relativistic fermions.

## VACUUM ENERGY IN EFFECTIVE THEORY

As distinct from the microscopic theory, which deals with bare particles, the effective theory deals with the quasiparticles—fermions living at the level of chemical potential  $\mu = cp_F$ . There are four different quasiparticles: (i) quasiparticles and quasiholes living in the vicinity of the Fermi point  $p_z = +p_F$  have spectrum  $\omega_{qp}(p_+) = |\omega(p) - \mu| = c|p_+|$ , where  $p_+ = p_z - p_F$ , and (ii) quasiparticles and quasiholes living in the vicinity of the other Fermi point at  $p_z = -p_F$  have spectrum  $\omega_{qp}(p_-) = |\omega(p) - \mu| = c|p_-|$ , where  $p_- = p_z + p_F$ . In the effective theory, the energy of the system is the energy of the Dirac vacuum  $E = -\sum_{p_+} c|p_+| - \sum_{p_-} c|p_-|$ . This energy is divergent and requires a cutoff, which is provided by the Fermi momentum playing the role of the cutoff Planck momentum:  $p_F \equiv p_p$ . Note that even with this cutoff the energy obtained within the effective theory has a wrong sign, compared with the correct microscopic result in Eq. (3).

The difference between the energies obtained in the microscopic and the effective theory approaches becomes important if gravity is involved, since the energy is the

source of the gravitational field. What kind of vacuum energy is gravitating is the essence of the cosmological constant problem.

### RELEVANT VACUUM ENERGY AND COSMOLOGICAL CONSTANT

Inspection of those condensed matter systems in which an effective gravity arises as a low energy phenomenon suggests the possible answer: the vacuum energy density responsible for the cosmological constant is  $\tilde{\epsilon} = \epsilon - \mu n$  [9, 10]. This follows from microscopic physics: the conservation of particle number  $N$  requires that the quantum field theoretical description of the  $N$ -body system be given by  $\mathcal{H} - \mu\mathcal{N}$ , where  $\mathcal{H}$  and  $\mathcal{N}$  are the Hamiltonian and the particle number operators in the second-quantized form. The energy  $\tilde{\epsilon}$  does not depend on the choice of zero energy level: the shift  $\Delta$  of the zero energy level for one particle leads to the shift of the chemical potential  $\mu \rightarrow \mu + \Delta$  and of the total energy  $E \rightarrow E + N\Delta$ , while  $\tilde{E} = E - \mu N$  remains invariant. In terms of  $\tilde{\epsilon}$ , the equation of state of the quantum vacuum is always

$$P = -\tilde{\epsilon}. \quad (6)$$

Although this is obtained using the microscopic theory ( $\tilde{\epsilon}$  is not determined within the effective theory), the result does not depend on details of the quantum liquid: it follows from the thermodynamic identity in Eq. (4).

Equation (6) is the same as the equation of state of the vacuum in quantum field theory, which follows from the Einstein cosmological term. Thus,  $\tilde{\epsilon}$  serves as the cosmological constant in the effective gravitational theory. For our vacuum represented by the Fermi gas, this cosmological constant is large, being determined by the Planck energy scale,  $\tilde{\epsilon} \sim -cp_p^2$ . The minus sign is in agreement with the negative energy of the Dirac vacuum in effective theory, and, according to Eq. (6), this corresponds to the positive vacuum pressure: Fermi gas (and also the Dirac vacuum) can be in equilibrium only in the presence of positive external pressure  $P$ .

There are, however, quantum liquids which can exist without an external pressure. Liquid  $^3\text{He}$  and liquid  $^4\text{He}$  at  $T = 0$  are examples. In both of these liquids, there is some analogue of gravity that arises in the low-energy corner. Let us consider the ground state of such quantum liquid, if there is no contact with the environment. In a complete equilibrium, the pressure  $P$  in the liquid must be zero, since there is no external forces acting on the liquid. Then, from Eq. (6), one automatically obtains that for such equilibrium vacuum at  $T = 0$  the cosmological constant in the effective gravity is identically zero,  $\tilde{\epsilon} \equiv 0$ , without any fine tuning. This means that, according to the quantum liquid analogy,

the stationary equilibrium vacuum is not gravitating (see for more details [10]).

### LEAKAGE OF VACUUM THROUGH THE WALL

Now let us discuss the Casimir effect—a change in the vacuum pressure caused by the finite-size effects in the vacuum. We must take into account the discreteness of the spectrum of bare particles or quasiparticles (depending on which theory we use, microscopic or effective) in the slab. Let us start with the microscopic description in terms of bare particles (atoms). We can use two different boundary conditions for particles, which give two kinds of discrete spectrum

$$\omega_k = k \frac{\hbar c \pi}{a}. \quad (7)$$

$$\omega_k = \left(k + \frac{1}{2}\right) \frac{\hbar c \pi}{a}. \quad (8)$$

Equation (7) corresponds to the “classical spinless” fermions with Dirichlet boundary conditions. Equation (8) is for the  $1 + 1$  Dirac fermions with no particle current through the wall; this case with the generalization to the  $d + 1$  fermions was discussed in [11].

The vacuum is represented by the ground state of the collection of  $N$  noninteracting particles in a 1D box of size  $a$ . The “vacuum” energies for the spinless and Dirac fermions are correspondingly

$$E(N, a) = \sum_{k=1}^N \omega_k = \frac{\hbar c \pi}{2a} N(N+1), \quad (9)$$

$$E(N, a) = \sum_{k=0}^{N-1} \omega_k = \frac{\hbar c \pi}{2a} N^2. \quad (10)$$

To calculate the Casimir force acting on the wall, we must introduce the vacuum on both sides of the wall. Let us thus consider three walls: at  $z = 0$ ,  $z = a_1 < a$ , and  $z = a$ . Then we have two slabs with sizes  $a_1$  and  $a_2 = a - a_1$ , and we can find the force acting on the wall between the two slabs, i.e., at  $z = a_1$ . We assume the same boundary conditions for all walls. But we must allow the particles to transfer between the slabs, otherwise the main force acting on the wall between the slabs will be due to the different bulk pressure in the two slabs. This can be done due to, say, very small holes (tunnel junctions) in the wall, which do not violate the boundary conditions and do not disturb the particle energy levels, but still allow the particle exchange between the two vacua.

This situation can be compared with the traditional Casimir effect. The force between the conducting plates arises because the electromagnetic fluctuations of the vacuum in the slab are modified due to boundary conditions imposed on electric and magnetic fields. In reality, these boundary conditions apply only in the

low-frequency limit, while the wall is transparent for the high-frequency electromagnetic modes, as well as for the other degrees of freedom of real vacuum (fermionic and bosonic), which can easily penetrate through the conducting wall. In the traditional approach, it is assumed that these degrees of freedom, which produce the divergent terms in the vacuum energy, must be canceled by the proper regularization scheme. That is why, although the dispersion of dielectric permeability does weaken the real Casimir force, nevertheless in the limit of large distances,  $a_1 \gg c/\omega_0$ , where  $\omega_0$  is the characteristic frequency at which the dispersion becomes important, the Casimir force does not depend on how easily the high-energy vacuum leaks through the conducting wall.

I consider here just the opposite limit, when (almost) all bare particles are totally reflected. This corresponds to the case when the penetration of the high-energy vacuum modes through the conducting wall is highly suppressed, and thus one must certainly have the traditional Casimir force. Nevertheless, I will show that, due to the mesoscopic finite- $N$  effects, the contribution of the diverging terms to the Casimir effect becomes dominant. They produce highly oscillating vacuum pressure, whose amplitude exceeds the value of the conventional Casimir pressure by a factor of  $p_P a/\hbar$ . For their description, the continuous effective low-energy theories do not apply.

### MESOSCOPIC CASIMIR FORCE IN 1D FERMI GAS

The total vacuum energies of the spinless and Dirac fermions in two slabs are

$$E = \frac{\hbar c \pi}{2} \left( \frac{N_1(N_1 + 1)}{a_1} + \frac{N_2(N_2 + 1)}{a_2} \right), \quad (11)$$

$$E = \frac{\hbar c \pi}{2} \left( \frac{N_1^2}{a_1} + \frac{N_2^2}{a_2} \right), \quad (12)$$

$$N_1 + N_2 = N, \quad a_1 + a_2 = a. \quad (13)$$

Since particles can transfer between the slabs, the global vacuum state in this geometry is obtained by the minimization over the discrete particle number  $N_1$  at a fixed total number  $N$  of particles in the vacuum. If the mesoscopic  $1/N$  corrections are ignored, one obtains  $N_1 \approx (a_1/a)N$  and  $N_2 \approx (a_2/a)N$ , and the force acting on the wall between the two vacua is zero.

However,  $N_1$  and  $N_2$  are integer valued, and this leads to mesoscopic fluctuations of the Casimir force. Within a certain range of parameter  $a_1$ , there is a global minimum characterized by integers  $(N_1, N_2)$ . In the neighboring intervals of parameters  $a_1$ , one has either  $(N_1 + 1, N_2 - 1)$  or  $(N_1 - 1, N_2 + 1)$ . The force acting on

the wall in the state  $(N_1, N_2)$  is obtained by variation of  $E(N_1, N_2, a_1, a - a_1)$  with respect to  $a_1$  at fixed  $N_1$  and  $N_2$ :

$$F_{N_1 N_2 a_1 a_2} = -\frac{dE_{N_1 N_2 a_1 a_2}}{da_1} + \frac{dE_{N_1 N_2 a_1 a_2}}{da_2}. \quad (14)$$

If  $a_1$  increases, then at some critical value of  $a_1$ , where  $E(N_1, N_2, a_1, a_2) = E(N_1 + 1, N_2 - 1, a_1, a_2)$ , one particle must cross the wall from the right to the left. At this critical value, the force acting on the wall changes abruptly {we do not discuss here interesting physics arising just at the critical values of  $a_1$ , where the degeneracy of the states  $(N_1, N_2)$  and  $(N_1 + 1, N_2 - 1)$  occurs; for these positions of the wall (or membrane), the particle numbers  $N_1$  and  $N_2$  are undetermined and are actually fractional due to the quantum tunneling between the slabs [12]}. Using, for example, the spectrum in Eq. (12), one obtains for the jump in the Casimir force

$$F_{N_1 \pm 1, N_2 \mp 1} - F_{N_1, N_2} \approx \pm \frac{\hbar c \pi N}{a_1 a_2}. \quad (15)$$

If  $a_1 \ll a$ , the amplitude of the mesoscopic force

$$|\Delta F_{\text{meso}}| = \frac{\hbar c \pi n}{a_1} = \frac{\hbar c \pi n^2}{N_1} \equiv \frac{c p_P}{a_1}. \quad (16)$$

It is by a factor of  $1/N_1 = \pi \hbar / a_1 p_F \equiv \pi \hbar / a_1 p_P$  smaller than the bulk vacuum energy density in Eq. (3). On the other hand, it is by the same factor  $p_F a_1 \equiv p_P a_1$  larger than the traditional Casimir pressure, which in the 1D case is  $P_C \sim \hbar c / a_1^2$ . The divergent term which linearly depends on the Planck momentum cutoff  $p_P$ , as in Eq. (16), was revealed in many different calculations (see, e.g., [6]), and attempts were undertaken to invent the regularization scheme which would cancel the divergent contribution.

### MESOSCOPIC CASIMIR FORCES IN A GENERAL CONDENSED MATTER SYSTEM

Equation (16) for the amplitude of mesoscopic fluctuations of vacuum pressure can be generalized to any dimension. The mesoscopic random pressure comes from the discrete nature of the quantum vacuum in quantum liquids. If the volume  $V_1$  of the vessel changes continuously, the equilibrium number  $N_1$  of particles changes stepwise. This results in abrupt changes of pressure at some critical values of  $V_1$ :

$$P_{\text{meso}} \sim P_{N_1 \pm 1} - P_{N_1} = \pm \frac{dP}{dN_1} = \pm \frac{m c_s^2}{V_1} \equiv \pm \frac{c p_P}{V_1}. \quad (17)$$

The mesoscopic pressure is determined by microscopic physics, and thus a microscopic quantity such as the mass  $m$  of the atom, the ‘‘Planck mass,’’ enters this force.

For the pair-correlated systems such as Fermi superfluids with finite gap in the energy spectrum, the ampli-

tude must be twice as large. This is because the jumps in pressure occur when two particles (the Cooper pair) tunnel through the junction,  $\Delta N = \pm 2$ .

For the spherical shell of radius  $a$  immersed in the quantum liquid, the mesoscopic pressure is

$$P_{\text{meso}} \sim \pm \frac{3mc_s^2}{4\pi a^3} \equiv \pm \frac{3p_F c}{4\pi a^3}. \quad (18)$$

## DISCUSSION

Let us compare the mesoscopic vacuum pressure in Eq. (18) with the traditional Casimir pressure obtained within the effective theories for the same spherical shell geometry. In the case of the original Casimir effect, the effective theory is quantum electrodynamics. In superfluid  $^4\text{He}$ , this is low-frequency quantum hydrodynamics which is equivalent to the relativistic scalar field theory. The sound-wave modes with a linear (“relativistic”) spectrum play the role of the relativistic massless scalar field with Neumann boundary conditions corresponding to the (almost) vanishing current through the wall (recall that there must be some leakage through the shell to provide equal bulk pressure on both sides of the shell).

If we believe in the traditional regularization schemes which cancel out the ultraviolet divergence, then from the effective scalar field theory one must obtain the Casimir pressure  $P_C = -dE_C/dV = K\hbar c_s/8\pi a^4$ , where  $K = -0.4439$  for the Neumann boundary conditions and  $K = 0.005639$  for the Dirichlet boundary conditions [6]. However, at least in our case, the result obtained within the effective theory is not correct: the real Casimir pressure in Eq. (18) is produced by the finite- $N$  effect. It essentially depends on the Planck cutoff parameter; i.e., it cannot be determined by the effective theory; it is much larger, by a factor of  $p_F a/\hbar$ , than the traditional Casimir pressure; and it is highly oscillating. The regularization of these oscillations by, say, averaging over many measurements, by noise, or due to quantum or thermal fluctuations of the shell, etc., depends on the particular physical conditions of the experiment.

This shows that in some cases the Casimir vacuum pressure is not within the responsibility of the effective theory, and microscopic (trans-Planckian) physics must be invoked. If two systems have the same low-energy behavior and are described by the same effective theory, they do not necessarily experience the same Casimir effect. The result depends on many factors: discrete nature of the quantum vacuum, ability of the

vacuum to penetrate through the boundaries, dispersion relation at high frequency, etc. It is not excluded that even the original electromagnetic Casimir effect is renormalized by high-energy modes.

Of course, the extreme limit of an almost impenetrable wall, which we considered, does not apply to the original (electromagnetic) Casimir effect, where the overwhelming part of the fermionic and bosonic vacua easily penetrates the conducting walls, and where the mesoscopic fluctuations must be small. But are they negligibly small? In any case, our example shows that the cutoff problem is not a mathematical but a physical one, and the physics dictates the proper regularization scheme or the proper choice of the cutoff parameters.

The dependence of low-energy effects on physics beyond the effective theory was also discussed in connection with the Chern–Simons terms violating Lorentz and CPT symmetries [13, 14]. Quantum liquids provide an example of a finite system where trans-Planckian microscopic physics determines the coefficient of the Chern–Simons term [9, 15], which remains ambiguous within the effective theory.

I thank A.Yu. Kamenshchik for fruitful discussion. This work was supported in part by the Russian Foundation for Fundamental Research and by the ESF.

## REFERENCES

1. H. B. G. Casimir, Proc. K. Ned. Akad. Wet. **51**, 793 (1948).
2. G. Esposito, A. Yu. Kamenshchik, and K. Kirsten, Int. J. Mod. Phys. A **14**, 281 (1999); Phys. Rev. D **62**, 085027 (2000).
3. F. Ravndal, hep-ph/0009208.
4. H. Falomir, K. Kirsten, and K. Rebola, hep-th/0103050.
5. K. A. Milton, hep-th/0009173.
6. G. Cognola, E. Elizalde, and K. Kirsten, hep-th/9906228.
7. C. R. Hagen, quant-ph/0102135; Phys. Rev. D **61**, 065005 (2000).
8. M. Kardar and R. Golestanian, Rev. Mod. Phys. **71**, 1233 (1999).
9. G. E. Volovik, Phys. Rep. (in press); gr-qc/0005091.
10. G. E. Volovik, gr-qc/0101111.
11. R. D. M. De Paola, R. B. Rodríguez, and N. F. Svaiter, Mod. Phys. Lett. A **14**, 2353 (1999).
12. A. F. Andreev, Usp. Fiz. Nauk **168**, 655 (1998) [Phys. Usp. **41**, 581 (1998)].
13. R. Jackiw, Int. J. Mod. Phys. B **14**, 2011 (2000).
14. M. Perez-Victoria, hep-th/0102021.
15. G. E. Volovik, Pis'ma Zh. Éksp. Teor. Fiz. **70**, 1 (1999) [JETP Lett. **70**, 1 (1999)].

# Do Neutrino Oscillations Allow An Extra Phenomenological Parameter?<sup>1</sup>

I. S. Tsukerman

State Research Center Institute for Theoretical and Experimental Physics, Moscow, 117218 Russia  
e-mail: zuckerma@heron.itep.ru

Received March 11, 2001

The quantity  $\xi$  introduced recently in the phenomenological description of neutrino oscillations is in fact not a free parameter, but a fixed number. © 2001 MAIK "Nauka/Interperiodica".

PACS numbers: 14.60.Pq; 12.15.Ff

The literature on phenomenology of neutrino oscillations is vast (see, e.g., [1–6] and references therein). In a recent paper [7], Giunti and Kim in the case of two-flavor mixing have introduced a new phenomenological parameter  $\xi$ . According to [7],  $\xi = 0$  corresponds to the so-called equal-momentum assumption [1, 2], while  $\xi = 1$  corresponds to equal-energy assumption [5, 6]. The authors of [7] emphasize that  $\xi$  disappears from the final expressions for the neutrino oscillation probability.

The aim of this letter is to indicate that parameter  $\xi$  is fixed by energy–momentum conservation in the process which is responsible for neutrino emission, as explicitly assumed in [7].

Following [7], I will consider the decay  $\pi \rightarrow \mu\nu$  within in the framework of two-flavor toy model. The parameter  $\xi$  is defined in [7] for the pion rest frame by considering the auxiliary case of absolutely massless neutrinos and denoting the energy of such neutrinos as  $E$ ,

$$\xi = 1/2(1 + m_\mu^2/m_\pi^2), \quad (1)$$

where  $m_\mu$  and  $m_\pi$  are the masses of the muon and the pion. Then for massive (but light!) neutrinos, the authors of [7] get

$$E_{1,2} = E + (1 - \xi)m_{1,2}^2/2E, \quad (2)$$

$$p_{1,2} = E - \xi m_{1,2}^2/2E. \quad (3)$$

Here  $E_{1,2}$ ,  $p_{1,2}$ , and  $m_{1,2}$  are the energies, momenta, and masses of neutrinos, respectively. From the above statement about  $\xi = 0, 1$ , it follows that

$$E_1 = E_2 \text{ for } \xi = 1 \text{ and } p_1 = p_2 \text{ for } \xi = 0. \quad (4)$$

Thus, the equal-energy and equal-momentum assumptions in the form  $\Delta E \equiv E_1 - E_2 = 0$  and  $\Delta p \equiv p_1 - p_2 = 0$ ,

respectively, are treated by the authors of [7] as particular cases of the general kinematic relations (1) and (2):

$$\Delta E = (1 - \xi)\Delta m^2/2E = 0 \text{ for } \xi = 1, \quad (5)$$

$$\Delta p = \xi\Delta m^2/2E = 0 \text{ for } \xi = 0. \quad (6)$$

Unfortunately, both treatment and relations (6)–(8) are erroneous.

On the one hand, the quantity  $\xi$  is not a free parameter. Indeed, it follows from Eq. (5) that  $\xi$  has a fixed value ( $\approx 0.8$ ) for the decay under consideration. On the other hand, it is evident from definitions of  $E$  and  $\xi$  that

$$E = m_\pi(1 - \xi). \quad (7)$$

The parameter  $\xi$  determines sharing of the decay energy. As seen from Eq. (3), the values  $\xi = 0$  and  $\xi = 1$  are senseless because they refer, respectively, to the limiting cases  $E_{\text{recoil}} = 0$  and  $E = 0$ . Therefore, one cannot assume that  $\xi$  can be equal to 1 or 0. Instead, the solution to Eqs. (7) and (8) is the vanishing  $\Delta m^2$ , that is, the absence of oscillations.

I am grateful to L.B. Okun for friendly support. This work was supported by the Russian Foundation for Basic Research, project no. 00-15-96562.

## REFERENCES

1. B. M. Pontecorvo, Zh. Éksp. Teor. Fiz. **53**, 1717 (1967) [Sov. Phys. JETP **26**, 984 (1967)].
2. V. N. Gribov and B. M. Pontecorvo, Phys. Lett. B **28B**, 493 (1969).
3. S. Bilenky and B. Pontecorvo, Phys. Lett. B **61B**, 248 (1976); Lett. Nuovo Cimento **17**, 569 (1976); Comments Nucl. Part. Phys. **7**, 149 (1977).
4. L. B. Okun, Surv. High Energy Phys. **15**, 75 (2000).
5. H. Lipkin, hep-ph/9901399.
6. L. Stodolsky, Phys. Rev. D **58**, 036006 (1998); hep-ph/9802387.
7. C. Giunti and C. W. Kim, hep-ph/0011074.

<sup>1</sup>This article was submitted by the author in English.

## Dependence of Nuclear $Z$ Factor on the Chemical Potential

M. V. Zverev and E. E. Saperstein\*

Russian Research Centre Kurchatov Institute, pl. Kurchatova 1, Moscow, 123182 Russia

\*e-mail: saper@mbslab.kiae.ru

Received March 16, 2001

A simple microscopic formula is derived for the renormalization factor  $Z$  of Green's function on the basis of the self-consistency relation of many-body theory and the Brueckner method. This formula involves the derivative of the Brueckner  $G$  matrix with respect to energy. Based on the analysis of the properties of the  $G$  matrix for a slab of nuclear matter, the  $G$  matrix is approximately replaced by the off-mass-shell  $T$  matrix taken for free  $NN$  scattering at a negative energy  $E$  equal to the doubled chemical potential  $\mu$  of the nucleus under consideration. The  $Z$  factor thus calculated depends strongly on  $\mu$  and decreases with  $|\mu|$ . This effect is important for analyzing the properties of atomic nuclei near the drip line, where  $\mu$  is zero.

PACS numbers: 21.65.+f; 24.10.Cn

The renormalization factor  $Z$  of the one-particle Green's function  $\mathcal{G}(p, \varepsilon)$  of Fermi liquid ( $Z$  factor) is one of the fundamental characteristics of a Fermi system. However, it is eliminated from all observables in the Landau theory of Fermi liquid [1] by means of the renormalization procedure similar to that applied in QED. Only one observable remains—the “Migdal jump” in the momentum distribution of particles  $n(p)$  [2]—that is determined directly by the  $Z$  factor. However, in atomic nuclei, this jump is strongly smeared due to finite range effects [3] and, therefore, can hardly be determined experimentally. Instead, a new important observable appears, which is determined by the  $Z$  factor. This is the one-particle spectroscopic factor  $S_\lambda$ , where  $\lambda$  is a set of quantum numbers of the knocked-out (or added) nucleon. The relationship between  $S_\lambda$  and  $Z$  is the simplest in magic nuclei, where  $S_\lambda$  coincides with the matrix element  $(Z)_{\lambda\lambda}$ .

Theory of finite Fermi systems (TFFS) was developed by Migdal [4] similar to the Landau theory of Fermi liquid and also involves a coordinate-dependent factor  $Z(\mathbf{r})$  that is implicitly present in the amplitude of effective quasiparticle interaction  $\mathcal{F}$ . However, there is a variant of the self-consistent TFFS [5, 6], so-called quasiparticle Lagrangian method, in which the  $Z$  factor is introduced explicitly through one more phenomenological parameter which determines the energy dependence of the effective interaction. The problem of calculating the  $Z$  factor cannot be circumvented when one develops a first-principle nuclear theory based on a free  $NN$  potential. In particular, the effective interaction between nucleons near the Fermi surface (Landau–Migdal amplitude) is expressed in the Brueckner theory [7, 8] in terms of the Brueckner  $G$  matrix, the key

parameter of this approach, through the following formula including the  $Z$  factor in an explicit form:

$$\mathcal{F}(\mathbf{r}_1, \mathbf{r}_2, \mathbf{r}_3, \mathbf{r}_4) = \sqrt{Z(\mathbf{r}_1)Z(\mathbf{r}_2)Z(\mathbf{r}_3)Z(\mathbf{r}_4)}G(\mathbf{r}_1, \mathbf{r}_2, \mathbf{r}_3, \mathbf{r}_4; E = 2\mu). \quad (1)$$

Here,  $E$  is the total energy in the two-particle channel, and  $\mu$  is the chemical potential of the system.

Note that the  $Z$  factor of infinite nuclear matter was calculated in [9, 10] from the dispersion relation for the nucleon mass operator in a nuclear medium. Under rather general assumptions, the  $Z$  factor was expressed in terms of the nuclear response function. It turned out that the  $Z$  factor differs from unity due predominantly to the spin–isospin component of the response function. This component is primarily determined by the Migdal constant  $g'$ . Unfortunately, this method of calculating  $Z$  does not provide extrapolation to loosely bound nuclei near the drip line, which have been intensely studied both experimentally and theoretically in recent years. Indeed, the  $g'$  constant is known only for the nuclear chemical potential  $\mu \approx -8$  MeV that is characteristic of stable nuclei, and its behavior with decreasing  $|\mu|$  is not *a priori* clear.

In this work, we calculate the  $Z$  factor by a different method, which enables us to reveal the dependence of the  $Z$  factor on  $\mu$ . We start with the many-body self-consistency relation [5, 11] between one-particle and two-particle characteristics of the system. This condition follows from the spontaneous violation of the translational invariance and is valid for any finite “self-bound” Fermi system, i.e., which is in bound state in the absence of external fields. This condition relates the

mass operator  $\Sigma$ , effective interaction  $\mathcal{U}$ , and one-particle Green's function  $\mathcal{G}$  to each other and has the form

$$\begin{aligned} & \frac{\partial \Sigma(\mathbf{r}, \mathbf{r}'; \varepsilon)}{\partial \mathbf{R}} \\ &= \int \frac{d\varepsilon'}{2\pi i} d\mathbf{r}_1 d\mathbf{r}'_1 \mathcal{U}(\mathbf{r}, \mathbf{r}', \mathbf{r}_1, \mathbf{r}'_1; \varepsilon, \varepsilon') \frac{\partial \mathcal{G}(\mathbf{r}_1, \mathbf{r}'_1; \varepsilon')}{\partial \mathbf{R}_1}, \end{aligned} \quad (2)$$

where  $\mathbf{R} = (\mathbf{r} + \mathbf{r}')/2$ ,  $\mathbf{R}_1 = (\mathbf{r}_1 + \mathbf{r}'_1)/2$ , and the block  $\mathcal{U}$  of  $NN$  interaction is irreducible in the particle-hole channel and corresponds to zero energy transfer in this channel.

We are interested in the  $Z$  factor, i.e., in the residue of the Green's function  $\mathcal{G}$  at the one-particle pole. More precisely, the  $Z$  factor in a nonuniform system is defined as

$$\mathcal{G}(\mathbf{r}, \mathbf{r}'; \varepsilon) = \sqrt{Z(\mathbf{r})Z(\mathbf{r}')} \mathcal{G}^q(\mathbf{r}, \mathbf{r}'; \varepsilon) + \mathcal{G}^R(\mathbf{r}, \mathbf{r}'; \varepsilon), \quad (3)$$

where  $\mathcal{G}^q(\mathbf{r}, \mathbf{r}'; \varepsilon)$  is the quasiparticle Green's function with unit residue and  $\mathcal{G}^R(\mathbf{r}, \mathbf{r}'; \varepsilon)$  has no poles near the Fermi surface. Following the TFFS [4], we expand the mass operator near the Fermi surface in powers of  $\varepsilon - \mu$  and of the difference between the squared momentum  $\mathbf{p}^2$  and squared Fermi momentum. Retaining only linear terms and using notation from [5], we obtain

$$\begin{aligned} \Sigma(\mathbf{r}, \mathbf{r}'; \varepsilon) &= \left[ \Sigma_0(\mathbf{r}) + \frac{1}{(k_F^0)^2} \mathbf{p} \Sigma_1(\mathbf{r}) \mathbf{p} \right. \\ &\quad \left. + \Sigma_2(\mathbf{r}) \frac{\varepsilon}{\varepsilon_F} \right] \delta(\mathbf{r} - \mathbf{r}'). \end{aligned} \quad (4)$$

Here, normalization quantities  $k_F^0 = \pi^2/mC_0$ , where the standard normalization factor  $C_0 = (dn/d\varepsilon_F)^{-1}$  of the TFFS is equal to the density of states near the Fermi surface, and  $\varepsilon_F^0 = (k_F^0)^2/2m$  are introduced for the components of the mass operator  $\Sigma_i$  to have the same dimensions. In this notation,  $Z(\mathbf{r}) = (1 - \Sigma_2(\mathbf{r})/\varepsilon_F^0)^{-1}$ .

Differentiating Eq. (2) with respect to energy and using local expansion (4), one obtains the following integro-differential self-consistency relation for the  $Z$  factor:

$$\begin{aligned} & \frac{\partial}{\partial \mathbf{r}} (Z^{-1}(\mathbf{r})) = - \int \frac{d\varepsilon'}{2\pi i} d\mathbf{r}_1 d\mathbf{r}'_1 \\ & \times \frac{\partial \mathcal{U}(\mathbf{r}, \mathbf{r}, \mathbf{r}_1, \mathbf{r}'_1; \varepsilon, \varepsilon')}{\partial \varepsilon} \bigg|_0 \frac{\partial \mathcal{G}(\mathbf{r}_1, \mathbf{r}'_1; \varepsilon')}{\partial \mathbf{R}_1}, \end{aligned} \quad (5)$$

where the subscript 0 means that  $\varepsilon = \mu$ . Equation (5) is formally exact. Below, we simplify it by using various approximations, in particular, taking  $\mathcal{U} = G$ , where  $G$  is the Brueckner matrix satisfying the Bethe–Goldstone equation [7, 8], which takes into account two-particle correlations.

In [12], the Bethe–Goldstone equation was solved for a slab of nuclear matter, a simple system simulating heavy spherical nuclei, by using the separable representation [13, 14] of the Paris  $NN$  potential [15] and the mixed coordinate–momentum representation technique [16]. The latter was developed for microscopic consideration of superfluidity in semi-infinite nuclear matter. Some results from [12] were applied in [17] to finite nuclei, for which the coordinate dependence of the scalar–isoscalar component  $f_0(r)$  of the Landau–Migdal amplitude was calculated on the basis of Eq. (1) and the nuclear mean field obtained from Eq. (2). The calculation was based on the fact that the main contribution to the mean field, when calculated using Eq. (2), comes from the nuclear surface region, where, first, the Brueckner theory is accurate enough and, second, some additional approximations can be used. In particular, one can consider only  $s$ -wave scattering and approximate the  $G$  matrix in each of the two  $s$ -wave channels by the expression

$$\begin{aligned} G^S(\mathbf{r}, \mathbf{r}', \mathbf{r}_1, \mathbf{r}'_1; \varepsilon, \varepsilon') &= C_0 \gamma^S(\mathbf{r}; \varepsilon, \varepsilon') \\ &\times \delta(\mathbf{r} - \mathbf{r}') \delta(\mathbf{r} - \mathbf{r}_1) \delta(\mathbf{r}_1 - \mathbf{r}'_1), \end{aligned} \quad (6)$$

where the total spin in the two-particle channel is  $S = 0$  and 1 for the singlet and triplet channels, respectively. The procedure of localization of the  $G$  matrix, Eq. (6), is based on the local-potential approximation proposed in [16]. This procedure requires specification of the nuclear mean field  $V(r)$ , for which, as in [17], we use the Woods–Saxon well with realistic parameters for stable nuclei. For more details, see [12, 16, 17].

The invariant amplitude  $f_0$  corresponds to zero spin and zero isospin in the particle–hole channel and is determined by the following combination of the  $G$  matrices in the two channels:

$$\gamma_f(r, E) = \frac{3}{16} (\gamma_0(r, E) + \gamma_1(r, E)). \quad (7)$$

According to this equation,  $\gamma_f$  depends only on the total energy  $E = \varepsilon + \varepsilon'$ . Under the same approximations,  $\Sigma(\mathbf{r}, \mathbf{r}'; \varepsilon) = \Sigma(\mathbf{r}; \varepsilon) \delta(\mathbf{r} - \mathbf{r}')$  and the mean field has the form

$$V(r) = Z(r) \Sigma(r; \varepsilon = \mu). \quad (8)$$

Taking Eq. (8) into account, one can approximately renormalize Eq. (2) as [5]

$$\frac{d\Sigma(r; \varepsilon)}{dr} = Z(r) C_0 \gamma_f(r; \varepsilon, \mu) \frac{d\rho(r)}{dr}. \quad (9)$$

Equations (8) and (9) provide the following explicit expression for the central part of the nuclear potential in terms of the known renormalization factor  $Z(r)$ :

$$V(r) = -C_0 Z(r) \int_r^\infty ds Z(s) \gamma_f(s; \mu, \mu) \frac{d\rho(s)}{ds}. \quad (10)$$

In [17], Eq. (10) was used to determine the mean field from phenomenological  $Z(r)$ . We demonstrate now that self-consistency relation (9) can be used to find the quantity

$$Z(r) = \left( 1 - \left( \frac{d\Sigma(r, \varepsilon)}{d\varepsilon} \right)_0 \right)^{-1}. \quad (11)$$

Differentiating Eq. (9) with respect to  $\varepsilon$  and using definition (11), we obtain

$$Z^{-1}(r) \frac{dZ^{-1}(r)}{dr} = -C_0 \left( \frac{\partial \gamma_f(r; \varepsilon, \mu)}{\partial \varepsilon} \right)_0 \frac{d\rho(r)}{dr}. \quad (12)$$

This equation can be integrated in the explicit form

$$Z(r) = \left[ 1 + 2C_0 \int_r^\infty ds \left( \frac{\partial \gamma_f(s; \varepsilon, \mu)}{\partial \varepsilon} \right)_0 \frac{d\rho(s)}{ds} \right]^{-1/2}. \quad (13)$$

A simple model of the Landau–Migdal scalar–isoscalar amplitude  $f(r)$  was proposed in [17] on the basis of the analysis of the results from [12]. In this model, the  $G$  matrix is replaced in Eq. (7) by the off-mass-shell  $T$  matrix for free  $NN$  scattering at negative energy  $E = 2\mu$ . The  $T$  matrix satisfies the Lippmann–Schwinger equation

$$T(E) = \mathcal{V} + \mathcal{V} A(E) T(E), \quad (14)$$

where  $\mathcal{V}$  is the free  $NN$  potential and  $A(E)$  is the propagator of two free nucleons with the total energy  $E$ . The  $T$  matrix can be calculated much more simply than the  $G$  matrix, but it rather accurately reproduces the  $G$  matrix when calculating the  $f(r)$  amplitude (Fig. 1). This simple model for the amplitude  $f(r)$  is valid, at least when used under self-consistency relation (10), because of two reasons. First, the property  $G \rightarrow T$  is asymptotically valid beyond the nuclear edge. Second, as is seen from Fig. 1, the magnitude of this asymptotic value is very large and is approximately an order of magnitude larger than the inner values of each of the amplitudes under consideration. Because the basic contribution to Eq. (10) comes from the nuclear surface, where the derivative of density is large, a change in the inner  $f(r)$  value even by a factor of 2 only slightly affects the result of calculation of the mean field. Note that this model does not apply to the other invariant components of the Landau–Migdal amplitude, in particular, to the scalar–isoscalar amplitude  $f'$ .

In this work, we approximately calculate the  $Z$  factor from Eq. (13) using the same approximation for the derivative of the scalar–isoscalar amplitude  $f$  with respect to the energy. This substitution is indirectly justified by the fact that, as is shown in [17], this approximation holds for  $f$  even upon varying the nuclear chemical potential  $\mu$ . Thus, we replace  $\gamma_f$  in Eq. (13) by  $t_f$ , i.e., by the combination for the free  $T$  matrix similar to Eq. (7). Apart from the quantities calculated in [12, 17], Eq. (13) involves a new quantity—the derivative of the  $T$  matrix

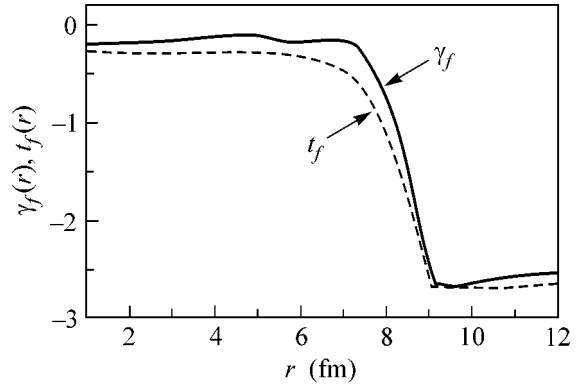


**Fig. 1.** Scalar–isoscalar combinations of the (solid line)  $\gamma_f(r)$  and (dashed line)  $t_f(r)$  components of the  $G$  and  $T$  matrices, respectively.

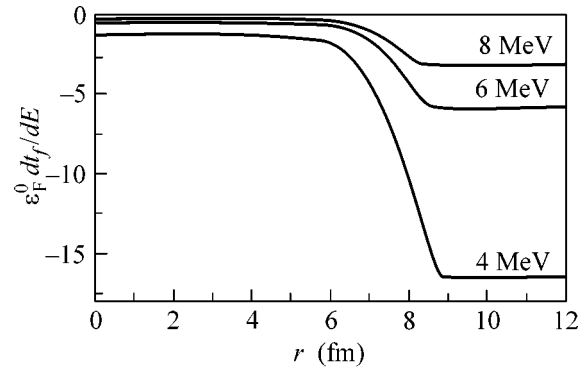


**Fig. 2.** Dimensionless derivative  $\varepsilon_F^0 \partial t_f / \partial E$  of the scalar–isoscalar component of the Landau–Migdal amplitude calculated for different values of chemical potential. The  $|\mu|$  values are indicated above the lines.

with respect to energy. The equation for this derivative can easily be obtained from Eq. (14); it has the form

$$\frac{\partial T(E)}{\partial E} = \mathcal{V} \frac{\partial A(E)}{\partial E} T(E) + \mathcal{V} A(E) \frac{\partial T(E)}{\partial E}. \quad (15)$$

The method for solving this equation and the way of local representation in form of Eq. (6) are completely analogous to those used in [12, 17] for the  $T$  matrix.

The dimensionless  $\varepsilon_F^0 \partial t_f(r, E) / \partial E$  combination similar to Eq. (7) is shown in Fig. 2 for the chemical potential  $\mu = -8$  MeV typical of stable nuclei and for somewhat smaller  $|\mu|$  values corresponding to approaching the boundary of nucleon stability. The calculation was performed with the following parameters of the Woods–Saxon potential: the depth  $V_0 = 50$  MeV; the radius  $R_p = r_0 A^{1/3}$ , where  $r_0 = 1.24$  fm and  $A$  is the number of nucleons in a nucleus ( $A = 200$  was taken in the calculation); and the diffuseness parameter  $b = 0.65$  fm. As is seen, the qualitative behavior of this derivative is similar to that of  $t_f(r)$ : the outer magnitude is considerably larger

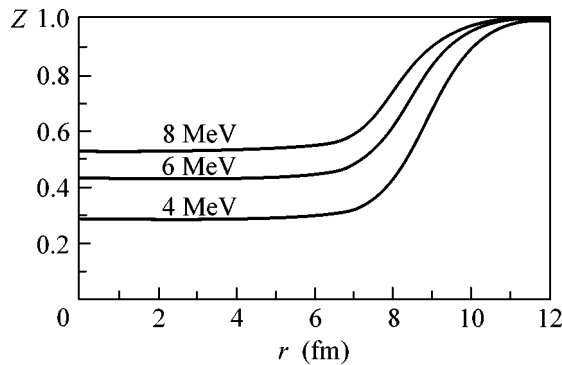


Fig. 3.  $Z$  factor for various values  $|\mu|$  indicated above the lines.

in absolute value than the inner magnitude. For this reason, the substitution of  $\partial$  in Eq. (13) is qualitatively justified.

For calculating the  $Z$  factor from Eq. (13), it is necessary to know the derivative of density  $d\rho/dr$ . As in [17], the density was specified by the Fermi function with radius  $R_d = R_p - \delta R$ , where  $\delta R = 0.5$  fm, and the diffuseness parameter identical to that for the potential. The calculation by Eq. (13) was performed with the same  $\mu$  values as above. The fact that the  $Z$  value in the nuclear interior at  $\mu = -8$  MeV (Fig. 3) is considerably smaller than the known experimental value  $Z_{\text{exp}} = 0.8 \pm 0.05$  [5] is not surprising because of the crude approximations used. As is seen, the error introduced into the calculated  $f$  amplitude [17] by the substitution of the  $T$  matrix for the  $G$  matrix is smaller than for the calculated derivative with respect to energy. Among the necessary refinements, the direct calculation and use of the derivative of  $G$  matrix with respect to energy, instead of its replacement by the derivative of  $T$  matrix in Eq. (13), should be the first step. The calculation of the corrections to the Brueckner theory is a more complicated problem (see, e.g., [18, 19]), but one can expect that these corrections are less significant because they are more important in the inner nuclear region, which makes only small contribution to integral (13).

As is seen, the  $Z$  factor decreases noticeably with  $|\mu|$ . The reason is quite clear: both amplitude  $t_f$  and its derivative with respect to energy in Eq. (13) increase on approaching the poles (real in the triplet channel and virtual in the singlet channel). Clearly, this reason will hold to some extent after the above-mentioned refinements of the calculation. We restricted our consideration to the values  $|\mu| \geq 4$  MeV because the calculation of the  $Z$  factor by this method becomes doubtful for smaller  $|\mu|$  values. Indeed, such a sizable decrease in

$Z$  implies a considerable rearrangement of the system, so that the variation in the quantities such as mean field  $V(r)$  and density  $\rho(r)$  should be taken into account self-consistently, i.e., by including the variation in  $Z$  as well. This calculation will be performed in a separate work.

This work was supported by the Russian Foundation for Basic Research, project nos. 00-02-17319 and 00-15-96590.

## REFERENCES

1. L. D. Landau, Zh. Éksp. Teor. Fiz. **35**, 97 (1958) [Sov. Phys. JETP **8**, 70 (1958)].
2. A. B. Migdal, Zh. Éksp. Teor. Fiz. **32**, 399 (1957) [Sov. Phys. JETP **5**, 333 (1957)].
3. M. V. Zverev and E. E. Saperstein, Yad. Fiz. **43**, 304 (1986) [Sov. J. Nucl. Phys. **43**, 195 (1986)].
4. A. B. Migdal, *Theory of Finite Fermi Systems and Applications to Atomic Nuclei* (Nauka, Moscow, 1965; Interscience, New York, 1967).
5. V. A. Khodel and E. E. Saperstein, Phys. Rep. **92**, 183 (1982).
6. A. B. Migdal, *Theory of Finite Fermi Systems and Applications to Atomic Nuclei* (Nauka, Moscow, 1983, 2nd ed.).
7. H. A. Bethe, Annu. Rev. Nucl. Sci. **21**, 93 (1971).
8. P. Ring and P. Schuck, *The Nuclear Many-Body Problem* (Springer-Verlag, Berlin, 1980).
9. E. E. Sapershtein and S. V. Tolokonnikov, Pis'ma Zh. Éksp. Teor. Fiz. **68**, 529 (1998) [JETP Lett. **68**, 553 (1998)].
10. E. E. Saperstein and S. V. Tolokonnikov, Yad. Fiz. **62**, 1383 (1999) [Phys. At. Nucl. **62**, 1302 (1999)].
11. S. A. Fayans and V. A. Khodel', Pis'ma Zh. Éksp. Teor. Fiz. **17**, 633 (1973) [JETP Lett. **17**, 444 (1973)].
12. M. Baldo, U. Lombardo, E. E. Saperstein, and M. V. Zverev, Yad. Fiz. **64**, 247 (2001) [Phys. At. Nucl. **64**, 203 (2001)].
13. J. Haidenbauer and W. Plessas, Phys. Rev. C **30**, 1822 (1984).
14. J. Haidenbauer and W. Plessas, Phys. Rev. C **32**, 1424 (1985).
15. M. Lacombe, B. Loiseaux, J. M. Richard, *et al.*, Phys. Rev. C **21**, 861 (1980).
16. M. Baldo, U. Lombardo, E. E. Saperstein, and M. V. Zverev, Nucl. Phys. A **628**, 503 (1998).
17. M. Baldo, U. Lombardo, E. E. Saperstein, and M. V. Zverev, Yad. Fiz. **64**, 509 (2001) [Phys. At. Nucl. **64**, 454 (2001)].
18. J. Wambach, T. L. Ainsworth, and D. Pines, Nucl. Phys. A **555**, 128 (1993).
19. H.-J. Schulze, J. Cugnon, A. Lejeune, *et al.*, Phys. Lett. B **375**, 1 (1996).

Translated by R. Tyapaev

## Temperature Effect on the Decay Periods of Long-Lived $^{180m}\text{Hf}$ and $^{87m}\text{Sr}$ Isomers

V. G. Alpatov, Yu. D. Bayukov, A. V. Davydov\*, Yu. N. Isaev, G. R. Kartashov,  
M. M. Korotkov, and V. M. Samoylov

State Scientific Center of the Russian Federation Institute for Theoretical and Experimental Physics,  
ul. Bol'shaya Cheremushkinskaya 25, Moscow, 117259 Russia

\* e-mail: [Andrey.Davydov@itep.ru](mailto:Andrey.Davydov@itep.ru)

Received March 20, 2001

Experiments on measuring the decay periods of long-lived  $^{180m}\text{Hf}$  and  $^{87m}\text{Sr}$  isomers at room temperature and at 77 K in massive samples of  $\text{HfO}_2$ ,  $\text{Sr}(\text{NO}_3)_2$ , and  $\text{SrCO}_3$  are reported. The isomeric nuclear states were excited by irradiating the samples with neutrons from a Pu–Be source. According to the theory of V.I. Vysotskiĭ *et al.*, the  $T_{1/2}$  value must increase if a  $\gamma$ -active nucleus is surrounded by many identical ground-state nuclei, because these distort the spectrum of electromagnetic vacuum oscillations near the nuclear energy level. As the temperature of the sample decreases,  $\gamma$ -ray lines narrow, especially for the low-energy Mössbauer transitions, thereby enhancing the resonance effect on the spectrum of vacuum oscillations. For the  $^{180m}\text{Hf}$  isomer, whose upper  $\gamma$  transition carries away 57.55 keV, the  $T_{1/2}$  value was found to increase by  $2.99 \pm 0.87\%$  upon sample cooling. For  $^{87m}\text{Sr}$ , whose decay scheme has no Mössbauer lines, the relative change in  $T_{1/2}$  was found to be  $0.77 \pm 0.53\%$ . © 2001 MAIK “Nauka/Interperiodica”.

PACS numbers: 21.10.Tg

It has become evident from the Mössbauer experiment on  $^{109}\text{Ag}$  [1] that the relevant  $\gamma$ -ray line (88 keV) is scarcely broadened, if at all. The broadening factor lies in the range from 1 to 3 with 67% probability, and it is not improbable that this factor is even less than unity, indicating  $\gamma$ -ray line narrowing. In the works of Vysotskiĭ *et al.* [2–4], the effect of the resonant environment on the gamma-decay probability of excited nuclei is discussed in terms of a mechanism in which the spectrum of electromagnetic vacuum oscillations near the  $\gamma$  source is distorted by introducing in this spatial region a massive sample containing the same nuclei in the ground state. Since, according to the authors of [2–4], it is precisely the vacuum oscillations which are responsible for the gamma decay, the weakening of the spectrum of vacuum oscillations in the region of nuclear resonance results in a decrease in the gamma-decay probability and ensuing narrowing of the  $\gamma$ -ray emission line.

In our experiment on the decay of excited  $^{109m}\text{Ag}$  nuclei [1], the situation is just that corresponding to conditions for the occurrence of the effect of Vysotskiĭ *et al.* A  $\gamma$  source is a single-crystal silver plate, into which a mother nuclide  $^{109}\text{Cd}$  was intruded by thermal diffusion. It decays into the excited  $^{109m}\text{Ag}$  nucleus, which, being surrounded by silver atoms, among which the  $^{109}\text{Ag}$  isotope is in a 48.2% abundance, should experience, according to the theory of Vysotskiĭ *et al.*, the distorted spectrum of vacuum oscillations.

To directly ascertain that the gamma-decay probability of the  $^{109m}\text{Ag}$  nuclei indeed decreases in a massive

silver sample, one should compare the decay kinetics measured for these nuclei in a massive silver  $\gamma$  source with analogous kinetics in a silver-free radioactive  $^{109}\text{Cd}$  sample. To implement the first variant, an experiment on  $\gamma$ -resonance activation of silver nuclei should be carried out similar to experiment [5], but with a source prepared not on a cyclotron but using a sparing technique of intruding  $^{109}\text{Cd}$  into a silver single crystal through thermal diffusion. If the  $\gamma$ -ray line only slightly broadens or not at all, then one will obtain a much stronger, than in [5], silver activation effect with a much weaker  $\gamma$  source. This would allow the decay law to be measured with a good accuracy for the excited isomeric state of  $^{109}\text{Ag}$ . The second experiment should be carried out using very weak  $^{109}\text{Cd}$  activities in the absence of traces of silver.

Inasmuch as the setup for implementing the experiments on gamma activation of the  $^{109}\text{Ag}$  nuclei is presently unavailable to us, we could not accomplish direct measurements of the mean lifetimes for the isomeric states of these nuclei in the presence of a resonant environment. For this reason, the experiments were carried out with other isomers, namely,  $^{180m}\text{Hf}$  and  $^{87m}\text{Sr}$ . The decay schemes for these isomers are shown in Fig. 1. For the decay period of the  $^{180m}\text{Hf}$   $8^-$  state to be affected by the resonant environment, it is necessary that the  $^{180}\text{Hf}$  nuclei of this environment be in the  $8^+$  state. Then, their action on the spectrum of vacuum oscillations near the line at 57.55 keV will be similar to the effect of ground-state two-level nuclei. This effect can be

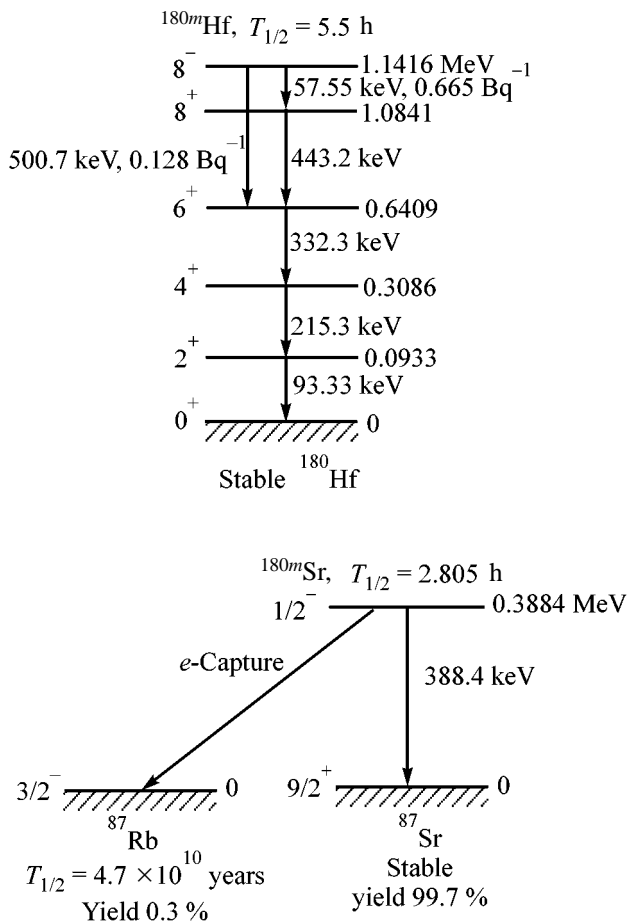


Fig. 1. Decay schemes for the  $^{180m}\text{Hf}$  and  $^{87m}\text{Sr}$  isomers.

imagined as an unobservable exchange of virtual photons between nuclei and vacuum oscillations. If such an exchange takes place, then the multistep sequential virtual excitation of the energy levels of the  $^{180}\text{Hf}$  isomer becomes possible and some of these nuclei may occur in the virtual  $8^+$  state with a nonzero probability. On cooling the massive hafnium  $\gamma$  source, the widths of all lines in the  $\gamma$ -ray cascade originating at 57.55 keV will decrease. In this case, a certain fraction of gamma intensity at 93.3 and 57.55 keV will undergo very strong Mössbauer narrowing, while the Doppler widths of higher energy lines will diminish (by approximately a factor of two upon passing from room temperature to 77 K). This narrowing must result in a strong distortion of the spectrum of vacuum oscillations in the resonance region near the 57.55-keV transition, which, in turn, would have an effect on the decay period of the  $8^-$  state.

With the  $^{87m}\text{Sr}$  isomer, the  $\gamma$ -line energy is too large (388.4 keV) for the Mössbauer effect to be detectable. Because of this, the  $\gamma$ -ray line of the strontium source changes only its Doppler width on cooling. Hence, it is expected that a decrease in  $T_{1/2}$  for  $^{87m}\text{Sr}$  should be less pronounced than for  $^{180m}\text{Hf}$ .

The experimental setup for checking the validity of these premises is very simple. A metallic vessel is placed inside a foam plastic thermal shield, and a massive sample of the substance of interest containing nuclei in the isomeric state is put at the vessel bottom. A Ge(Li) detector connected to a Nokia LP 4900B pulse-amplitude analyzer is placed underneath this primitive cryostat. Samples of  $\text{HfO}_2$  (19 g) and  $\text{Sr}(\text{NO}_3)_2$  (20 g) in 35-mm-i.d. fluoroplastic ampoules were used. For each sample, the experiment was conducted as follows. The sample was exposed overnight to neutrons from a Pu–Be source with an intensity of  $\sim 2 \times 10^7$  neutron/s. The isomer was formed both by the  $(n, \gamma)$  reaction of slow neutrons with the  $^{179}\text{Hf}$  or  $^{86}\text{Sr}$  isotope and as a result of inelastic scattering of fast neutrons by the  $^{180}\text{Hf}$  and  $^{87}\text{Sr}$  isotopes. The decay period of the isomer was measured by the Ge(Li) detector for the next day. If, on a certain day, the measurements were performed at room temperature, then the next day they would be performed at 77 K, for which purpose liquid nitrogen was poured into the metallic vessel with the sample. For hafnium, the decay periods were determined using the lines at 215.3-, 332.3-, and 443.2-keV separately, whereupon the results were averaged.

One of the main problems arising in the data processing was associated with choosing the most correct method of determining gamma intensities for the 215.3-, 332.3-, and 443.2-keV lines of the  $^{180m}\text{Hf}$  isomer and the 388.4-keV line of the  $^{87m}\text{Sr}$  isomer. Simultaneously with  $^{180m}\text{Hf}$ , the other long-lived radioactive hafnium isotopes are formed upon exposing a hafnium sample with natural isotope abundance to neutrons; these isotopes also contribute to the measured  $\gamma$ -ray spectrum. As a result, the  $\gamma$ -ray lines listed above have rather high pedestals produced by low-energy “tails” of the lines due to  $^{180m}\text{Hf}$  and other  $\gamma$ -ray emitting hafnium isotopes. Among these, the greatest contribution to the pedestals comes from  $^{181}\text{Hf}$ , which undergoes  $\beta$  decay with a half-life  $T_{1/2} = 42.4$  days, and from  $^{175}\text{Hf}$ , which decays through electron capture with a half-life of 70 days. The most intense line of  $^{181}\text{Hf}$  (more precisely, of its decay product  $^{181}\text{Ta}$ ) occurs at 482 keV and, hence, contributes to the pedestals under all three  $^{180m}\text{Hf}$  lines. In the  $\gamma$ -ray spectrum of  $^{175}\text{Hf}$ , the main role is played by the line at 343.4 keV, which is emitted in 86.9% of all decay events and contributes to the pedestals under the 215.3- and 332.3-keV lines.

Several methods of separating  $\gamma$ -ray peaks from pedestals were tested. The first was as follows. Each peak was assigned a finite energy interval with a margin (i.e., covering some portions of the pedestal to the left and right of the peak), and the same intervals were taken on both sides of the peak. Gamma intensity was calculated as the difference between the number of counts in the peak’s interval and one-half of the number of counts in the left and right portions of the pedestal. This method, e.g., was employed for data processing in

[6, 7]. Its drawback is that the left (low-energy) portion of the pedestal contains a certain number of counts that are related to the peak. For this reason, the resulting gamma intensity proves to be underestimated. Subsequently, two other methods of pedestal determination were tested with the use of only the right (high-energy) portion of the spectrum. The first of these methods consisted in a linear least-squares fit to the right portion of the pedestal followed by the extrapolation of the resulting straight line to the region under the peak. This method was suitable for the lines at 215.3 and 443.2 keV but not for the 332.3-keV peak because of the presence of energetically close  $^{175}\text{Hf}$  343.4-keV and  $^{181}\text{Hf}$  345.8-keV lines above it. For this reason, the pedestal under the 332.3-keV peak was determined by averaging the number of counts in eight analyzer channels above the peak energy. However, the error in determining the peak area by this method was too large primarily because of the error in the calculated line slope, which is close to zero. We eventually adopted the second method of data processing. This method consisted in mere averaging of the number of counts in a relatively small number of channels ( $\sim 20$  for the peaks at 215.3 and 443.2 keV and eight for the peak at 332.3 keV; note that the maximum of a peak at 443.2 keV fell on channel no. 1065), followed by subtracting the resulting average value from the number of counts in each channel under the peak. The validity of such an averaging procedure was confirmed by the chi-square statistics.

A total of two measurement runs were conducted for each isomer. In the first run with  $^{180m}\text{Hf}$ , the decay period of the isomer was measured five times at each temperature, with the duration of each measurement being 9–10 h. The results are

$$\begin{aligned} 293 \text{ K: } T_{1/2} &= 5.471 \pm 0.043 \text{ h,} \\ 77 \text{ K: } T_{1/2} &= 5.655 \pm 0.042 \text{ h,} \\ \Delta T_{1/2}/T_{1/2} &= 3.4 \pm 1.1\%. \end{aligned}$$

For  $^{87m}\text{Sr}$ , the following relative change in  $T_{1/2}$  was obtained upon passing from room temperature to 77 K in the first run:

$$\Delta T_{1/2}/T_{1/2} = -1.1 \pm 2.0\%.$$

In the second run, the thickness of a heat-insulating foam plastic layer under the metallic vessel in which the  $\gamma$  sources were placed was slightly increased. As a result, the distance from the source to the detector also slightly increased and the counting rate declined accordingly. Since the durations of the first and the second experiments with  $^{180m}\text{Hf}$  were the same, the error of the second result was slightly greater than that of the first one. The relative change in  $T_{1/2}$  on passing from 273 to 77 K was found to be

$$\Delta T_{1/2}/T_{1/2} = 2.4 \pm 1.4\%.$$

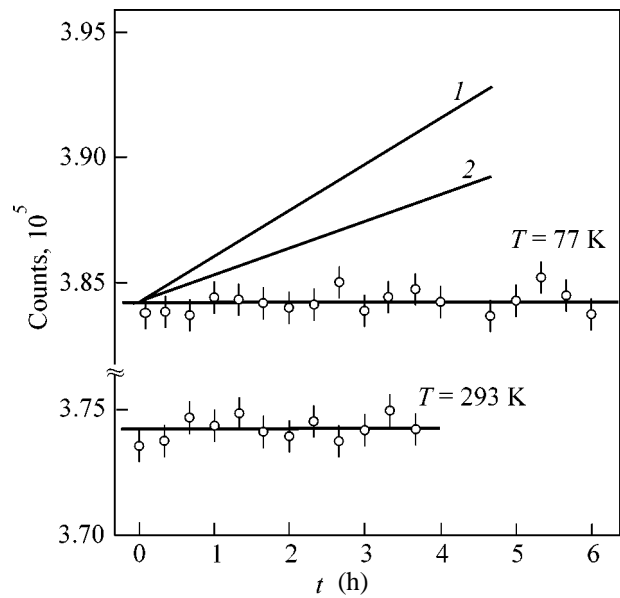


**Fig. 2.** Counting rates vs. time  $t$  in the control experiment with a thin  $\gamma$  source ( $^{57}\text{Co}$  in a silver foil) at room temperature and at 77 K. Lines 1 and 2 show how the counting rates would change at 77 K in the first and second experimental runs, respectively, if the observed growth in  $T_{1/2}$  of the  $^{180m}\text{Hf}$  isomer was due to gradual drawing of the  $\gamma$  source and detector together because of a slow contraction of foam plastic upon cooling.

The averaging of the mutually consistent results of the two experiments with  $^{180m}\text{Hf}$  gave the following value:

$$\Delta T_{1/2}/T_{1/2} = 2.99 \pm 0.87\%.$$

To make sure that the observed change in the  $^{180m}\text{Hf}$   $T_{1/2}$  was not the result of drawing the  $\gamma$  source and detector together due to a very slow contraction of the lower foam plastic layer upon its cooling by liquid nitrogen that was poured into the cryostat, the following control experiment was carried out. A silver foil  $\gamma$  source with  $^{57}\text{Co}$  nuclides intruded in it was put under the fluoroplastic container with a nonactivated sample of hafnium oxide. The counting rates for the 122-keV  $\gamma$ -ray quanta from this source were measured for a rather long time at room temperature and at 77 K. The results of measurements are presented in Fig. 2. The counting rate is seen to be stable at both temperatures. The effect of drawing the  $\gamma$  source and detector together might be invoked for explaining the observed growth of  $T_{1/2}$  in the first and second experimental runs with hafnium only if the experimental points obtained at 77 K fell on lines 1 and 2, respectively. One can see that this explanation of a rise in  $T_{1/2}$  does not work. However, the possibility of the  $\text{HfO}_2$  powder very slowly settling inside the container at 77 K still exists (note that this does not occur with the strontium samples). For this reason, it would be profitable to

carry out analogous experiments with monolithic samples of metallic hafnium.

The second experiment with the  $^{87m}\text{Sr}$  isomer was carried out using the 50- and 38-g samples of  $\text{SrCO}_3$ . Measurements were conducted continuously for 10 days alternately for both samples with periodically changing temperature conditions. Each measurement of  $T_{1/2}$  took 6 h. The following value was obtained for the relative change in  $^{87m}\text{Sr}$   $T_{1/2}$  upon passing from 293 to 77 K in the second run:

$$\Delta T_{1/2}/T_{1/2} = 0.82 \pm 0.54\%.$$

Together with the results of the first experiment, this gives for  $^{87m}\text{Sr}$

$$\Delta T_{1/2}/T_{1/2} = 0.77 \pm 0.53\%.$$

Therefore, the data of our experiments with  $^{180m}\text{Hf}$  and  $^{87m}\text{Sr}$  are in qualitative agreement with the aforementioned model predictions, and it is reasonable to assume that this effect should be observed in our experiments with the  $^{109m}\text{Ag}$  isomer, so that the narrowing of the  $\gamma$ -ray line in these experiments is quite possible. Notice that analogous effects were observed in [8–11].

The second experimental run with  $^{180m}\text{Hf}$  and  $^{87m}\text{Sr}$  was supported by the INTAS, grant no. 97-31566.

#### REFERENCES

1. V. G. Alpatov, Yu. D. Bayukov, V. M. Gelis, *et al.*, *Laser Phys.* **10**, 952 (2000).
2. V. I. Vysotskiĭ, V. I. Vorontsov, and R. N. Kuz'min, *Pis'ma Zh. Tekh. Fiz.* **10**, 300 (1984) [*Sov. Tech. Phys. Lett.* **10**, 126 (1984)].
3. V. I. Vysotskiĭ, in *Technical Digest of 1st International Induced Gamma Emission Workshop, PC-IGE Foundation, Bucharest, 1997*, p. 81.
4. V. I. Vysotskiĭ, *Phys. Rev. C* **58**, 337 (1998).
5. G. E. Bizina, A. G. Beda, N. A. Burgov, and A. V. Davydov, *Zh. Éksp. Teor. Fiz.* **45**, 1408 (1963) [*Sov. Phys. JETP* **18**, 973 (1964)].
6. V. G. Alpatov, Yu. D. Bayukov, A. V. Davydov, *et al.*, in *Collection of Scientific Works of Scientific Session of Moscow Engineering Physics Institute-2000, Moscow, 2000*, Vol. 7, p. 211.
7. V. G. Alpatov, Yu. D. Bayukov, A. V. Davydov, *et al.*, in *Proceedings of the 50th Conference on Nuclear Spectroscopy and Structure of Atomic Nucleus, St. Petersburg, 2000*, p. 193.
8. V. I. Vysotskiĭ, V. P. Bugrov, A. A. Kornilova, *et al.*, *Hyperfine Interact.* **107**, 277 (1997).
9. S. K. Godovikov, *Pis'ma Zh. Éksp. Teor. Fiz.* **68**, 599 (1998) [*JETP Lett.* **68**, 629 (1998)].
10. S. K. Godovikov, *Laser Phys.* **10**, 1293 (2000).
11. V. I. Vysotskiĭ, A. A. Kornilova, A. A. Sorokin, and S. I. Reĭman, *Program and Abstracts of the International Conference "Mössbauer Effect: Magnetism, Material Science, Gamma Optics," Kazan, 2000*, p. 99.

*Translated by V. Sakun*

## Focusing of a Nonlinear Phase-Conjugate Ultrasonic Wave Transmitted through a Phase-Inhomogeneous Layer

A. P. Brysev\*, F. V. Bunkin, R. V. Klopotov, L. M. Krutyanskiĭ, and V. L. Preobrazhenskii

*Wave Research Center of the General Physics Institute, Russian Academy of Sciences, Moscow, 119991 Russia*

\* e-mail: brysev@orc.ru

Received February 28, 2001

The propagation of a nonlinear phase-conjugate ultrasonic wave through a layer introducing random phase aberrations is studied experimentally. The wave is generated by an overthreshold parametric phase-conjugating ultrasonic amplifier. It is shown that, with the extent of nonlinearity achieved for the conjugate wave, the phase locking of harmonics is retained and, as a consequence, a compensation of the distortions introduced by the layer takes place. The possibility of an automatic focusing of a nonlinear phase-conjugate wave propagating in an inhomogeneous medium is demonstrated, which is important for practical applications. © 2001 MAIK "Nauka/Interperiodica".

PACS numbers: 43.25.Jh

It is well known that phase conjugation provides a possibility for an automatic focusing of wave beams on objects placed in both homogeneous media and inhomogeneous media introducing considerable phase aberrations in the wave field [1]. In recent years, the phase-conjugation focusing has become an object of intensive experimental studies in acoustics [2–6]. This fact is related to the development of effective methods of phase conjugation for ultrasonic waves [5, 7–9], as well as to the prospects for the applications of phase conjugation in medical diagnostics and nondestructive testing. One of the most interesting methods of the phase conjugation of ultrasonic waves is the parametric phase conjugation of waves above the absolute instability threshold in a solid, which provides a giant amplification of the conjugate wave relative to the incident one [10]. The possibility of using this method for phase-conjugation focusing of ultrasound in solids and in liquid media was demonstrated experimentally [2, 11]. In other experiments, such effects as the self-targeting of acoustic beams at regular and random scattering objects in liquid [3, 12] and the compensation of phase distortions at the carrier frequency of the conjugated wave [13] were observed. The high intensity of the conjugate wave under conditions of giant parametric amplification provides a possibility to study the specific features of the self-focusing of acoustic beams in the case of their nonlinear propagation. The focusing of nonlinear phase-conjugate beams in a homogeneous medium was considered in recent publication [14]. At the same time, the question about the possibility of the compensation of phase distortions in the case of phase-conjugate beam focusing under conditions of amplification and nonlinear propagation remained a matter of discussion. One of the recent publications [15] reported on the compensation of phase

aberrations of an image obtained at the second harmonic of the conjugate wave in an acoustic microscope on the basis of a parametric phase-conjugating amplifier.

In this paper, we report on the results of the direct measurements of the field structure produced by a focused phase-conjugate ultrasonic wave propagating in a phase-inhomogeneous medium under conditions of a well developed nonlinearity. We present the amplitude distributions for the first four harmonics and the distributions of the rms pressure in the focal plane and along the beam axis. We discuss the mechanism of the phase locking of harmonics in the case of the self-focusing of a nonlinear conjugate wave.

The experiment is schematically illustrated in Fig. 1. A spherically focused ultrasonic source  $S$  with a focal length of 82 mm and a diameter of 27 mm was placed in a water-filled tank. The ultrasonic beam diverging from the focal region was characterized by a carrier frequency of 5 MHz and a pulse duration of 30  $\mu$ s. The beam was directed at an overthreshold parametric phase-conjugating amplifier made on the basis of magnetostrictive ceramics [7, 16]. The amplifier was placed at a distance of 206 mm from the source and had an operating aperture 36 mm in diameter. The conjugate wave generated by the amplifier at the same frequency propagated in the backward direction, through the focus toward the source. In the pulsed-periodic mode of operation used in the experiment, the bursts of incident and conjugate waves propagating in water were separated in time. The appropriate time gating allowed us to perform the measurements for a selected wave train. The acoustic field in water was measured by a acoustically transparent broadband membrane PVDF hydrophone  $H$  with an active element 0.5 mm in diameter. The positioning of

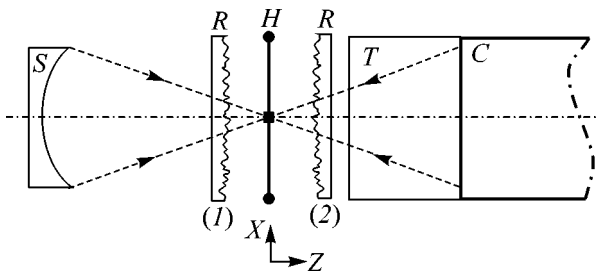


**Fig. 1.** Simplified schematic representation of the experiment. The dashed lines show the propagation of the incident and conjugate acoustic waves in the absence of the layer. The notation is as follows: *S* is the ultrasonic radiator, *C* is the phase-conjugating amplifier, *T* is the metal tube, *H* is the membrane-type hydrophone, *R* is the phase layer, (1) and (2) are the positions of the layer, and *X* and *Z* are the axes of the hydrophone positioning.

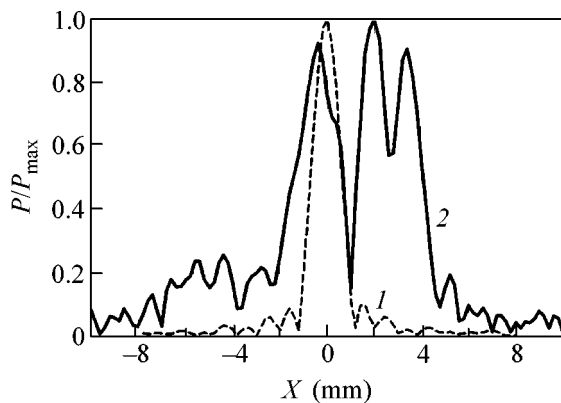


**Fig. 2.** Focal distribution of the normalized pressure amplitude in the incident wave (1) in the absence of the phase layer and (2) with the phase layer set in position (1); *X* is the distance from the beam axis.

the hydrophone was performed using an automated *XZ* system with an accuracy of 0.2 mm. At each point of the field, the measuring system averaged the hydrophone signal over 32 samples and determined the peak and the rms pressure values and the amplitudes of the first four spectral components. At the focus, the amplitude of the incident wave was  $2.44 \times 10^5$  Pa and the level of the second harmonic did not exceed  $-25$  dB relative to the fundamental harmonic, which allowed us to consider the beam propagation as practically linear.

The inhomogeneous medium was represented by a specially designed layer *R* of a silicone polymer. The acoustic parameters of the layer material were as follows: the density  $850 \text{ kg/m}^3$ , the sound velocity  $1160 \text{ m/s}$ , and the attenuation  $6 \text{ dB/cm}$  at a frequency of  $5 \text{ MHz}$ . One side of the layer was flat, and the other had random surface irregularities in the form of irregular pyramids. The dimensions of the bases of these pyramids and the pyramid heights were within  $2\text{--}5 \text{ mm}$ . Hence, the difference in the phase shifts in water and in the layer, e.g.,

at a distance of  $3 \text{ mm}$ , was greater than  $4\pi$ . The acoustic impedance of the layer provided a sufficiently good acoustic matching with water. Taking into account the relatively small thickness of the layer, we can assume that the distortions introduced in the acoustic beam were mainly concerned with the phase, while the contribution of the amplitude loss was insignificant.

To study the ability of the layer to introduce distortions in the propagating wave so that these distortions are noticeable at a given distance, we placed the layer in the position denoted as position (1) in Fig. 1. The distance from the flat surface to the focus was  $20 \text{ mm}$ . In these conditions, we measured the field produced by the radiator in the focal plane. The typical curve obtained from these measurements is shown in Fig. 2. For comparison, Fig. 2 also shows the focal distribution of the field in the absence of the layer. One can see that the presence of the layer strongly affects the distribution typical of a spherical beam and destroys the focusing. Multiply repeated measurements with the layer being shifted without changing its orientation and the distance to the source provided similar results, which testified to the destruction of the focus and differed in the positions, shape, and number of peaks in the curves. Thus, the experiment demonstrated the satisfactory quality of the layer as a medium introducing phase aberrations.

For the experiments with a phase-conjugate wave, the phase layer was shifted from position (1) to position (2) symmetric with respect to the focus. In this geometry, the aberrations were introduced into the incident wave after its propagation through the focal region. Since, in this case, a strong stochastic defocusing was observed, it was necessary to eliminate the loss caused by the part of the scattered beam falling outside the aperture of the phase-conjugating amplifier. For this purpose, between the layer and the amplifier, we placed a metal tube *T* with an inner diameter  $36 \text{ mm}$  and a length of  $101 \text{ mm}$ , which played the role of an acoustic waveguide. Experiments showed that, in the absence of this tube, the reproduction of the spatial structure of the field produced by the incident beam failed.

The results obtained by measuring the field of a phase-conjugate beam along the axis are shown in Fig. 3. The dotted lines show the position of the layer. The scanning region began immediately from the layer and was  $30 \text{ mm}$  long. For comparison, the dashed line shows the pressure distribution in the incident wave. The time profile of the conjugate wave taken at the initial point of scanning is shown on the lower right of Fig. 3a. One can see that, at the left boundary of the layer, the conjugate wave is obviously nonlinear: the amplitudes of the second, third, and fourth harmonics reach  $18$ ,  $8$ , and  $4\%$  of the first harmonic amplitude, respectively. On the whole, the longitudinal profile of the conjugate beam adequately reproduces the profile of the incident beam.

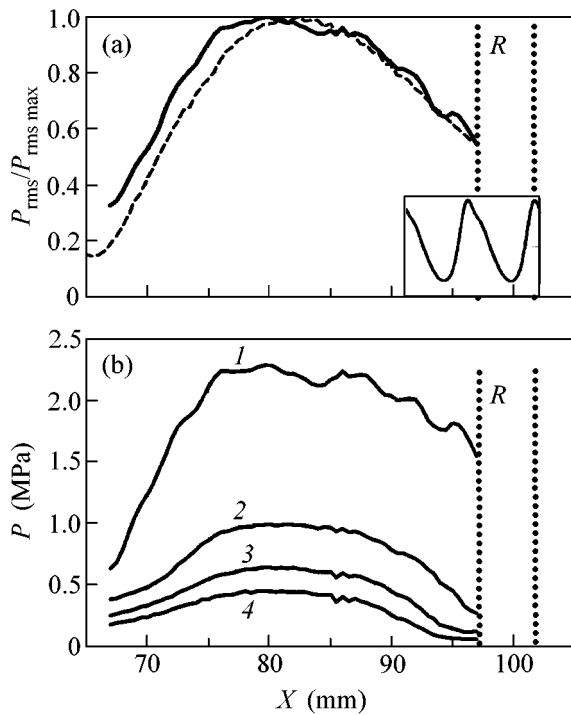


**Fig. 3.** Distribution of the sound pressure along the beam axis: (a) the normalized mean effective value and (b) the amplitudes of the first four harmonics. The solid curves correspond to the conjugate wave, and the dashed curve corresponds to the incident wave. The dotted lines indicate the position of the phase layer  $R$ ; the numbers 1–4 indicate the harmonic numbers;  $Z$  is the distance from the source. The inset (a) shows the conjugate wave form at the beam axis at the point  $Z = 97$  mm.

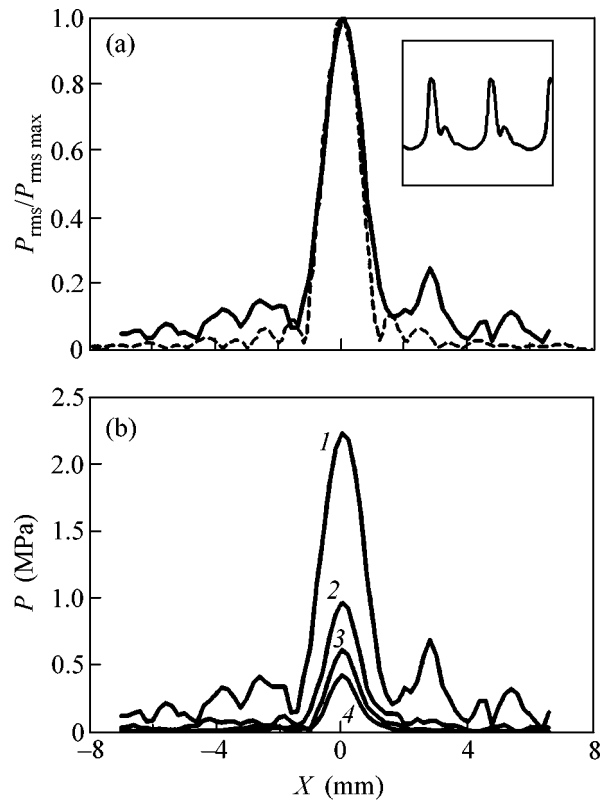


**Fig. 4.** Focal distribution of the sound pressure field: (a) the normalized mean effective value and (b) the amplitudes of the first four harmonics. The solid curves correspond to the conjugate wave, and the dashed curve corresponds to the incident wave. The numbers 1–4 indicate the harmonic numbers;  $X$  is the distance from the beam axis. The inset shows the conjugate wave form at the point  $X = 0$ .

Figure 4 represents (a) the measured transverse distributions of the rms pressure value and (b) the corresponding distributions of the harmonic amplitudes for the conjugate beam in the focal plane of the source. The field distribution in the incident beam is shown by the dashed line. The time profile of the conjugate wave at the focus is shown on the upper right of Fig. 4a. The ratio of the fundamental harmonic amplitudes of the conjugate and incident waves at the focus was about 10, and the peak pressure drop in the conjugate wave, i.e., the difference between the positive and negative peaks of the wave profile, was 6.95 MPa. Despite the increase in the relative level of the side lobes, the field of the nonlinear conjugate wave exhibits a high quality of phase-conjugation focusing of the ultrasonic beam in both the position and the width of the principal maximum. Our experiments on the phase conjugation with amplification allow us to judge the quality of the reproduction of the acoustic field at the maximum attained pressure amplitude of the conjugate wave. One can see that it is possible to obtain an automatic phase-conjugation focusing of amplified conjugate waves with the compensation of phase aberrations due to the inhom-

ogeneities of the medium even in the presence of considerable nonlinear distortions of the waveform.

It should be noted that the experimental results presented above point to the essential difference between the properties of nonlinear wave beams with reversed fronts in acoustics and in optics. From the study of the propagation of optical beams with conjugate fronts in a homogeneous medium with a cubic nonlinearity [17], it follows that the compensation of nonlinear distortions is possible only when the transformation coefficient of the phase-conjugation mirror is close to unity, which corresponds to the general requirement that the time-reversal invariance of the equations describing the wave propagation in nonlinear and dispersive media be retained. In the case of a dispersionless propagation, which is typical of acoustics, the nonlinearity manifests itself primarily in the form of a cascade harmonic generation. In this case, the phases of all harmonics of the nonlinear wave are described by the same eikonal equation for both homogeneous and inhomogeneous media [18]. The analysis shows that such a phase correlation can lead to the compensation of phase distortions and to a spatial localization of the harmonics of the conjugate

wave in the focal region of the initial wave [15] even when, in the strict sense, the time-reversal invariance is violated. As a consequence, using the phase conjugation of the fundamental harmonic with an amplification, it is possible to obtain an efficient phase-conjugation focusing of a nonlinear wave in a dispersionless inhomogeneous medium. This specific feature of the phase conjugation of acoustic beams can find various practical applications in nonlinear systems of acoustic imaging and in the physics of intense ultrasound.

We are grateful to the staff members of the Acoustics Department of Moscow State University O.A. Sapozhnikov, Yu.A. Pishchal'nikov, and T.V. Sinilo for their assistance in calibrating the measuring hydrophone and the ultrasonic source. This work was supported by the Russian Foundation for Basic Research.

#### REFERENCES

1. B. Ya. Zel'dovich, N. F. Pilipetskiĭ, and V. V. Shkunov, *Principles of Phase Conjugation* (Nauka, Moscow, 1985; Springer, Berlin, 1985).
2. A. P. Brysev, F. V. Bunkin, D. V. Vlasov, *et al.*, *Akust. Zh.* **36**, 166 (1990) [*Sov. Phys. Acoust.* **36**, 91 (1990)].
3. A. P. Brysev, F. V. Bunkin, L. M. Krutyanskiĭ, *et al.*, *Pis'ma Zh. Ėksp. Teor. Fiz.* **61**, 454 (1995) [*JETP Lett.* **61**, 464 (1995)].
4. M. Tanter, J.-L. Tomas, and M. Fink, *Appl. Phys. Lett.* **72**, 2511 (1998).
5. H. C. Song, W. A. Kuperman, and W. S. Hodgkiss, *J. Acoust. Soc. Am.* **103**, 3234 (1998).
6. K. Yamamoto, M. Ohno, A. Kokubo, *et al.*, *J. Acoust. Soc. Am.* **106**, 1339 (1999).
7. A. P. Brysev, F. V. Bunkin, D. V. Vlasov, *et al.*, *Akust. Zh.* **34**, 986 (1988) [*Sov. Phys. Acoust.* **34**, 567 (1988)].
8. M. Ohno and K. Takagi, *Appl. Phys. Lett.* **69**, 3483 (1996).
9. M. Fink, *Phys. Today* **50**, 34 (1997).
10. A. P. Brysev, L. M. Krutyanskiĭ, and V. L. Preobrazhenskiĭ, *Usp. Fiz. Nauk* **168**, 878 (1998) [*Phys. Usp.* **41**, 793 (1998)].
11. L. M. Krutiansky, V. L. Preobrazhensky, Yu. V. Pyl'nov, *et al.*, *Phys. Lett. A* **164**, 196 (1992).
12. A. P. Brysev, F. V. Bunkin, A. D. Stakhovsky, *et al.*, *Bull. Russ. Acad. Sci., Phys., Suppl. Phys. Vib.* **59**, 40 (1995).
13. A. Brysev, L. Krutyansky, P. Pernod, and V. Preobrazhensky, *Appl. Phys. Lett.* **76**, 3133 (2000).
14. A. Brysev, L. Krutyansky, V. Preobrazhensky, *et al.*, in *Proceedings of the 15th International Symposium on Nonlinear Acoustics "Nonlinear Acoustics at the Turn of the Millennium," ISNA 15, Göttingen, 1999*, Ed. by W. Lauternborn and T. Kurtz (American Inst. of Physics, Melville, 2000), *AIP Conf. Proc.* **524**, 183 (2000).
15. P. Pernod, V. L. Preobrazhensky, and Yu. V. Pyl'nov, *Appl. Phys. Lett.* **78**, 553 (2001).
16. A. P. Brysev, F. V. Bunkin, L. M. Krutyanskiĭ, *et al.*, *Akust. Zh.* **43**, 244 (1997) [*Acoust. Phys.* **43**, 207 (1997)].
17. L. A. Bol'shov, D. V. Vlasov, M. A. Dykhne, *et al.*, *Pis'ma Zh. Ėksp. Teor. Fiz.* **31**, 311 (1980) [*JETP Lett.* **31**, 286 (1980)].
18. O. V. Rudenko and A. K. Sukhorukova, *Akust. Zh.* **37**, 753 (1991) [*Sov. Phys. Acoust.* **37**, 392 (1991)].

*Translated by E. Golyamina*

# Inverse-Bremsstrahlung Absorption of an Intense Laser Field in Cluster Plasma

I. Yu. Kostyukov

Institute of Applied Physics, Russian Academy of Sciences, ul. Ul'yanova 46, Nizhni Novgorod, 603600 Russia  
e-mail: kost@appl.sci-nnov.ru

Received February 14, 2001; in final form, March 14, 2001

Inverse-bremsstrahlung absorption of an intense laser field in cluster plasma is considered in the Born approximation with allowance made for electron interaction with the entire subsystem of clustered ions. The electromagnetic power absorbed in plasma is calculated for linearly and circularly polarized laser radiations. It is shown that plasma “clustering” can give rise to much more effective absorption of electromagnetic energy as a result of collisions. The collective effects (the action of the overall field of clustered ions on an electron) dominate over the elementary processes (electron scattering by individual ions in the cluster) in the course of inverse bremsstrahlung.

PACS numbers: 52.38.Dx; 52.27.-h; 36.40.-c

Cluster properties have long attracted the particular attention of physicists. In recent years, interest in clusters has increased due to the development of nanotechnology [1, 2] and to the effects caused by the action of intense laser radiation [3, 4]. Modern experimental technique allows the preparation of clusters from various chemical compounds over a wide range of parameters (from 100 to 1 000 000 atoms and molecules per a cluster of size 10–1000 Å). Intense laser radiation produces cluster plasma which efficiently absorbs laser energy (more than 95% of the radiant energy [5]) and is characterized by a high density and temperature of particles. High energy density renders such a medium promising for studying thermonuclear reactions [6] and generation of intense X-ray radiation [7].

It is pointed out in [7, 8] that, due to a high cluster density, the early stage of the process is characterized by a highly efficient collisional heating. Apart from the effective electromagnetic energy absorption channels such as cluster inner ionization (ionization of atoms and molecules inside the cluster) and its outer ionization (overcoming of the attractive cluster field by an electron), the inverse bremsstrahlung accompanying collisions of free (cluster-noncaptured) electrons with the ionized cluster also plays a great part. However, the available theories of inverse absorption [9, 10] do not take into account the collective effects occurring in a cluster plasma. The point is that, before cluster decay, an electron interacts not only with a single ion (as is assumed in the standard theory) but also with the entire dense cluster ion core that is formed as a result of photoionization and composed of a large number of ions. It is the purpose of this work to extend the theory of inverse bremsstrahlung to the case of cluster plasma

with inclusion of the electron interaction with the whole subsystem of clustered ions.

To study the inverse bremsstrahlung in a cluster plasma, it is convenient to employ the “jelly” cluster model [4]. This model assumes that the ion core can be represented as a sphere of radius  $a$  with a constant ion density  $n_i$  inside. Therefore, the scattering potential in the case of cluster plasma is written as

$$\varphi(r) = \begin{cases} \frac{2\pi e Z n_i}{3} (3a^2 - r^2), & r \leq a \\ \frac{4\pi e Z n_i a^3}{3r}, & r > a, \end{cases} \quad (1)$$

where  $e$  is the electron charge and  $Z$  is the ion charge. The Fourier transform of this potential is

$$U(k) = \frac{16\pi^2 e Z n_i}{k^5} [\sin(ka) - (ka) \cos(ka)]. \quad (2)$$

In the limit  $a \rightarrow 0$ , this expression transforms into the Fourier transform of a point-charge Coulomb potential  $U(k) = 4\pi q/k^2 = (4\pi/k^2)(4\pi a^3 e Z n_i/3)$ .

It follows from Eq. (1) that the electric field is maximal ( $E_{\max} \approx 4\pi e^2 Z n_i a/3$ ) at the cluster surface. For the typical ion concentration  $n_i \approx 10^{22} \text{ cm}^{-3}$  in the cluster [6, 11] and single ionization  $Z = 1$ ,  $E_{\max}$  is smaller than the atomic field ( $E_a \approx 5.1 \times 10^9 \text{ V/cm}$ ) at  $a < 85 \text{ Å}$ , which occurs when the number of particles in cluster  $N_i = 4\pi n_i a^3/3$  is less than  $2.6 \times 10^4$ . Thus, despite the large core charge, electrons can be pulled out from the cluster by a relatively weak laser field [12] and then heated as a result of inverse bremsstrahlung absorption.

The electromagnetic power absorbed due to the electron collisions with scattering centers is given by

$$Q = n_e n_{cl} \int v f(\mathbf{v}) d\mathbf{v} \sum_n n \hbar \omega \sigma_n, \quad (3)$$

where  $n_e$  is the electron concentration,  $n_{cl}$  is the concentration of scattering centers,  $f(\mathbf{v})$  is the electron distribution function,  $\omega$  is the laser frequency, and  $\hbar$  is Planck's constant. The electron scattering cross section by a potential center with absorption and emission of  $n$  photons of a circularly polarized plane electromagnetic wave can be calculated for the arbitrary scattering potential using the Born approximation [10, 13],

$$\sigma_n = \frac{e^2}{4\pi^2 \hbar v} \int d\mathbf{k} U^2(\mathbf{k}) \times J_n^2 \left( \frac{e\mathbf{E} \times \mathbf{k}}{m\hbar\omega^2} \right) \delta(\varepsilon' - \varepsilon + n\hbar\omega), \quad (4)$$

where  $\hbar\mathbf{k} = \mathbf{p}' - \mathbf{p}$ ;  $U(\mathbf{k})$  is the Fourier transform of the scattering potential;  $\varepsilon'$ ,  $\mathbf{p}'$ ,  $\varepsilon$ , and  $\mathbf{p}$  are the electron energies and momenta before and after the collision, respectively;  $E$  is the amplitude of electric laser field; and  $m$  and  $c$  are the electron mass and the velocity of light, respectively.

It is assumed that the plasma is hot enough and the electron temperature is much higher than the photon energy,  $T = m v_T^2/2 \gg \hbar\omega$ . Let us first consider the absorption in a weak laser field where the quiver velocity of an electron is much lower than its thermal velocity,  $v_{\sim} = eE/(m\omega) \ll v_T$ . In this case, the main contribution to the absorption comes from the terms with  $n = \pm 1$ , and the Bessel function in Eq. (4) can be expanded in powers of its small argument. Integration with respect to velocities with the Maxwellian electron distribution function  $f(\mathbf{v}) = v_T^{-3} \pi^{-3/2} \exp(-v^2/v_T^2)$  gives for the arbitrary scattering potential [9, 14]

$$Q = \frac{\sqrt{2\pi}}{12} \left( \frac{v_{\sim}}{v_T} \right)^3 C \times \int_0^{r_{\min}^{-1}} U^2(k) k^3 \exp\left(-\frac{\omega^2}{v_T^2 k^2}\right) dk, \quad (5)$$

$$C = \frac{8e^4 Z^2 n_e n_{cl} N_i^2}{m v_{\sim}},$$

where  $n_{cl}$  is the cluster concentration,  $r_{\min} = \max\{r_s, \lambda_e\}$ ,  $\lambda_e = \hbar/mv_T$  is the electron de Broglie wavelength, and  $r_s$  is found from equation  $T = e\phi(r_s)$ . The radius  $r_s$  bounds the spatial region  $r < r_s$  around the monotonically decreasing scattering potential, where the potential energy of a particle is greater than its kinetic energy and, hence, the theory becomes inapplicable. Since the Coulomb potential has a singularity at zero, this condi-

tion is fulfilled in a region sufficiently close to the ion. Contrary to the Coulomb potential, the cluster potential is finite, so that under certain conditions perturbation theory becomes valid everywhere. Equation (5) is obtained in the approximation  $\max\{r_s, \lambda_e\} \ll v_T/\omega$ . In the opposite limit, the particle adiabatically passes through the scattering region and the absorption becomes exponentially weak [15].

Integrating in Eq. (5) with cluster potential (1), one obtains the following expression for the power absorbed in cluster plasma in the case of a circularly polarized wave:

$$Q_{cl} = \frac{\sqrt{12\pi}}{12} C \left( \frac{v_{\sim}}{v_T} \right)^3 \left[ F\left(\frac{2\omega a}{v_T}\right) - F\left(\frac{2a}{r_{\min}}\right) \right], \quad (6)$$

$$F(y) = y^{-6} [y^6 \text{ci}(y) - 48 - 18y^2 + \cos y \times (48 - 6y^2 + y^4) + y \sin y (48 + 2y^2 - y^4)],$$

where ci stands for integral cosine. The function  $F(y) = -\ln y$  if  $y \rightarrow 0$  and  $F(y) \approx 18y^{-4}$  if  $y \rightarrow \infty$ . Then, to logarithmic accuracy, Eq. (6) can be rewritten as

$$Q_{cl} = \frac{\sqrt{2\pi}}{12} C \left( \frac{v_{\sim}}{v_T} \right)^3 \times \begin{cases} \ln\left(\frac{v_T}{\omega r_{\min}}\right), & r_{\min} \gg a \\ \ln\left(\frac{2v_T}{\omega a}\right), & v_T/\omega \gg a \gg r_{\min} \\ \frac{9}{8} \left(\frac{v_T}{\omega a}\right)^4, & a \gg v_T/\omega. \end{cases} \quad (7)$$

It follows from this expression that, if the integration region lies outside the cluster ( $r_{\min} > a$ ), then the latter can be considered as a high-charge ion. Thus, in the limit  $a \rightarrow 0$  and, correspondingly,  $n_{cl} \rightarrow n_i$  and  $n_i 4\pi a^3/3 = N_i \rightarrow 1$ , the scattering potential takes the Coulomb form and Eq. (7) converts to the standard expression for the power absorbed as a result of electron-ion collisions in an ordinary uniform plasma [9, 14]. If  $v_T/\omega \gg a$  and  $r_{\min} \ll a$ , the main contribution to the absorption comes from electrons passing outside the cluster and the cutoff at small distances actually coincides with the cluster radius. If the integration region lies inside the cluster ( $v_T/\omega < a$ ), then the absorbed power decreases markedly and the logarithmic dependence on the parameters is replaced by a power law. Notice that  $Q_{cl}$  depends on  $r_{\min}$  only if  $r_{\min} > a$ . Inasmuch as  $\lambda_e < a$  in a cluster plasma, one has  $r_{\min} = r_s = 2e^2 Z N_i / T$  in Eqs. (6) and (7). Thus, because of a large cluster size ( $\lambda_e \ll a$ ), the quantum effects in the inverse bremsstrahlung are insignificant. Note that it is sufficient to determine  $r_{\min}$  to a numerical multiplier because  $r_{\min}$  enters only the argument of a logarithm in the expression for absorbed power.

Let us now consider the inverse bremsstrahlung absorption of an intense circularly polarized electromagnetic wave ( $v_{\sim} \gg v_T$ ). In this limit, one can employ the following simplifying assumptions [10, 16]: instead of the Bessel function in Eq. (4), one can use its asymptotic form

$$J_n(z) \approx \begin{cases} \sqrt{\frac{2}{\pi z}} \cos \left[ z - \left( n + \frac{1}{2} \right) \right], & z > n \\ 0, & z < n, \end{cases} \quad (8)$$

and the summation over  $n$  can be replaced by integration with respect to  $n$ , because the number of absorbed and emitted photons in this case is large. For the intense laser field, the absorbed power shows little dependence on the electron distribution function, so that one can assume for simplicity that it has the form  $f(\mathbf{v}) = \delta(v - v_T)/4\pi v_T^2$ , where  $\delta(x)$  is the delta function. In particular, the expression for the power absorbed in a uniform plasma with such a distribution function coincides with the analogous expression obtained using the Maxwellian distribution function [9, 16]. Integrating with respect to velocities and  $n$ , one obtains for the power absorbed in a cluster plasma in the case of an intense circularly polarized wave

$$\begin{aligned} Q_{cl}^c &= \frac{\pi C}{\sqrt{2}} \int_{\omega/v_T}^{r_{\min}^{-1}} U^2(k) k^3 dk \\ &= \frac{\pi C}{\sqrt{2}} \left[ F\left(\frac{2a\omega}{v_T}\right) - F\left(\frac{2a}{r_{\min}}\right) \right]. \end{aligned} \quad (9)$$

For an intense laser field, the parameter  $r_{\min}$  is determined by the quiver velocity of an electron rather than by its thermal velocity. Since  $\hbar/mv_{\sim} < \lambda_e < a$  and  $\hbar\omega \ll T$ , the quantum effects in this case are also insignificant and  $r_{\min} = r_s = 2e^2ZN_i/mv_{\sim}^2$ . Using the asymptotic form of  $F(x)$ , Eq. (9) can be recast as

$$Q_{cl}^c = \frac{\pi C}{\sqrt{2}} \begin{cases} \ln \left( \frac{v_T m v_{\sim}^2}{e^2 Z N_i \omega} \right), & \frac{e^2 Z N_i}{m v_{\sim}^2} \gg a \\ \ln \left( \frac{2v_T}{\omega a} \right), & \frac{v_T}{\omega} \gg a \gg \frac{e^2 Z N_i}{m v_{\sim}^2} \\ \frac{9}{8} \left( \frac{v_T}{\omega a} \right)^4, & a \gg \frac{v_T}{\omega}. \end{cases} \quad (10)$$

For the Maxwellian electron distribution, the expressions for the first two limiting cases are the same, while in the third limiting case of large clusters ( $a > v_T/\omega$ ) the absorbed power increases by a factor of 15/4.

Let now consider the inverse bremsstrahlung absorption of a linearly polarized plane wave in a clus-

ter plasma. In the limit of a weak electromagnetic wave ( $v_{\sim} \ll v_T$ ), the expression for the absorbed power has the same form as for the circular polarization, Eqs. (6) and (7). For an intense linearly polarized electromagnetic wave,  $r_s$  depends on time,  $r_s = e^2ZN_i(mv_{\sim}^2 \sin^2\omega t + T)^{-1}$ , because the squared electron velocity in such a wave also depends on time. In this case, the absorbed power is calculated using the following relationship [15]:

$$Q_{cl}^l = \frac{\sqrt{2}}{\pi} C \int_0^{\pi/(2\omega)} dt \frac{\omega}{\sin\omega t} \frac{Q_{cl}^c(v_{\sim} \sin\omega t)}{C}, \quad (11)$$

where  $Q_{cl}^c(x)$  is given by Eqs. (7) and (10) as a function of oscillation velocity  $v_{\sim}$ . Depending on the value of  $v_{\sim} \sin\omega t$ , one should use different limiting expressions in Eqs. (7) and (10) at different instants of time.

The integration procedure in Eq. (11) is the same as in the case of scattering by an ion in ordinary uniform plasma [15]. Let us first consider the limit  $v_T/\omega \gg e^2ZN_i/T$  and  $a \ll e^2ZN_i/mv_{\sim}^2$ . Then, when calculating the integral in Eq. (11) for the times  $v_{\sim} \sin\omega t < v_T$ , one should use Eq. (7) for a weak laser field in the limit  $a \ll e^2ZN_i/T$ , while for the times  $v_{\sim} \sin\omega t > v_T$  one should use Eq. (9) for an intense laser field in the limit  $a \ll e^2ZN_i/(mv_{\sim}^2)$ . The result

$$Q_{cl}^l = C \ln \frac{v_{\sim}}{v_T} \ln \frac{m v_T^2 v_{\sim}}{e^2 Z N_i \omega} \quad (12)$$

coincides at  $N_i = 1$  and  $n_{cl} = n_i$  with the expression obtained for an intense linearly polarized wave absorbed due to the electron-ion collisions in a uniform plasma at  $Ze^2 \gg \hbar v_{\sim}$  and  $v_T/\omega \gg Ze^2/T$  [9, 15].

Likewise, in the general case of an intense linearly polarized electromagnetic wave absorbed in a cluster plasma with a Maxwellian electron distribution, one has at  $v_T/\omega \gg e^2ZN_i/T$

$$Q_{cl}^l = C \begin{cases} \ln \frac{v_{\sim}}{v_T} \ln \frac{m v_T^2 v_{\sim}}{e^2 Z N_i \omega}, & \frac{e^2 Z N_i}{m v_{\sim}^2} \gg a \\ \ln \frac{v_{\sim}}{v_T} \ln \frac{v_T}{a\omega} - \frac{1}{4} \ln^2 \frac{e^2 Z N_i}{Ta} \\ \frac{v_T}{\omega} \gg \frac{e^2 Z N_i}{T} \gg a \gg \frac{e^2 Z N_i}{m v_{\sim}^2} \\ \ln \frac{v_{\sim}}{v_T} \ln \frac{v_T}{a\omega}, & \frac{v_T}{\omega} \gg a \gg \frac{e^2 Z N_i}{T} \\ \frac{135}{32} \left( \frac{v_T}{\omega a} \right)^4 \ln \frac{v_{\sim}}{v_T}, & a \gg \frac{v_T}{\omega}. \end{cases} \quad (13)$$

In the opposite limit  $v_T/\omega \ll e^2ZN_i/T$ , the expressions for the absorbed power have the form

$$Q_{cl}^l = \frac{C}{4} \begin{cases} \ln^2 \frac{m v_T v_{\sim}^2}{e^2 Z N_i \omega}, & \frac{e^2 Z N_i}{m v_{\sim}^2} \gg a \\ \ln^2 \frac{v_T}{a \omega}, & \frac{v_T}{\omega} \gg a \gg \frac{e^2 Z N_i}{m v_{\sim}^2} \\ \frac{135}{16} \left( \frac{v_T}{a \omega} \right)^4 \ln \frac{m v_T v_{\sim}^2}{e^2 Z N_i \omega}, & a \gg \frac{v_T}{\omega}. \end{cases} \quad (14)$$

Let us compare the absorption efficiencies for the cluster plasma and an ordinary uniform plasma assuming that the average ion density in cluster plasma  $\langle n_i \rangle = N_i n_{cl}$  coincides with the ion density in a uniform plasma (e.g., plasma formed after cluster decay). Then, the ratio of absorbed powers in these media at  $\{a, v_T/\omega\} \gg e^2ZN_i/T$  is

$$\alpha = \frac{Q_{cl}}{Q_{pl}} \approx N_i \left( \ln \frac{m v_T v_{\sim}^2}{e^2 Z \omega} \right)^{-1} F \left( \frac{2a\omega}{v_T} \right). \quad (15)$$

In the general case, the gain in inverse bremsstrahlung in a cluster plasma, as compared to a uniform plasma, is also proportional to the number of particles in the cluster. It is worth noting that  $Q_{pl}$  also coincides with the power absorbed in a cluster plasma as a result of electron collisions with individual ions in the cluster without regard for the action of the overall ion-core field. Therefore, the parameter  $\alpha$  can be treated as the ratio of the power absorbed in cluster plasma taking into account the collective effects (i.e., taking into account the electron interaction with the entire cluster ion core) to the power absorbed without regard for these effects (i.e., only as a result of electron scattering by an individual ion in the cluster without regard for the field of the remaining ions).

It follows from Eq. (15) that the absorption efficiency in a cluster plasma increases with increasing cluster charge and can markedly exceed the absorption efficiency in the corresponding uniform plasma. In experiments [6] on thermonuclear reactions, deuterium clusters of size  $2a \approx 50 \text{ \AA}$  with density  $n_i \approx 3 \times 10^{22} \text{ cm}^{-3}$  were irradiated by a titanium-sapphire laser with an output  $I \approx 5 \times 10^{17} \text{ W/cm}^2$  and a wavelength  $\lambda \approx 7800 \text{ \AA}$ . At the electron temperature  $T \approx 1 \text{ keV}$  typical for experiments on the interaction of an intense laser radiation with clusters [3, 4], the absorption efficiency in a cluster plasma is higher than the absorption efficiency in the corresponding uniform plasma by a factor of  $\sim 4 \times 10^2$ . Thus, the energy exchange between the laser field and electrons interacting with the cluster ion core as a whole is much more efficient than in the case of their interaction with individual ions in the cluster. Despite the large logarithmic factor converting for large clusters

with  $a > v_T/\omega$  into a small multiplier  $(v_T\omega/a)^4$ , the parameter  $\alpha$  remains large enough. For example, for experiments with large clusters [11]  $2a \approx 80\text{--}100 \text{ \AA}$  ( $I \approx 10^{18} \text{ W/cm}^2$ ,  $\lambda \approx 7800 \text{ \AA}$ , and  $n_i \approx 8 \times 10^{21} \text{ cm}^{-3}$ ), the inclusion of collective effects enhances absorbed power  $\sim 3 \times 10^2$  times.

When estimating the efficiency of inverse bremsstrahlung in cluster plasma, it was assumed in this work that most electrons escape from the cluster. However, it is likely that a major part of electrons do not escape from large clusters, so that the charge distribution inside the cluster should be different from uniform and determined with regard to the inner electrons. It is notable that the question of how many electrons leave the cluster as a result of interaction is as yet little studied. The use of a Maxwellian distribution is another simplifying assumption. In real conditions, the electron velocity distribution may be anisotropic [17], and this should be taken into account when describing the heating dynamics in cluster plasma.

Evidently, the above results cease to be valid after cluster decay. Therefore, the effects studied in this work evolve during time on the order of the oscillation period of ions in the cluster (the cluster decay time approxi-

mately equals  $\tau_{cl} \approx 2\pi/\omega_i = 2\pi/\sqrt{4\pi e^2 n_i/M}$ , where  $M$  is the ion mass [6]), i.e., at the early stage of heating by prolonged laser pulses. Note that the pulse duration in many experiments is shorter than the cluster lifetime [3, 6], so that the cluster is decomposed only after the pulse. Since the characteristic time of cluster explosion is much longer than the period of the laser field, the expressions obtained in this work can be used for estimating the inverse bremsstrahlung absorption by slowly expanding clusters.

Note in conclusion that the results presented in this work are obtained in the dipole approximation. For ultrahigh-intensity laser fields, relativistic theory should be invoked [18]. However, calculations show that the inclusion of relativistic corrections in the expression for the coefficient of inverse bremsstrahlung in a usual uniform plasma brings about corrections only in the argument of a logarithm [18]. This allows one to believe that the above expressions can be used for estimating the inverse bremsstrahlung absorption of ultrahigh-intensity laser radiation in the case of cluster plasma as well.

This work was supported by the INTAS (grant no. YSF 00-46) and the Russian Foundation for Basic Research (project nos. 01-02-16575 and 99-02-16443).

## REFERENCES

1. B. M. Smirnov, Usp. Fiz. Nauk **167**, 1169 (1997) [Phys. Usp. **40**, 1117 (1997)].
2. B. M. Smirnov, Usp. Fiz. Nauk **170**, 969 (2000).
3. T. Ditmire, Contemp. Phys. **38**, 315 (1997).

4. V. P. Kraĭnov and M. B. Smirnov, Usp. Fiz. Nauk **170**, 969 (2000).
5. T. Ditmire, R. A. Smith, J. W. G. Tisch, and M. H. R. Hutchinson, Phys. Rev. Lett. **78**, 3121 (1997).
6. J. Zweiback, R. A. Smith, T. E. Cowan, *et al.*, Phys. Rev. Lett. **84**, 2634 (2000).
7. T. Ditmire, T. Donnelly, R. Falcone, and M. Perry, Phys. Rev. Lett. **75**, 3122 (1995).
8. Y. L. Shao, T. Ditmire, J. W. G. Tisch, *et al.*, Phys. Rev. Lett. **77**, 3343 (1996).
9. V. P. Silin, Zh. Éksp. Teor. Fiz. **47**, 2254 (1964) [Sov. Phys. JETP **20**, 1510 (1964)].
10. G. J. Pert, J. Phys. B **29**, 1135 (1996).
11. S. Dobosz, M. Schmidt, M. Perdrix, *et al.*, Zh. Éksp. Teor. Fiz. **115**, 2051 (1999) [JETP **88**, 1122 (1999)].
12. M. B. Smirnov and V. P. Kraĭnov, Zh. Éksp. Teor. Fiz. **115**, 2014 (1999) [JETP **88**, 1102 (1999)].
13. F. M. Bunkin and M. V. Fedorov, Zh. Éksp. Teor. Fiz. **49**, 1215 (1965) [Sov. Phys. JETP **22**, 844 (1966)].
14. Ya. Shima and H. Yatom, Phys. Rev. A **12**, 2106 (1975).
15. V. P. Silin and S. A. Uryupin, Zh. Éksp. Teor. Fiz. **81**, 910 (1981) [Sov. Phys. JETP **54**, 485 (1981)].
16. A. Ya. Polishchuk and J. Meyer-Ter-Vehn, Phys. Rev. E **49**, 663 (1994).
17. B. N. Chichkov, S. A. Shumsky, and S. A. Uryupin, Phys. Rev. A **45**, 7475 (1992).
18. I. Yu. Kostyukov and J. M. Rax, Phys. Rev. Lett. **83**, 2206 (1999).

*Translated by V. Sakun*

# Capillary Turbulence at the Surface of Liquid Hydrogen

M. Yu. Brazhnikov, G. V. Kolmakov, A. A. Levchenko, and L. P. Mezhev-Deglin

*Institute of Solid State Physics, Russian Academy of Sciences, Chernogolovka, Moscow region, 142432 Russia*

Received February 22, 2001; in final form, March 13, 2001

The results of studying the nonlinear capillary waves at a charged surface of liquid hydrogen are reported. Spectral density is experimentally determined for the surface elevations excited by spectrally narrow low-frequency pumping. It is shown that the spectral density in the range 100 Hz–5 kHz obeys the power-law dependence  $\text{const}\omega^m$  (scaling). The  $m$  exponent is close to  $-3$ , indicating that the capillary turbulence regime is established. © 2001 MAIK “Nauka/Interperiodica”.

PACS numbers: 68.03.Kn; 47.27.Gs

In this letter, we report the results of studying the oscillations of a charged surface of liquid hydrogen excited by an external force with a frequency ranging from 20 to 300 Hz. The studies were carried out in a cylindrical cell in an external dc electric field of strength lower than the critical value above which the charged flat surface of a liquid undergoes reconstruction [1].

It is known that the nonlinear interactions of capillary waves are relatively strong [2]. An ensemble of interacting waves can be described by a kinetic equation quite similar to the Boltzmann equation in gas dynamics. The dispersion law for the capillary waves  $\omega = (\sigma/\rho)^{1/2}k^{3/2}$ , where  $\sigma$  is the surface tension coefficient and  $\rho$  is the fluid density, is of the decay type. Consequently, the main contribution to the wave interaction comes from three-wave processes, namely, the process of wave decay into two waves with the conservation of total wave vector and frequency and the inverse process of confluence of two waves into a single wave.

The steady-state distribution of surface waves can be described by the Fourier transform of pair correlation function  $I_\omega = \langle |\eta_\omega|^2 \rangle$  for the surface deviations  $\eta(r, t)$  from the flat state. The theory of homogeneous capillary turbulence [3] predicts a power-law frequency dependence for the correlation function

$$I_\omega = \text{const}\omega^{-17/6}, \quad (1)$$

i.e., a Kolmogorov-type spectrum in the inertial interval. At low frequencies, the inertial interval is bounded by the drive frequency, and at high frequencies it is bounded by viscous damping. Distribution (1) is characterized by a constant energy flux to high frequencies and, hence, occurs at frequencies higher than the pump frequency (direct cascade). This prediction is confirmed by numerical simulation of the nonlinear evolution of capillary waves using “first principles,” i.e., by solving equations of hydrodynamics [4].

It is the purpose of this work to study the steady-state distribution of capillary waves at the surface of

liquid hydrogen and to compare the experimental results with the predictions of the theory of weak capillary turbulence about the formation of a power-law Kolmogorov-type spectrum. The merit of liquid hydrogen in experiments on capillary turbulence is that the kinematic viscosity of the capillary waves in this case is small, while the coefficient of nonlinearity is large, allowing the observation of the Kolmogorov-type turbulence distribution over a wide inertial frequency interval. Note that the power-law frequency dependence was recently observed for the correlation function of surface elevations at frequencies lower than 1 kHz in experiments with water [5].

The frequency spectrum of a charged surface of a fluid in a cylindrical cell was studied earlier in [6]. When comparing our experimental results with the theory developed for a continuous spectrum, account must be taken of the discrete and nonequidistant character of our spectrum.

**Experimental.** Experiments were carried out in an optical cell placed in a helium cryostat. A flat capacitor, with a radioactive target on its lower plate, was mounted horizontally inside the cell. Hydrogen was condensed into a container formed by the lower plate and a guard ring 25 mm in diameter and 3 mm in height. The liquid layer was 3 mm thick. The upper capacitor plate (collector with a diameter of 25 mm) was situated at a distance of 4 mm above the liquid surface. The liquid temperature in the experiments was 15 K.

The free fluid surface was charged by  $\beta$  electrons emitted from the radioactive target. Electrons ionized a thin liquid layer near the surface. A dc voltage  $U = 1300$  V was applied to the capacitor plates. The sign of charges forming a quasi-two-dimensional layer underneath the liquid surface was determined by the voltage polarity. In our experiments, we investigated the oscillations of a positively charged surface. The metallic guard ring installed around the radioactive target prevented escape of charged particle from the surface to the container walls.

The surface oscillations of liquid hydrogen were excited at one of the resonance frequencies (hydrogen standing waves) by an ac voltage that was applied to the guard ring additionally to the dc voltage.

It follows from our preliminary experiments with the same cell [6] that the frequency spectrum of the charged surface of liquid hydrogen is adequately described by the expression deduced in [7] taking into account the thickness of liquid layer, the distance from the surface to the upper capacitor plate, and the applied voltage  $U$ . For frequencies higher than 20 Hz, the dispersion law is close to  $\omega \sim k^{3/2}$ .

Surface oscillations of liquid hydrogen were monitored by a change in the power of a laser beam reflected from the surface. The angle between the beam and the unperturbed flat surface (glancing angle) was  $\alpha = 0.2$  rad. The linear dimensions of a light spot on the surface were  $l \approx 0.5$  mm. The beam reflected from the oscillating surface was focused by a lens onto a photodetector. The voltage at the photodetector was directly proportional to the beam power  $P(t)$  and was recorded for a few seconds on a computer interfaced to a high-speed 12-bit analog-to-digital converter.

The power of a beam reflected from the liquid surface depends on the glancing angle and the ratio of the surface wavelength  $\lambda$  to the spot size  $l$ . In our experiments, the oscillating surface deviated from the flat state by an angle  $\delta\varphi \leq 10^{-2}$  rad that was much smaller than the angle  $\alpha$ . For small-amplitude waves with wavelengths much larger than the spot size,  $\lambda \gg l$ , the power of the reflected beam is a linear function of angle  $\delta\varphi$  [8]. In the opposite case,  $\lambda < l$ , the spot size accommodates several wavelengths and the recorded power of the reflected beam is determined by the surface slope averaged over the light spot area. Estimates show that the power of the reflected beam generally changes by a value that is proportional to the product of the amplitude of angle  $\delta\varphi$  and the wavelength  $\lambda$ . The crossover from one recording regime to another occurs at a frequency  $\omega_l/2\pi \approx 500$  Hz corresponding to the surface wave with  $\lambda \approx l$  in liquid hydrogen.

**Results and discussion.** The oscillations of the charged surface of liquid hydrogen were excited at frequencies from 20 to 300 Hz. The spectral density of beam power reflected from the charged surface of liquid hydrogen was obtained by taking Fourier transform of the measured  $P(t)$  dependence. Typical results are presented in Figs. 1 and 2.

The frequency dependence of the squared amplitude of Fourier transform  $P_\omega^2$  of the measured signal is shown in Fig. 1. The surface was excited at a frequency of the third resonance of surface waves in the cell,  $\omega_p/2\pi = 28$  Hz. The main peak at a drive frequency  $\omega_p$  and the peaks at multiple frequencies are observed in the  $P_\omega^2$  vs.  $\omega/2\pi$  curve. These peaks correspond to the capillary waves excited at the surface as a result of non-

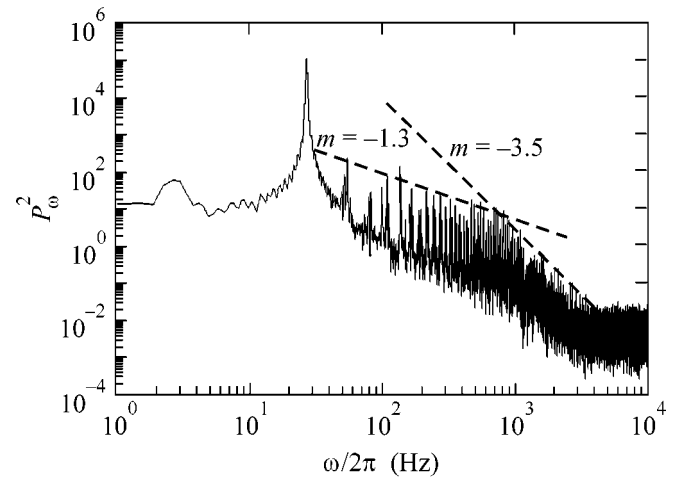


**Fig. 1.** Frequency dependence of the squared Fourier transform of the laser beam power reflected from the oscillating charged surface. Pump frequency  $\omega_p/2\pi = 28$  Hz and  $U = 1300$  V. The dashed lines correspond to the  $\omega^m$  dependences with  $m = -1.3$  and  $-3.5$ .

linearity. The frequency dependence of a peak at frequencies below 800 Hz fits a power law  $\omega^m$  with exponent  $m \approx -1.3$ . At high frequencies  $\omega/2\pi > 800$  Hz, the frequency dependence of peak heights is described by a steeper function with exponent  $m \approx -3.5$ . At frequencies above 4 kHz, the peaks disappear in the instrumental noise. A change in the exponent  $m$  at a frequency near 800 Hz is likely caused by the crossover from the regime of recording long-wavelength oscillations with  $\omega < \omega_l$  to the regime of recording short-wavelength oscillations ( $\omega > \omega_l$ ). The observed crossover frequency  $\omega_l/2\pi = 800$  Hz is close to the above-mentioned value obtained from qualitative considerations.

The frequency dependence of  $P_\omega^2$  obtained in the experiment with pump frequency  $\omega_p/2\pi = 263$  Hz (16th resonance) is shown in Fig. 2. It clearly demonstrates that the peak height decreases at  $\omega > \omega_p$  following the law close to  $P_\omega^2 \sim \omega^{-3.5}$  up to a frequency of 5 kHz. The spectrum suffered a substantial change with increasing pump frequency: the low-frequency interval where  $P_\omega^2$  is proportional to  $\omega^{-1.3}$  disappeared.

In our experiments, we measured the reflected beam power, which at  $\omega < \omega_l$  is proportional to the angle  $\delta\varphi$  of surface deviation from the equilibrium position. This angle can be estimated as a ratio of the wave amplitude to the wavelength. Then the correlation function of surface elevations is written in the frequency representation as

$$I_\omega = \langle |\eta_\omega|^2 \rangle \sim (\omega^{-2/3} \delta\varphi_\omega)^2 \sim P_\omega^2 \omega^{-4/3}. \quad (2)$$

At  $\omega > \omega_l$ , the power  $P_\omega \sim \lambda \delta\varphi_\omega$  or

$$I_\omega \sim P_\omega^2. \quad (3)$$

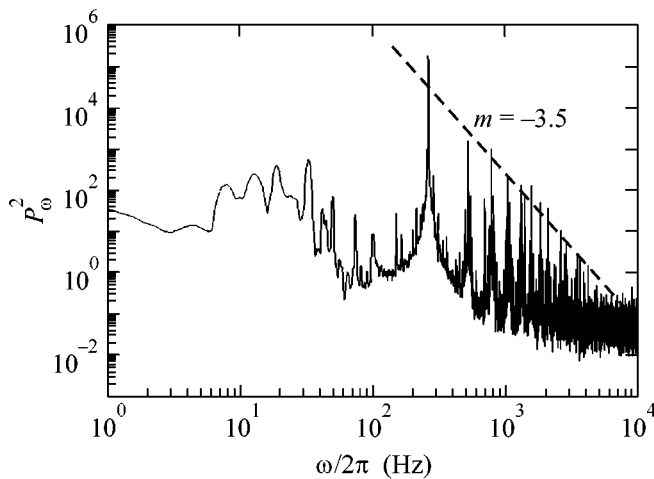


**Fig. 2.** Spectral distribution of  $P_\omega^2$  for pumping at  $\omega_p/2\pi = 263$  Hz with  $U = 1300$  V. The dashed line corresponds to the  $P_\omega^2 \sim \omega^{-3.5}$  dependence.

It follows from the  $P_\omega^2$  dependences shown in Figs. 1 and 2 that the correlation function in the frequency range 200–800 Hz, as estimated using Eq. (2), is close to  $I_\omega \sim \omega^{-2.6}$ . At frequencies higher than 800 Hz, the estimate by Eq. (3) gives  $I_\omega \sim \omega^{-3.5}$ . Thus, experimental data demonstrate the power-law (scaling) frequency dependence for the correlation function of surface elevations (scaling) in the frequency range 100–5000 Hz. This is consistent with the results of work [5]. The fact that the measured exponents are close to theoretical estimate (1) provides evidence for the occurrence of a weak-turbulence regime in the system of capillary waves. The deviation of the exponent  $m$  from its theoretical value at low frequencies may be due to the discreteness of the frequency spectrum of a liquid surface oscillations in a finite-size cell. Moreover, the excitation conditions in our experiments differed from those in the theoretical model; in the experiment, the pumping was accomplished at a fixed frequency, whereas

theoretical Eq. (1) implies a broadband pumping with simultaneous excitation of many surface eigenmodes.

In summary, a power-law (scaling) frequency dependence was observed experimentally for the correlation function of surface elevations (scaling) in liquid hydrogen in the frequency range 100–5000 Hz. The frequency dependence obtained for the correlation function as a result of processing experimental data is in qualitative agreement with the predictions of the theory of weak capillary turbulence.

We are grateful to V.E. Zakharov and E.A. Kuznetsov for helpful discussion; to E. Henry, P. Al'strom, and M. Levinsen for providing the manuscript of paper [5] before publication; and to V.N. Khlopinskiĭ for assistance in experiments. This work was supported (in part) by the Ministry of Industry, Science, and Technology of the Russian Federation (project "Kristall-6") and by the INTAS-NETWORK (grant no. 97-1643).

## REFERENCES

1. A. A. Levchenko, G. V. Kolmakov, L. P. Mezhev-Deglin, *et al.*, *Pis'ma Zh. Eksp. Teor. Fiz.* **65**, 547 (1997) [*JETP Lett.* **65**, 572 (1997)].
2. V. Zakharov, V. L'vov, and G. Fal'kovich, *Kolmogorov Spectra of Turbulence*, Vol. 1: *Wave Turbulence* (Springer-Verlag, Berlin, 1992).
3. V. E. Zakharov and N. N. Filonenko, *Zh. Prikl. Mekh. Tekh. Fiz.* **5**, 62 (1967).
4. A. N. Pushkarev and V. E. Zakharov, *Phys. Rev. Lett.* **76**, 3320 (1996).
5. E. Henry, P. Alstrom, and M. T. Levinsen, *Europhys. Lett.* **52**, 27 (2000).
6. A. A. Levchenko, G. V. Kolmakov, L. P. Mezhev-Deglin, *et al.*, *J. Low Temp. Phys.* **119**, 343 (2000).
7. D. M. Chernikova, *Fiz. Nizk. Temp.* **2**, 1374 (1976) [*Sov. J. Low Temp. Phys.* **2**, 669 (1976)].
8. L. D. Landau and E. M. Lifshitz, *Course of Theoretical Physics*, Vol. 8: *Electrodynamics of Continuous Media* (Nauka, Moscow, 1982; Pergamon, New York, 1984), p. 405.

*Translated by V. Sakun*

# A Sequence of Two Ferrotoroidal Phase Transitions in Nickel–Bromine Boracite $\text{Ni}_3\text{B}_7\text{O}_{13}\text{Br}$

D. G. Sannikov

Shubnikov Institute of Crystallography, Russian Academy of Sciences, Leninskii pr. 59, Moscow, 117333 Russia

Received December 15, 2000; in final form, March 12, 2001

The phenomenological theory of a sequence of two second-order phase transitions in Ni–Br boracite is presented. Two different components of the toroidal moment vector  $T_i$  are the order parameters of these transitions. Expressions are derived for the temperature dependences of the spontaneous values of  $T_i$ , polarization  $P_i$ , and magnetization  $M_i$  and the dielectric  $\chi_{ij} = dP_i/dE_j$ , magnetic  $k_{ij} = dM_i/H_j$ , and magnetoelectric  $\alpha_{ij} = dP_i/dH_j = dM_j/dE_i$  susceptibilities. Some of these susceptibilities display sharp temperature peaks in the vicinity of phase transitions. © 2001 MAIK “Nauka/Interperiodica”.

PACS numbers: 77.80.Bh; 75.30.Cr; 75.30.Kz

It has been realized rather unexpectedly that, along with the well-known dipole moments such as polarization  $P_i$  and magnetization  $M_i$ , there is one more dipole moment in electrodynamics, namely, a toroidal moment  $T_i$ , that was discovered not too long ago (see review [1]). The transformation properties of the vector  $T_i$  are different from those of the  $P_i$  and  $M_i$  vectors; it changes sign both under spatial and under time inversions. In [2], phase transitions with the order parameter  $T_i$  were assigned to a separate class of transitions (see also [3]). A phenomenological approach to the description of the phase transition in Ni–I boracite ( $T = 64$  K) was suggested in [4], where this transition was treated as a ferrotoroidal (or toroidal; there is no unique terminology as yet) transition. Although all available experimental data were explained, it was still unclear whether the same data could be explained in any other way (especially if the translational symmetry of crystal changed upon the transition). In more recent experiments on low-temperature phase transitions in Co–Br, Co–I, and Ni–Cl boracites [5–7], a narrow temperature peak due to the  $\alpha_{32}$  component of magnetoelectric tensor  $\alpha_{ij}$  was observed near the transition (no such peak was observed for the  $\alpha_{23}$  component). These data were explained on the assumption that the transition was a ferrotoroidal phase transition, for which the  $T_1$  component of the  $T_i$  vector plays the part of order parameter [8] (see also [9, 10]). As a result, no doubt remained that boracites provide the first examples of ferrotoroidal crystals (or toroids) exhibiting the ferrotoroidal phase transition.

In recent work [11], two sequential low-temperature second-order phase transitions were observed in Ni–Br boracite at  $T = 30$  K and  $T = 21$  K. The proximity of these two transitions suggests that they are caused by a

common mechanism. In other words, they can be described by a single thermodynamic potential, in which only the coefficient  $A$  of  $T_i^2$  changes with temperature  $T$  and passes through zero upon lowering  $T$ . Therefore, both transitions are proper ferrotoroidal transitions, the first one being related to the  $T_1$  component and the second to the  $T_2$  component of the  $T_i$  vector. It is of interest to find out what characteristic temperature anomalies can be observed for the  $P_i$ ,  $M_i$ , and  $T_i$  vectors and the  $\chi_{ij}$ ,  $k_{ij}$ , and  $\alpha_{ij}$  tensors in the vicinity of these transitions. It is also of interest to reveal whether there are other possible sequences of ferrotoroidal phase transitions in boracites, and, if so, under what conditions they can occur. This issues are the subject of this work.

Let us denote the sequence of phase transitions observed in the Ni–Br boracite as  $G_0 \rightarrow G_1 \rightarrow G_2 \rightarrow G_3$ . The phase transition  $G_0 \rightarrow G_1$  at  $T = 398$  K is an improper ferroelectric transition. The symmetry of the cubic phase  $G_0$  is  $T_d' = \bar{4}3m1'$ , and the symmetry of the orthorhombic phase  $G_1$  is  $G_{2v}' = mm21'$ . We are interested in the transition sequence  $G_1 \rightarrow G_2 \rightarrow G_3$ . The symmetry of another orthorhombic phase  $G_2$  is  $C_{2v}(C_s) = m'm2'$ . For the symmetry of the  $G_3$  phase, see below. It is assumed that the  $T_1$  component is the order parameter of the first phase transition  $G_1 \rightarrow G_2$  at  $T = \theta_1$  (as in other boracites showing only a single such transition) and the  $T_2$  component is the order parameter of the second  $G_2 \rightarrow G_3$  transition at  $T = \theta_2$ . Let us focus on the thermodynamic potential for the cubic phase of a crystal. Our goal is to estimate the spontaneous  $T_i$ ,  $P_i$ , and  $M_i$  vectors and  $\chi_{ij}$ ,  $k_{ij}$ , and  $\alpha_{ij}$  susceptibilities using the coefficients in the respective expressions.

The following invariants (structural and exchange) are used in writing the potential for the  $G_0$  phase:

$$R^2, P^2, P_3 R^2, M^2, T^2, P_i E_i, M_i H_i, \quad (1)$$

where  $R^2$  stands for the square of the six-component order parameter of the  $G_0 \rightarrow G_1$  phase transition. It is assumed that the transition results in the nonzero spontaneous component  $P_3$  and that  $P_3 > 0$  (single-domain crystal). The relativistic invariants

$$I_1 = \frac{1}{4}(T_1^2 - T_2^2)^2 + (T_1^2 + T_2^2)T_3^2,$$

$$I_2 = (P_1 T_1 - P_2 T_2)T_3 + \frac{1}{2}P_3(T_1^2 - T_2^2), \quad (2)$$

$$I_3 = (P_2 M_3 - P_3 M_2)T_1 + (P_3 M_1 - P_1 M_3)T_2 + (P_1 M_2 - P_2 M_1)T_3,$$

$$I_4 = (M_2 T_1 - M_1 T_2)(T_1^2 - T_2^2) - 2(M_2 T_1 + M_1 T_2)T_3^2 + 4M_3 T_1 T_2 T_3$$

are also used. In what follows, the experimentally suitable orthorhombic coordinates  $x_1, x_2, x_3$  turned relative to the cubic coordinates  $x, y, z$  through  $\pi/4$  about the  $z = x_3$  axis are used.

The thermodynamic potential has the form

$$\begin{aligned} \Phi = & \alpha R^2 + \frac{1}{2}\beta R^4 + \frac{1}{2}AT^2 + \frac{1}{4}CT^4 \\ & - \bar{D}R^2 T^2 + \frac{1}{2}\kappa P^2 - \sigma P_3 R^2 + \frac{1}{2}BM^2 + cI_1 \\ & - dI_2 + aI_3 - bI_4 - P_i E_i - M_i H_i. \end{aligned} \quad (3)$$

(As to the choice of the invariants in Eqs. (1) and (2) and the potential in Eq. (3), see in more detail [8].) Eliminating  $R^2$ , one arrives at the thermodynamic potential that contains only the desired vector components of  $P_i, M_i$ , and  $T_i$ :

$$\begin{aligned} \Phi = & \Phi_0 + \frac{1}{2}\bar{A}T^2 + \frac{1}{4}\bar{C}T^4 + \frac{1}{2}\kappa(P_1^2 + P_2^2) \\ & + \frac{1}{2}\tilde{\kappa}P_3^2 - \tilde{\kappa}DP_3 T^2 + \frac{1}{2}BM^2 \\ & + cI_1 - dI_2 + aI_3 - bI_4 - P_i E_i - M_i H_i. \end{aligned} \quad (4)$$

The following notation is used hereafter:

$$\begin{aligned} \tilde{\kappa} = & \kappa - \frac{\sigma^2}{\beta}, \quad D = \frac{\sigma\bar{D}}{\beta\tilde{\kappa}}, \quad \bar{A} = A - 2\frac{\tilde{\kappa}D}{\sigma}P_0, \\ \bar{C} = & C - 2\frac{D^2}{\beta}, \quad \tilde{A} = \bar{A} - 2\tilde{\kappa}DP_0 - dP_0, \\ \tilde{C} = & \bar{C} - 2\tilde{\kappa}D^2 + c - 2Dd, \\ c' = & c - Dd, \quad c'' = c + dD, \end{aligned} \quad (5)$$

where the spontaneous polarization  $P_0 = P_0(T)$  in the  $G_1$  phase should be taken from the experiment. Note that

the use of  $P_0(T)$  allowed the unknown and temperature-dependent coefficient  $\alpha$  to be eliminated from Eq. (3). It follows from Eqs. (3) and (4) for the potentials that  $\beta > 0$ ,  $\tilde{\kappa} > 0$ ,  $\bar{C} > 0$ , and  $B > 0$ , while the signs of coefficients  $D, a, b, c$ , and  $d$  are arbitrary.

By varying the potential in Eq. (4) with respect to the  $T_i, P_i$ , and  $M_i$  variables and solving the resulting equations, one obtains the following expressions for the spontaneous values of these quantities in the  $G_1, G_2$ , and  $G_3$  phases. Below, only the nonzero components and only the leading terms of power series expansions in parameters  $T_i^2, a, b, c, d$ , and  $P_0$  are presented. In the  $G_1$  phase,

$$P_3 = P_0. \quad (6)$$

In the  $G_2$  phase,

$$\begin{aligned} T_1^2 = & -\frac{\tilde{A}}{\bar{C}} = \frac{A_T}{\bar{C}}(\theta_1 - T), \\ P_3 = & P_0 + DT_1^2, \\ M_2 = & \frac{aP_0}{B}T_1. \end{aligned} \quad (7)$$

It is assumed that only the coefficient  $\tilde{A}$  linearly depends on  $T$ :  $\tilde{A} = A_T(T - \theta_1)$ . The quantity  $P_0$  also depends on  $T$  (see above). For the  $G_1 \rightarrow G_2$  phase transition to be ferrotoroidal with respect to the  $T_1$  component, it is necessary that the inequality  $d > 0$  be fulfilled. In the  $G_3$  phase,

$$\begin{aligned} T_1^2 = & \frac{1}{c'}(dP_0 + c''T_2^2), \quad T_2^2 = \frac{c'}{2c}\frac{A_T}{\bar{C}}(\theta_2 - T), \\ \theta_1 - \theta_2 = & \frac{\tilde{C}}{A_T c'}dP_0, \quad P_3 = \frac{c}{c'}(P_0 + 2DT_2^2), \end{aligned} \quad (8)$$

$$M_1 = -\frac{ac + bd}{Bc'}T_2(P_0 + 2DT_2^2),$$

$$M_2 = \frac{ac + bd}{Bc'}T_1(P_0 + 2DT_2^2).$$

An analysis of the potential in Eq. (4) shows that the  $G_2 \rightarrow G_3$  phase transition is ferrotoroidal with respect to the  $T_2$  component only if the inequalities  $c > 0$  and  $c - Dd > 0$  are fulfilled.

By twice varying the potential in Eq. (4), first with respect to  $T_i, P_i$ , and  $M_i$  and next with respect to  $E_i$  and  $H_i$ , and solving the resulting equations, one arrives after tedious mathematics at the following expressions for the  $\chi_{ij}, k_{ij}$ , and  $\alpha_{ij}$  susceptibilities [under the same conditions as in deriving Eqs. (6)–(8)]. In the  $G_1$  phase,

$$\chi_{33} = \frac{1}{\tilde{\kappa}}, \quad k_{22} = \frac{1}{B} + \frac{a^2 P_0^2}{B^2 A_T (T - \theta_1)}. \quad (9)$$

In the  $G_2$  phase,

$$\begin{aligned}\chi_{33} &= \frac{1}{\tilde{\kappa}} + \frac{2D^2}{\tilde{C}}, & k_{11} &= \frac{1}{B} + \frac{(ac + bd)^2 P_0 \theta_1 - \theta_2}{2B^2 c'^2 d T - \theta_2}, \\ k_{22} &= \frac{1}{B} + \frac{a^2 P_0^2}{2B^2 A_T (\theta_1 - T)}, & \alpha_{23} &= -\frac{a}{\kappa B} T_1, & \alpha_{32} &= \frac{DaP_0}{BC} \frac{1}{T_1}.\end{aligned}\quad (10)$$

And in the  $G_3$  phase,

$$\begin{aligned}\chi_{33} &= \frac{1}{\tilde{\kappa}} + \frac{2D^2}{\tilde{C}}, & \chi_{12} &= \chi_{21} = -\frac{d^2}{2\kappa^2 c} \frac{T_2}{T_1}, \\ k_{11} &= \frac{1}{B} + \frac{(ac + bd)^2 P_0 \theta_1 - \theta_2}{4B^2 c'^2 d \theta_2 - T}, \\ k_{12} &= k_{21} = \frac{(ac + bd)(ac + 5bd) T_1}{8B^2 c c' d T_2}, \\ \alpha_{13} &= \frac{ac + 2bd}{\kappa B c} T_2, \\ \alpha_{31} &= \frac{(ac + bd) P_0}{2Bc} \left( \frac{d}{2\kappa c'} - \frac{D}{\tilde{C}} \right) \frac{1}{T_2}, \\ \alpha_{23} &= -\frac{a}{\kappa B} T_1, \\ \alpha_{32} &= \frac{ac + bd}{2Bcd} \left[ \frac{5d}{2\tilde{\kappa}} + D(c + 5Dd) \frac{1}{\tilde{C}} \right] T_1.\end{aligned}\quad (11)$$

In Eqs. (10) and (11),  $T_1^2$  and  $T_2^2$  in the denominators are replaced by their  $T$ -dependent expressions given by Eqs. (7) and (8). The quantities  $\chi_{ij}$  and  $k_{ij}$  that are not given in Eqs. (9)–(11) are equal to  $\chi_{ij} = 1/\kappa$  and  $k_{ij} = 1/B$ , as in the initial  $G_0$  phase.

It follows from Eqs. (6)–(11) that the phase transitions  $G_1 \rightarrow G_2$  and  $G_2 \rightarrow G_3$ , being presumably proper ferrotoroidal with respect to  $T_1$  and  $T_2$ , prove to be improper ferroelectric transitions with respect to  $P_3$  and weak ferromagnetic ones with respect to  $M_2$  and  $M_1$ . In the vicinity of the first  $G_1 \rightarrow G_2$  transition, the  $k_{22}$  and  $\alpha_{32}$  components show anomalous temperature behavior in the form of narrow peaks [cf. Eqs. (9) and (10)], with the  $k_{22}$  component being anomalous in both the  $G_1$  and the  $G_2$  phase while  $\alpha_{32}$  only in the  $G_2$  phase. The  $k_{11}$ ,  $k_{12}$ , and  $\alpha_{31}$  components are responsible for the narrow peaks near the second transition  $G_2 \rightarrow G_3$  [cf. Eqs. (10) and (11)], with  $k_{11}$  being anomalous in both phases  $G_2$  and  $G_3$  while  $k_{12}$  and  $\alpha_{31}$  only in the  $G_3$  phase. The observation of this anomalous behavior in the experiments would serve as a test for the validity of the theoretical approach suggested in this work. According to this approach, the magnetic point symmetry group of the  $G_3$  phase should be  $C_2(C_1) = 2'$ .

If one assumes that not  $T_2$  but the  $T_3$  component is the order parameter of the second transition  $G_2 \rightarrow G_3$ ,

then this transition can occur only if the inequalities  $c + Dd < 0$  and  $c - 2Dd < 0$  hold. In this case, the magnetic point symmetry group of the  $G_3$  phase should be  $C_s = m$ . This variant of the theory is less appropriate to the experimental data [11] than the one suggested above, and so it is not considered here. Note that the magnetic point group of the  $G_3$  phase was experimentally specified as  $C_1 = 1$  [11]. However, the second-order phase transition from the  $C_{2v}(C_s) = m'm2'$  group to the  $C_1 = 1$  group, strictly speaking, is forbidden. This point also calls for further experimental verification.

An analysis of potential (4) suggests that other sequences of ferrotoroidal phase transitions are also possible in boracites. If the inequalities  $c < 0$  and  $c - 2Dd > 0$  are fulfilled, then the sequence  $G_1 \rightarrow G_2 \rightarrow G_3 \rightarrow G_4$  becomes possible, where the magnetic point symmetry group of the  $G_3$  phase is  $C_s = m$  and that of the  $G_4$  phase is  $C_1 = 1$ . This case was not considered in this work because there is no experimental need for it: a sequence of three low-temperature phase transitions was observed in none of the boracites. Finally, if  $c - Dd < 0$  and  $c + Dd > 0$ , then only a single  $G_1 \rightarrow G_2$  transition is possible. This case was considered in [8] and, in fact, is reproduced in this work [cf. Eqs. (6), (7), (9), and (10)].

I am grateful to V.A. Golovko for useful remarks.

## REFERENCES

1. V. M. Dubovik and L. A. Tosunyan, *Fiz. Élem. Chastits At. Yadra* **14**, 1193 (1983) [*Sov. J. Part. Nucl.* **14**, 504 (1983)].
2. V. L. Ginzburg, A. A. Gorbatsevich, Yu. V. Kopaev, and B. A. Volkov, *Solid State Commun.* **50**, 339 (1984).
3. B. A. Volkov, A. A. Gorbatsevich, Yu. V. Kopaev, and V. V. Tugushev, *Zh. Éksp. Teor. Fiz.* **85**, 729 (1981) [*Sov. Phys. JETP* **54**, 391 (1981)].
4. D. G. Sannikov and I. S. Zheludev, *Fiz. Tverd. Tela (Leningrad)* **27**, 1369 (1985) [*Sov. Phys. Solid State* **27**, 826 (1985)].
5. M. Clin, J.-P. Rivera, and H. Schmid, *Ferroelectrics* **79**, 173 (1988).
6. M. Clin, J.-P. Rivera, and H. Schmid, *Ferroelectrics* **108**, 213 (1990).
7. J.-P. Rivera and H. Schmid, *J. Appl. Phys.* **70**, 6410 (1991).
8. D. G. Sannikov, *Zh. Éksp. Teor. Fiz.* **111**, 53 (1997) [*JETP* **84**, 293 (1997)].
9. I. E. Chupis, *Fiz. Nizk. Temp.* **18**, 306 (1992) [*Sov. J. Low Temp. Phys.* **18**, 210 (1992)].
10. D. G. Sannikov, *Ferroelectrics* **219**, 177 (1998).
11. S.-Yu. Mao, H. Schmid, G. Triscone, and J. Muller, *J. Magn. Magn. Mater.* **195**, 65 (1999).

Translated by V. Sakun

# Anomalous Phonon Wind Effect on the Lateral Exciton Migration in Ultrathin Quantum Well CdTe/ZnTe

E. E. Onishchenko\*, V. S. Bagaev, and V. V. Zaitsev

Lebedev Physical Institute, Russian Academy of Sciences, Leninskiĭ pr. 53, Moscow, 117924 Russia

\* e-mail: evgeny@lebedev.ru

Received December 27, 2000; in final form, February 27, 2001

The effect of nonequilibrium acoustic phonon flux on the photoluminescence of an ultrathin quantum well CdTe/ZnTe upon its quasi-resonant excitation by a He–Ne laser was studied. It is found that the phonon flux generated by an external source affects the quantum well luminescence bandshape even at small lasing power and large (up to 1 cm) distance between the phonon generation zone and the quasi-resonant luminescence excitation zone. It is assumed that the phonon flux stimulates exciton in-plane (lateral) migration in the quantum well through the tunneling between the local potential minima accompanied by *induced* phonon emission.  
© 2001 MAIK “Nauka/Interperiodica”.

PACS numbers: 78.67.De; 63.22.+m

**Introduction.** It is known that when interpreting luminescence spectra of real quantum wells (QWs) with intrinsic thickness fluctuations, it is necessary to take into account the transfer of localized excitons between the spatially separated states with different energies. As a rule, such a lateral transfer is assisted by acoustic phonons [1]. Inasmuch as the situation in real heterostructures is generally nonequilibrium, it is of interest to study the influence of nonequilibrium acoustic phonons on the ensemble of localized excitons.

The influence of a nonequilibrium phonon flux (phonon wind [2]) on the QW photoluminescence in III-V and II-VI semiconductors was investigated in a number of works [3–5]. In these works, phonons were excited using a heat pulse technique which is widely employed for studying the phonon propagation and electron–phonon interaction in semiconductors. Contrary to the classical heat pulse technique, in which a heated metallic film serves as a phonon source, nonequilibrium phonons in our experiments were generated directly by the optical excitation of the structure. In this case, phonons are generated in the course of thermalization and nonradiative recombination of optically excited nonequilibrium charge carriers. Compared to the heat pulse technique, the spectrum of the phonons generated in this way is more nonequilibrium [6].

In the experiment described below, the influence of a phonon wind on the luminescence of an ultrathin CdTe/ZnTe QW was studied (the nominal thickness of the CdTe layer composed of four monolayers was  $\approx 1.3$  nm). The QW luminescence was excited in a quasi-resonant regime by a He–Ne laser because

(1) this allowed the number of nonequilibrium phonons generated in the course of excitation of the QW exciton states to be minimized;

(2) it was shown by us in [7] that the short-wavelength wing of the QW luminescence band excited in this way displays two additional (compared to the non-resonant excitation) features whose dynamics upon temperature increase or under the action of phonon wind allows qualitative conclusions to be drawn about the influence of acoustic phonons on the lateral exciton migration;

(3) the contribution from the luminescence of the isovalence  $O_{Te}$  impurity is absent in the luminescence spectrum (at low nonresonant excitation levels, this band would superpose on the QW luminescence band, thus impeding the interpretation of the experimental results).

**Experimental.** A CdTe/ZnTe structure was grown on a semi-insulating GaAs(001) substrate by molecular beam epitaxy [7]. The scheme of the experiment is shown in Fig. 1. The excitonic luminescence was excited by a He–Ne laser beam ( $\lambda = 632.8$  nm) focused

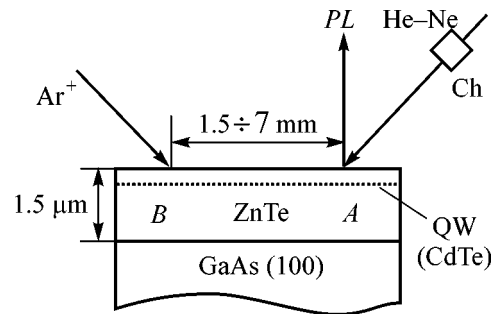


**Fig. 1.** Scheme of the experiment. Quasi-resonant photoluminescence (PL) excitation was provided by a He–Ne laser in zone A, and the nonequilibrium phonons were generated in zone B by the beam of an argon laser. The radiation of a He–Ne laser was modulated by chopper Ch.

into a spot with diameter  $\sim 0.1$  mm at a laser output of 1 mW (zone A). The laser radiation was modulated with a frequency of 1 kHz by mechanical chopper *Ch*. At a distance of several millimeters (from 1.5 to 7 mm in our experiments) from zone A, phonons were generated in zone B by an argon laser beam ( $\lambda = 488$  nm). For a beam diameter of  $\sim 0.1$  mm, the excitation power was varied within 0.4–150 mW. The luminescence spectra were analyzed by a DFS-24 double grating monochromator (with a reciprocal linear dispersion of 0.5 nm/mm). The signal was recorded using the lock-in detection technique. Measurements were performed at temperatures of 4.2 and 1.8 K.

**Description of the structure.** The band diagram of the CdTe/ZnTe structure is depicted in Fig. 2. The contribution of the conduction band (CB) to the potential jump is the greatest, resulting in a deep potential well for electrons. The valence band (VB) accounts for no greater than 20% of the difference in the energy gaps of ZnTe and CdTe ( $\approx 0.8$  eV). The electron (and exciton) energy level is shifted approximately by 100 meV upon changing the QW thickness by one monolayer (in the range of 1–5 monolayers).

High-resolution transmission electron microscopy suggests that the ultrathin QW is a CdTe layer of variable local thickness. The layer geometry is schematically depicted in the inset in Fig. 2. The characteristic lateral irregularity scale (islands of a monolayer thickness) is  $d_i < a_B$ , where  $a_B$  is the exciton Bohr radius. The irregularity of heteroboundaries produces a fluctuation potential. As was mentioned above, a change in the average QW thickness by one monolayer brings about a sizable (approximately by 100 meV) change in the depth of the exciton energy level. This defines the characteristic scale (tens of millielectronvolts) of fluctuations in the energy spectrum. Accordingly, the degree of localization at low temperatures is different for all excitons in QW; i.e., excitons cannot freely move in the QW plane but can migrate executing tunneling transitions between the local potential minima. These transitions are accompanied by the emission (absorption) of acoustic phonons. At low temperatures, the migration mainly proceeds with energy loss. As a rule, the higher energy states are less localized (for these states, the time of exciton departure to the other state is shorter than the recombination time).

As expected, the QW luminescence bandwidth at low temperatures is due to the inhomogeneous broadening and measures  $\sim 25$  meV. Figure 3 shows the QW luminescence spectrum upon quasi-resonant excitation by a He–Ne laser (solid line). The features indicated by vertical dash-dot lines emerge because both interface ( $\hbar\omega_1 = 19$  meV) and confined ( $\hbar\omega_2 = 25$  meV) optical phonons, appearing due to the CdTe layer, are involved in the relaxation of excitons produced by the He–Ne laser photons [8].

**Results.** The influence of phonon wind on the luminescence of the ultrathin QW is demonstrated in Fig. 3.

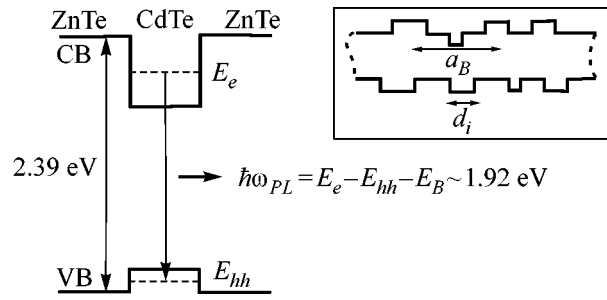


**Fig. 2.** Energy band diagram for the CdTe/ZnTe structure. Subscripts: *e* electron, *hh* heavy hole, and  $E_B$  exciton binding energy. The QW cross section perpendicular to the layer plane is schematically shown in the inset.

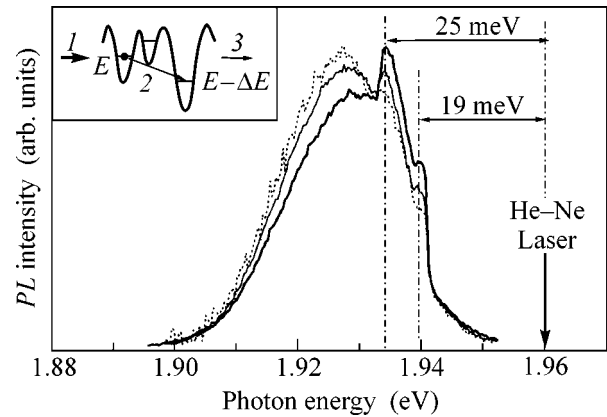


**Fig. 3.** The bold solid line is the QW luminescence spectrum for the quasi-resonant excitation by a He–Ne laser in the absence of nonequilibrium phonon flux. The solid line is the QW luminescence spectrum for an argon laser output of 1 mW. The points are the QW luminescence spectrum for an argon laser output of 150 mW. In both cases, the spacing between zones A and B is 7 mm. The potential relief is schematically shown in the inset. The horizontal lines indicate the exciton energy levels in the local potential wells. The nonequilibrium phonon flux (1) with energy  $\hbar\omega \sim \Delta E$  stimulates the exciton down-energy transition (2) accompanied by the induced emission of a phonon with  $\hbar\omega = \Delta E$  (3).

The features caused by the exciton relaxation mediated by the confined and interface phonons markedly weaken, and the integrated photoluminescence intensity increases by 5–15%. The phonon wind effect is observed even at an argon laser output of 0.4 mW (!) and for a distance of 7 mm between zones A and B. At a pump power of  $>10$  mW, the magnitude of the effect (change in the luminescence integrated intensity and bandshape) ceases to depend on the distance between zones A and B.

**Discussion.** The phonon wind enhances the QW luminescence integrated intensity and the population of low-energy exciton states, because a part of the excitons relax from the higher energy states. Note that the rise in temperature brings about an opposite transformation (Fig. 4). The integrated intensity is reduced,

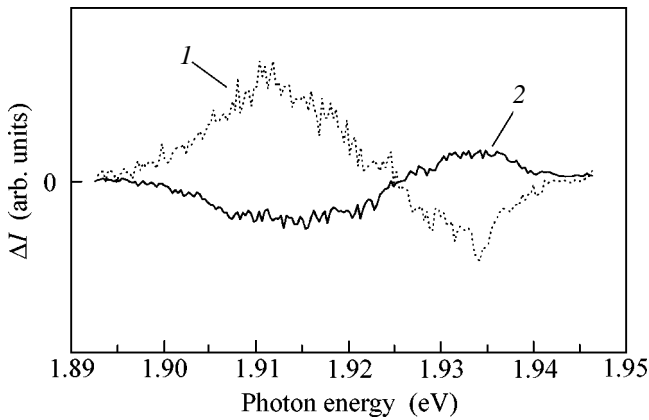


**Fig. 4.** Transformation of the luminescence signal from the ultrathin QW (1) with increasing temperature to 10 K and (2) under the action of phonon wind.

while the luminescence intensity in the range of short-wavelength wing (near the above-mentioned features) increases because of the migration of a part of the excitons from the low-energy states to the higher energy states. On further rise in temperature, the features smear out and disappear.

The situation where excitons migrate to the lower energy states through the mediation of equilibrium or nonequilibrium phonons is not unique. With an increase in temperature, the luminescence band maximum in low-dimensional structures (cf. [9, 10] and literature cited therein) often undergoes in a certain temperature range a long-wavelength shift that is larger than the change in the band gaps of the well and barrier materials. This occurs because excitons can migrate to the lower energy states via the “intermediate” (higher energy) states upon a temperature increase. However, this effect was not observed in our structure either upon quasi-resonant excitation or upon barrier (ZnTe) excitation. Moreover, such a thermally activated mechanism of exciton migration to the deeper states increases the fraction of nonradiatively recombining excitons [11] and, hence, diminishes the luminescence integrated intensity, whereas in our case it increases.

The exciton redistribution from the higher energy states (free excitons) to the lower energy states (excitons localized at the interface inhomogeneities) under the action of phonon wind was observed in [4] for a wide (10.2 nm) GaAs/Al<sub>0.33</sub>Ga<sub>0.67</sub>As QW. However, the situation in our case is different because of a considerable inhomogeneous broadening, so that one cannot speak about free excitons in our structure. For this reason, the explanation suggested in [4] that relates to the momentum transfer from the nonequilibrium phonons to the exciton subsystem does not apply in our case.

Attempts at furnishing a consistent analytical description of the lateral exciton transfer in a QW with fluctuating thickness at nonzero temperatures have encountered considerable difficulties [9]. The influence of nonequi-

librium phonons with unknown spectral distribution is also hard to take into account. We will restrict ourselves to a brief qualitative consideration of the problem.

The features related to the exciton relaxation involving confined and interface phonons (Fig. 3) are noteworthy. The photoexcited excitons emitting optical phonons (in a time shorter than 1 ps) fall within a rather narrow energy interval specified by  $\hbar\omega_1$  and  $\hbar\omega_2$ . Further relaxation can proceed only through much slower transitions promoted by the acoustic phonons. The characteristic time of such processes (tens of picoseconds) is comparable with the exciton radiative recombination time. Using the data presented in [12], one can approximately estimate this time (200–300 ps). Therefore, excitons are accumulated in a narrow energy range. In effect, the population of localized exciton states is inverted (with respect to the lower energy states) near the above-mentioned features. In such a situation, the phonon flux with energy comparable to the energy difference  $\Delta E$  between any closely spaced states (this situation is schematically illustrated in the inset in Fig. 3) must stimulate the induced phonon emission in the course of exciton transitions between these local potential minima. It is these processes, rather than the processes of phonon absorption, that are predominant. As a result, the population of the states with higher energy will diminish, while the population of the lower-energy states will increase, as is indeed observed in the experiment.

Of interest is the spectrum of nonequilibrium phonons reaching zone A. High-frequency acoustic phonons into which the optical phonons decay are characterized by short lifetimes due to spontaneous anharmonic decay and short mean free time (due to strong scattering by defects), resulting in their “localization” near the generation zone. The high-frequency acoustic phonons decay into lower frequency phonons that are capable of propagating to much greater distances. The characteristic energies of phonons reaching zone A will be discussed elsewhere; here we only briefly touch on this issue. In a bulk homogeneous material with almost isotropic (because of strong scattering [13]) phonon propagation, only a few phonons would reach zone A. One can thus assume that the phonons propagate in a quasi-two-dimensional (quasi-waveguide) regime. That we indeed deal with the quasi-two-dimensional propagation of nonequilibrium phonons is evident from the fact that the phonon wind effect did not quench even after the sample had been immersed in superfluid helium. As is well known [14], those phonons reaching sample boundaries pass to helium under these conditions. Since the phonons are generated in the region of ultrathin layers that are positioned near the sample surface, it might be expected that, due to strong scattering, the fraction of phonons reaching the structure/superfluid helium interface would be large enough. For this reason, one can expect that the phonon wind effect in the case of a three-dimensional quasi-diffusion phonon propagation regime will quench upon immersing the

sample in superfluid helium. However, this does not occur in the experiment.

**Conclusions.** The transformation of the QW luminescence spectrum under the action of phonon wind was observed. It is assumed that in the presence of an inverse population of localized states the nonequilibrium phonon flux stimulates lateral exciton migration over the local potential minima through the tunneling transitions accompanied by *induced* phonon emission. To explain the effect observed at low phonon generation level and for a macroscopic distance to the zone of quasi-resonant QW luminescence excitation, one has to assume that the nonequilibrium acoustic phonons in the structure under study propagate in a quasi-waveguide regime.

In our experiments, we dealt (1) with a nonequilibrium phonon flux of unknown spectral composition and (2) with the ensemble of excitons localized due to the fluctuation potential. It is conceivable that the nonequilibrium phonon fluxes with a given spectral composition can selectively act at low temperatures in heterostructures with predetermined parameters (geometry, energy level structure, etc.), allowing one to control the quasiparticle transport between “structural elements” and the population of energy levels in different structural elements. We mention in passing that these structures may serve as a base in designing quantum (phonon) amplifiers.

We are grateful to T.I. Galkina for interest in the work and valuable remarks, A.I. Sharkov for useful discussion, and S.R. Oktyabr'skiĭ for electron microscopy studies. This work was supported by the Russian Foundation for Basic Research (project nos. 00-02-17335 and 99-02-17183), the interdepartmental program FTNS of the Ministry of Science of the Russian Federation (project no. 97-1045), and the Grants for the Sup-

port of Scientific Schools (project no. 00-15-96568) and Young Scientists.

## REFERENCES

1. T. Takagahara, Phys. Rev. B **31**, 6552 (1985).
2. V. S. Bagaev, L. V. Keldysh, N. N. Sibel'din, *et al.*, Zh. Éksp. Teor. Fiz. **70**, 702 (1976) [Sov. Phys. JETP **43**, 362 (1976)].
3. E. S. Moskalenko, A. V. Akimov, A. L. Zhmodikov, *et al.*, Fiz. Tverd. Tela (St. Petersburg) **36**, 3140 (1994) [Phys. Solid State **36**, 1668 (1994)].
4. E. S. Moskalenko, A. V. Akimov, A. A. Kaplyanskii, *et al.*, Physica B (Amsterdam) **219–220**, 59 (1996).
5. A. V. Akimov, A. V. Scherbakov, A. L. Zhmodikov, *et al.*, Phys. Rev. B **56**, 12100 (1997).
6. V. S. Bagaev, G. Bel'ska-Levandovska, M. M. Bonch-Osmolovskii, *et al.*, Zh. Éksp. Teor. Fiz. **77**, 2117 (1979) [Sov. Phys. JETP **50**, 1013 (1979)].
7. V. V. Zaitsev, V. S. Bagaev, and E. E. Onishchenko, Fiz. Tverd. Tela (St. Petersburg) **41**, 717 (1999) [Phys. Solid State **41**, 647 (1999)].
8. J. Mendez, A. Pinczuk, J. P. Valladares, *et al.*, Appl. Phys. Lett. **50**, 1101 (1987).
9. S. D. Baranovskii, R. Eichmann, and P. Thomas, Phys. Rev. B **58**, 13081 (1998).
10. A. Polimeni, A. Patane, M. Henini, *et al.*, Phys. Rev. B **59**, 5064 (1999).
11. I. N. Krivorotov, T. Chang, G. D. Gilliland, *et al.*, Phys. Rev. B **58**, 10687 (1998).
12. J. H. Collet, H. Kalt, Le Si Dang, *et al.*, Phys. Rev. B **43**, 6843 (1991).
13. A. I. Sharkov, A. Yu. Klovov, T. I. Galkina, *et al.*, J. Russ. Laser Res. **21**, 478 (2000).
14. E. S. Sabisky and C. H. Anderson, Solid State Commun. **17**, 1095 (1975).

*Translated by V. Sakun*

# Mechanism of the Formation of a Soft Mode in Ferroelastic Phase Transition

S. V. Goryainov and N. N. Ovsyuk

*Institute of Mineralogy and Petrography, Siberian Division, Russian Academy of Sciences,  
Universitetskii pr. 3, Novosibirsk, 630090 Russia*

*e-mail: ovsyuk@uigmm.nsc.ru*

Received March 1, 2001

It is shown that the softening of the acoustic mode and the ensuing ferroelastic phase transition are due to the linear–quadratic interaction between the symmetric and antisymmetric deformations, which is presently neglected in the literature. An expression is obtained which can be used to predict the phase transition pressure if the initial elastic moduli are known. © 2001 MAIK “Nauka/Interperiodica”.

PACS numbers: 64.70.Kb; 61.50.Ks; 62.20.Dc

In recent years, lattice dynamics and molecular dynamics methods were used to numerically calculate the soft modes causing ferroelastic phase transitions in crystals [1, 2]. Calculations of this type do not use analytical expressions describing the mechanism for the appearance of soft modes. It is assumed that symmetry-breaking deformation arises spontaneously without applying any force and appears due to critical softening of elastic moduli. In the Landau theory of ferroelastic phase transitions, the free energy is expanded in powers of order parameters breaking crystal symmetry. The deformations not breaking symmetry are not treated as order parameters, because it is assumed that they are not involved in the transition. Next, it is postulated that the coefficient of the quadratic term of expansion, i.e., the elastic modulus, must vanish when the external variable thermodynamic parameter reaches its critical value. Within this approach, the reason for the formation of a soft mode remains unclear.

Of particular interest is physics of high-pressure ferroelastic phase transitions. Under pressure, the symmetry lowers to triclinic, after which amorphization occurs, as was demonstrated by an example of anorthite and quartz in [3, 4]. In this work, we consider the proper monoclinic–triclinic ferroelastic phase transition in Sr-anorthite ( $(\text{Sr,Ca})\text{Al}_2\text{Si}_2\text{O}_8$ ). A ferroelastic phase transition is considered proper when the order parameter and the spontaneous deformation behave identically under symmetry operations. In a proper ferroelastic phase transition, one of the components of the spontaneous deformation tensor can be taken as a critical parameter [1]. We studied a proper ferroelastic phase transition because in this case cell deformation can be treated as a whole, i.e., without specifying displacements of particular atoms, as in the case of an improper transition, and, hence, the mechanism of interaction between deformations of cell edges and

angles becomes more pictorial. We aimed at revealing the most general reason for crystal destabilization. We demonstrated that the soft acoustic mode responsible for the instability of the ferroelastic lattice is due to the linear–quadratic interaction between symmetric and antisymmetric deformations, which is presently neglected in the literature [5], although this interaction is the strongest among the anharmonic interactions.

In our previous work [6], we found that the energy of ferroelastic phase transition is due to symmetric components, and, therefore, their contributions cannot be neglected, as was done previously. The effect of symmetric components of the deformation tensor on the phase transition is accounted for by the term  $p_{\text{ext}}V$  in the Gibbs potential of a crystal subjected to external pressure  $G = F + p_{\text{ext}}V$ , where  $F$  is the free energy,  $V \approx e_1 + e_2 + e_3$  is the relative change in the volume of the unit cell, and  $e_i$  are components of the deformation tensor. The importance of making allowance for the effect of symmetric deformations was also pointed out in [7], where mechanical stress was calculated for a triatomic T–O–T molecule distorted under pressure from linear to bent. In that work, the authors examined how the transverse destabilizing force appears under the action of external forces applied to the molecule on two sides along the T...T line.

Recall that in the general case the symmetric and antisymmetric order parameters can be represented as the sum of the static and a small dynamic components related to lattice vibrations:  $Q_j = Q_{j\text{stat}} + Q_{j\text{dyn}}$ . The antisymmetric order parameters  $Q_{j\text{stat}}$  describe the system in thermodynamic equilibrium and are zero in the symmetric phase. The antisymmetric order parameters  $Q_{j\text{dyn}}$  describe lattice vibrations with certain frequencies  $\omega_j$  and wave vectors  $\mathbf{k}_j$  and occur in both symmetric and low-symmetry phases. On approaching the point of

phase transition, some vibrations with eigenfrequencies  $\omega_i(\mathbf{k}_i)$  are softened. In the case of the monoclinic–triclinic transition, the  $B_g$  representation, to which the acoustic branch belongs, is the eigenvalue of the dynamic matrix that accounts for the direction and polarization of the acoustic phonon wave vector. The stability condition for the dynamic matrix can be represented as  $(c_{44}c_{66} - c_{46}^2) > 0$ . This matrix corresponds to the propagation of three acoustic waves, with the lowest frequency soft mode being the transverse acoustic wave propagating along  $Y$  with the polarization  $[-c_{46}/c_{66}, 0, 1]$  [5].

Figure 1 shows the origin of the transverse antisymmetric force by an example of the phase transition in a triatomic T–O–T molecule. Solid lines show the static positions of atoms in thermodynamic equilibrium, and dashed lines show the transverse vibrations of the O atom. The forces  $F_r$  appear under the action of the contracted interatomic bonds, and their sum gives the tangential force  $F_t$  that provokes the bending phase transition in Fig. 1b if  $F_t > F_a$ , where  $F_a$  is the restoring force caused by the stiffness of the T–O–T angle.

In our analysis of the monoclinic–triclinic transition, we will use analogous reasoning. We assume that, on applying hydrostatic pressure to the unit cell, antisymmetric destabilizing forces also appear under the action of contracted interatomic bonds. By analogy with the triatomic molecule, Fig. 1 illustrates the action of static pressure and dynamic shear stress caused by a transverse acoustic wave on the monoclinic cell.

Let us consider a monoclinic cell with the normal to symmetry plane aligned with the  $Y$  axis. For this cell, the quadratic expansion of the free energy of deformation in the natural curvilinear  $q$  coordinates ( $r_i, \varphi_k$ ) is

$$F = \sum_{ij} c_{ij}^0 (\Delta r_i / r_{0i}) (\Delta r_j / r_{0j}) / 2 + \sum_{kl} c_{kl}^0 \Delta \varphi_k \Delta \varphi_l / 2, \quad (1)$$

where  $i, j = 1, 2, 3$ ;  $k, l = 4, 5, 6$ ;  $c_{ij}^0$  and  $c_{kl}^0$  are the initial elastic moduli in the symmetric phase; and  $r_{0i}$  are the initial cell parameters; small nondiagonal terms of the angle–bond type are omitted. For the sake of simplicity, we will first consider the two-dimensional deformation of one of the faces  $b_0 c_0$ , which includes the deformation of edges  $b_0$  and  $c_0$  and angle  $\alpha$ . In Fig. 1b it is seen that  $\Delta \alpha = \Delta z / b_0$ , where  $b_0$  is a parameter corresponding to the  $Y$  axis in the initial cell. The corresponding quadratic expansion of free energy is written as

$$F = c_{22}^0 (\Delta b / b_0)^2 / 2 + c_{23}^0 (\Delta b / b_0) (\Delta c / c_0) + c_{33}^0 (\Delta c / c_0)^2 / 2 + c_{44}^0 (\Delta z / b_0)^2 / 2. \quad (2)$$

Let us express this energy in Cartesian coordinates. Since the edge  $b_0$  departs in the  $Z$  direction under the

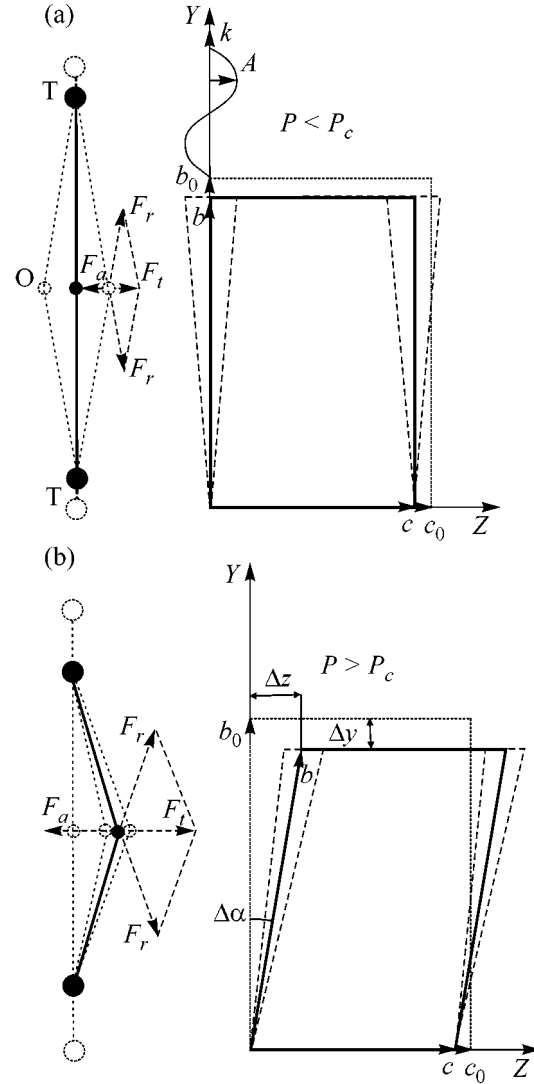


**Fig. 1.** Schematic illustration of phase transitions under the action of hydrostatic pressure  $P$  and transverse acoustic wave for the triatomic T–O–T molecule and the monoclinic crystal lattice (a) before and (b) after phase transition.

action of the acoustic wave, the power-series expansion of  $\Delta b$  has the form

$$\Delta b = [(b_0 + \Delta y)^2 + (\Delta z)^2]^{1/2} - b_0 \cong \Delta y + (\Delta z)^2 / 2b_0. \quad (3)$$

It is seen that  $\Delta b$  contains not only linear components along the  $Y$  axis, but also quadratic components along the perpendicular direction. This means that linear deformations in the natural curvilinear space, in which the deformations of chemical bonds and angles in the crystal lattice are considered, cause nonlinear deformations in Cartesian coordinates, in which atomic displacements are considered. In terms of the deformation tensor components, Eq. (3) takes the form  $\Delta b / b_0 = e_2 + e_4^2 / 2$ , because in the monoclinic cell  $\Delta \varphi_4 = \Delta \alpha = -e_4$ . As

a result, for the Gibbs energy  $G = F + p_{\text{ext}}V$ , one obtains the expression

$$G \cong c_{22}^0 e_2^2/2 + c_{23}^0 e_2 e_3 + c_{33}^0 e_3^2/2 + (c_{22}^0 e_2 + c_{23}^0 e_3 + c_{44}^0) e_4^2/2 + p_{\text{ext}}(e_2 + e_3), \quad (4)$$

from which it follows that, upon applying hydrostatic pressure to the unit cell, the symmetric static deformations of the  $e_{2\text{stat}}$  and  $e_{3\text{stat}}$  bonds come into linear–quadratic interaction with the dynamic deformations of the transverse acoustic wave  $e_{4\text{dyn}}$ , leading to a change in the force constants of transverse vibrations. Hence, for the direction of symmetry-breaking deformations distorting the cell so that the angle  $\phi_4 \neq 90^\circ$ , the effective force constant is

$$c_{44} = \partial^2 G / \partial e_4^2 = b_0^2 \partial^2 F / \partial z^2 = c_{44}^0 + c_{22}^0 e_2 + c_{23}^0 e_3. \quad (5)$$

Under equilibrium conditions,  $\partial G / \partial e_2 = c_{22}^0 e_2 + c_{23}^0 e_3 + p_{\text{ext}} = 0$ ; hence, for the symmetric phase one finds

$$c_{44} = c_{44}^0 - p_{\text{ext}}. \quad (6)$$

It is seen that the elastic modulus  $c_{44}$  softens upon the pressure buildup and vanishes (i.e., acoustic instability appears) at the critical pressure

$$p_c = c_{44}^0. \quad (7)$$

As was mentioned above, the amplitude vector of the soft acoustic mode has components not only along  $Z$ , but also along  $X$ . Therefore, for a more accurate quantitative estimation, one must introduce in Eq. (4) the second antisymmetric parameter  $e_6$ , which also softens under pressure. Now, because the edge  $b_0$  departs in the  $X$  and  $Z$  directions under the action of the acoustic wave, the power-series expansion of  $\Delta b$  has the form

$$\Delta b / b_0 \cong \Delta y / b_0 + (\Delta x)^2 / 2b_0^2 + (\Delta z)^2 / 2b_0^2 = e_2 + e_4^2/2 + e_6^2/2. \quad (8)$$

Due to the interaction between parameters  $e_4$  and  $e_6$ , the combination of moduli  $c_{44}c_{66} - c_{46}^2$  approaches zero faster than the individual modulus  $c_{44}$ ; therefore, after substituting expansion (8) into the Gibbs potential, one obtains that  $c_{44}c_{66} - c_{46}^2 = (c_{44}^0 - p)(c_{66}^0 - p) - (c_{46}^0)^2 = 0$  in the transition point. Hence,

$$p_c = (c_{44}^0 + c_{66}^0)/2 - [(c_{44}^0 + c_{66}^0)^2/4 - c_{44}^0 c_{66}^0 + c_{46}^{02}]^{1/2}. \quad (9)$$

Using the data for the initial moduli of Sr anorthite [1]  $c_{44}^0 = 11.6$  GPa,  $c_{66}^0 = 24.7$  GPa, and  $c_{46}^0 = -12.7$  GPa, one finds  $p_c = 3.86$  GPa, whereas the experimental pres-

sure for this transition is  $3.2 \pm 0.4$  GPa [8]. The above moduli were obtained within the pair potential model with parameters fitted so that the calculated and experimental cell parameters were the same. These calculated moduli should be considered as approximate because of the lack of experimental data for the elastic moduli of Sr anorthite. Therefore, it is unreasonable to expect full coincidence between the theory and experiment.

As a result, we have demonstrated that the soft acoustic mode responsible for the proper ferroelastic phase transition is caused by the linear–quadratic interaction between the static symmetric and the dynamic antisymmetric deformations, which is currently neglected in the literature, although it is the strongest among the anharmonic interactions. The authors of [5] justify the neglect of the terms  $e_i e_4^2$  by the fact that symmetric components  $e_i$  are smaller than  $e_4$  by about a factor of five. However, it follows from our expressions that the terms  $c_{44}^0$  and  $\sum_i c_{2i}^0 e_i$  with  $i = 1, 2, 3$ , and 5 must be compared rather than  $e_i$  and  $e_4$ . This interaction is common to structural phase transitions because it results from the nonlinear relation between the curvilinear natural coordinate space, in which the deformations of chemical bonds and angles in the crystal lattice are considered, and the Cartesian space of atomic displacements upon applying hydrostatic pressure to the ferroelastic. In addition, we have obtained an expression which can be used to predict phase transition pressure provided that the initial elastic moduli are known.

This work was supported by the Russian Foundation for Basic Research, project nos. 00-05-65429, 00-05-65305, and 01-05-65373.

## REFERENCES

1. M. T. Dove and S. A. T. Redfern, *Am. Mineral.* **82**, 8 (1997).
2. G. W. Watson and S. C. Parker, *Phys. Rev. B* **52**, 13306 (1995).
3. S. A. T. Redfern, *Miner. Mag.* **60**, 493 (1996).
4. S. V. Goryaĭnov and N. N. Ovsyuk, *Pis'ma Zh. Éksp. Teor. Fiz.* **69**, 431 (1999) [*JETP Lett.* **69**, 467 (1999)].
5. M. A. Carpenter and E. K. H. Salje, *Eur. J. Mineral.* **10**, 693 (1998).
6. S. V. Goryaĭnov and N. N. Ovsyuk, *Zh. Éksp. Teor. Fiz.* **118**, 906 (2000) [*JETP* **91**, 786 (2000)].
7. A. P. Mirgorodsky and M. B. Smirnov, *Ferroelectrics* **159**, 133 (1994).
8. M. D. McGuinn and S. A. T. Redfern, *Miner. Mag.* **58**, 21 (1994).

*Translated by A. Safonov*

# Nuclear Ferromagnetism and Superconductivity at Negative Nuclear Temperatures

A. M. Dyugaev, I. D. Vagner, and P. Wyder

Landau Institute for Theoretical Physics, Russian Academy of Sciences,  
Chernogolovka, Moscow region, 142432 Russia

Received March 7, 2001

Quantitative theory of the effect of nuclear ferromagnetism on the superconductivity of metals is proposed taking into account the electron–nuclear spin–spin interactions. At negative nuclear temperatures, when the nuclear magnetization is in opposition to an external magnetic field, nuclear ferromagnetism is favorable to superconductivity rather than suppressing it. The critical magnetic field in Be and  $\text{TiH}_{2.07}$  hydrate metals may exceed the critical field of a nonmagnetic superconductor by an order of magnitude. © 2001 MAIK “Nauka/Interperiodica”.

PACS numbers: 74.25.Nf

1. The coexistence of nuclear ferromagnetism and superconductivity was discovered in  $\text{AuIn}_2$  metal, whose critical magnetic field  $H_{c0} = 14.5$  Hz is small at temperatures  $T$  well below  $T_{ce} = 0.207$  K [1]. The critical field  $H_c(T)$  was found to strongly decrease at  $T < T_{cn} = 35$   $\mu\text{K}$ , where  $T_{cn}$  is the phase transition temperature into the nuclear ferromagnetic state. It was pointed out in [2] that nuclear ferromagnetism may suppress superconductivity. The theory of competing superconductivity and electronic ferromagnetism was suggested in [3] and extended to nuclear ferromagnetism in [4, 5]. We have emphasized in [6] that there is no full analogy between electronic ferromagnetism and nuclear ferromagnetism in superconductors. Electronic ferromagnetism occurs upon lowering  $T$  in the superconducting phase of a metal. This results in a spiral or domain structure that adjusts to the superconducting order parameter [7]. However, by the very statement of the experiment [1], nuclear ferromagnetism appears upon lowering of the temperature in the normal phase of a metal, while the superconducting transition occurs upon reduction of the magnetic field only after, on the background of the formed nuclear magnetic structure whose rearrangement time is exceedingly long. In other words, there is no need to take into account the back action of superconductivity on nuclear ferromagnetism. The interpretation of the experimental data on  $\text{AuIn}_2$  [1] is not easy because the appearance of a spontaneous nuclear moment in this metal is due to the spin–spin nuclear interactions, and it is unclear which type of magnetic domain structure will form in this case. Because of this, we proposed in [6] the experimental methodology that was later independently implemented in [8, 9] for Al and Sn metals. It is based on the fact that single-domain nuclear ferromagnetism can be obtained by adiabatic demagnetization at high nuclear

temperatures  $T_n > T_{cn}$ , when the effects caused by the appearance of a spontaneous nuclear moment can be ignored. The superconducting transition occurs at electron temperature  $T \gg T_n$  and magnetic field  $H_c(T)$  other than the field  $H_{c0}(T)$  in nonmagnetic metals. To a first approximation, this difference can be determined from the expression [3]

$$H_c(T) = H_{c0}(T) - 4\pi(1 - n)M_n(H_c), \quad (1)$$

where  $M_n$  is the nuclear moment density and  $n$  is the demagnetization factor depending on the sample geometry. At  $T \ll T_{ce}$ , the field  $H_{c0}(T)$  shows little dependence on the electron temperature  $T$ :

$$H_{c0}(T) = H_{c0}(0)(1 - T^2/T_{ce}^2). \quad (2)$$

For an ideal system of nuclear spins in a strong magnetic field, the moment  $M_n$  does not change upon adiabatic demagnetization,

$$M_n(H_i) = M_{n0}B_s(X) \quad X = \mu_n H_i / ST, \quad (3)$$

where  $M_{n0}$  is the saturation value for  $M_n$ ;  $B_s$  is the Brillouin function; and  $\mu_n$  and  $S$  are the nuclear magnetic moment and spin, respectively. It is assumed that the initial field  $H_i \gg h$ , where  $h$  is the local magnetic field. The final nuclear temperature  $T_n$  and the moment  $M_n(H_f)$  in the final field  $H_f$  of adiabatic demagnetization are given by [10]

$$M_n(H_f) = M_n(H_i) \frac{H_f}{\sqrt{h^2 + H_f^2}}, \quad T_n = T \frac{\sqrt{H_f^2 + h^2}}{H_i}. \quad (4)$$

The parameters  $H_c$  and  $H_{c0}$  are measured experimentally, so that  $M_n$  can be found using Eq. (1) and compared with the value calculated by Eqs. (3) and (4). For

Al one has  $h \ll H_c$  and  $M_n(H_i) \cong M_n(H_c)$ , and it was found in [7] that there is a small though detectable difference between the  $M_n$  values determined from Eqs. (1) and (3) for  $M_n$  close to its saturation value  $M_{n0}$ .

**2.** We now show that the linear relationship between  $H_c - H_{c0}$  and  $M_n$  is merely the leading term in the expansion of  $H_c - H_{c0}$  in powers of  $M_n$  and, thereby, explain the effect observed in [8] for Al. Let us take into account that, apart from the purely electrodynamic effect of ferromagnetism on superconductivity [3], the Cooper pair breaking mechanism can also be associated with the electron magnetizing by nuclear spins. This effect was considered for a nonuniform order parameter in superconductors [11, 12]. Nuclear ferromagnetism removes the spin degeneracy of electronic states in the  $M_n$  direction [11, 12],

$$E_{\pm} = \sqrt{\Delta^2 + \xi^2} \pm J.$$

The parameter  $J$  is related to the effective nuclear spin field  $H_n$  as  $J = \mu_e H_n$ , where  $\mu_e$  is the electron magnetic moment [6]. The field  $H_n$  is proportional to  $M_n$  and reaches maximum value  $H_{n0}$  for saturated  $M_n$ ,

$$H_n = H_{n0} M_n^*; \quad J = J_0 M_n^*; \quad J_0 = (\mu_e H_{n0}), \quad (5)$$

where  $M_n^*$  is the reduced nuclear moment  $M_n^* = M_n/M_{n0}$ . The critical field of a superconductor is determined from the general thermodynamic relation [13]

$$F_n - F_s = B_c^2/8\pi; \quad B_c = H_c + 4\pi(1-n)M_n. \quad (6)$$

The difference  $F_n - F_s$  in the free energies of the normal and superconducting metals at low temperatures  $T \ll T_{ce}$  can be found by the methods developed in [13],

$$F_n - F_s = \frac{1}{4}v \left( \Delta_0^2 - \frac{2\pi^2 T^2}{3} - 2J^2 \right), \quad (7)$$

where  $v$  is the density of electronic states and  $\Delta_0 = 1.76T_{ce}$ . The critical value  $J = \Delta_0/\sqrt{2}$  corresponds to the phase transition of a superconductor to the normal phase or to the state with nonuniform condensate at  $T = 0$  [11, 12]. Equations (6) and (7) can be used to deduce relationship between the critical magnetic fields in magnetic  $H_c$  and nonmagnetic  $H_{c0}$  metals,

$$\begin{aligned} & [H_c(T) + 4\pi M(H_c)(1-n)]^2 \\ &= H_{c0}^2(T) - 2 \frac{J^2(H_c)}{\Delta_0^2} H_{c0}^2(0), \end{aligned} \quad (8)$$

where  $H_{c0}(T)$  is found from Eqs. (6) and (7) at  $M_n = J = 0$ :

$$v\Delta_0^2 = \frac{H_{c0}^2(0)}{2\pi}; \quad H_{c0}(T) = H_{c0}(0) \left( 1 - \frac{\pi^2 T^2}{3\Delta_0^2} \right). \quad (9)$$

The accuracy of Eqs. (8) and (9) is determined only by the domain of applicability of the BCS theory. These

expressions can be used to derive the parameter  $M_n$  from the measured values of  $H_c$  and  $H_{c0}$  or to determine the critical field shift  $H_c - H_{c0}$  from the calculated  $M_n$  value. At ultralow temperatures, the difference between  $H_{c0}(T)$  and  $H_{c0}(0)$  can be ignored and Eq. (8) transforms to the relation between  $H_c$  and  $H_{c0}$  obtained in our work [6] for a cylindrical sample ( $n = 0$ ):

$$(H_c + 4\pi M_n)^2 = H_{c0}^2 \left( 1 - 2 \frac{J^2}{\Delta_0^2} \right). \quad (10)$$

**3.** In what follows, we restrict ourselves to the analysis of simplified Eq. (10) and consider two cases,  $M_n > 0$  and  $M_n < 0$ . The sign of nuclear magnetization depends on the method of its ‘‘preparation.’’ If the nuclear spins are in thermodynamic equilibrium at the initial stage of adiabatic demagnetization, then the signs of  $H$  and  $M_n$  will coincide regardless of the sign of nuclear moment; i.e.,  $M_n$  is aligned with  $H$ . In the case of dynamic nuclear polarization using the nuclear Overhauser effect, the nuclear temperature for negative  $\mu_n$  (Be, Rh, and Cd) is negative and  $M_n$  is antialigned with  $H$  [14]. The sign of nuclear magnetization can be changed by the well-elaborated experimental method of obtaining negative nuclear temperatures by rapidly turning over the external magnetic field [15].

For positive nuclear temperatures,  $M_n > 0$  and Eq. (10) has only one solution for  $H_c$ ,

$$H_c = H_{c0} \left( 1 - 2 \frac{J^2}{\Delta_0^2} \right)^{1/2} - 4\pi M_n. \quad (11)$$

The nuclear spin field  $H_{n0}$  and the parameter  $J_0$  in Eq. (5) can be estimated from the relationship [14]

$$H_{n0} = KM_{n0}/\chi, \quad (12)$$

where  $K$  is the Knight shift and  $\chi$  is the electronic magnetic susceptibility. The latter is known only for two metals Li and Na, in which  $\chi \approx 10^{-6}$ . The theory of Fermi liquid gives the following expression for  $\chi$  [13]:

$$\chi = \mu_e^2 v / (1 + B_0). \quad (13)$$

Using Eqs. (12) and (13) and relation (9) connecting the density of states  $v$  with  $H_{c0}$  and  $\Delta_0$ , one obtains for  $J_0/\Delta_0 \equiv \lambda$

$$\lambda = (1 + B_0)\lambda_0; \quad \lambda_0 = \epsilon \frac{\Delta_0 K}{(\mu_e H_{c0})}; \quad \epsilon = \frac{4\pi M_{n0}}{H_{c0}}. \quad (14)$$

All parameters in this expression, except for the Fermi-liquid constant  $B_0$ , are experimentally measurable quantities. The parameter  $\epsilon$  is determined for all known superconductors in [16]. Making use of Eqs. (11) and (14), one obtains the following relation between the reduced critical field  $H_c^* = H_c/H_{c0}$  and the reduced nuclear magnetization  $M_n^* = M_n/M_{n0}$ :

$$H_c^* = (1 - 2\lambda^2 M_n^{*2})^{1/2} - \epsilon M_n^*. \quad (15)$$

According to Eqs. (3) and (4), the reduced moment  $M_n^*$  depends on  $H_c$  and  $T$  as

$$M_n^*(H_c, T) = \frac{H_c}{\sqrt{H_c^2 + h^2}} B_s \left( \frac{\mu_n H_i}{ST} \right). \quad (16)$$

For most superconductors, the parameters  $\lambda$  and  $\epsilon$  are small. For example, in Al  $\lambda_0 = 0.03$  [Eq. (14)],  $\epsilon = 0.13$  [16], and  $H_{c0} \gg h$ , so that

$$H_c^* \cong 1 - \lambda^2 B_s^2 - \epsilon B_s. \quad (17)$$

Consequently, the measurement of  $H_c^*$  provides a basic opportunity to determine  $\lambda$  and the Fermi liquid constant  $B_0$  from Eqs. (14) and (17).

For the Be and Rh metals, the parameter  $\epsilon$  is large,  $\epsilon \approx 8$  [16], and one can expect, according to Eq. (15), that superconductivity is strongly suppressed by nuclear ferromagnetism. However, the local field in Rh is high,  $h \approx 7 H_{c0}$  [17], while the nonzero quadrupole moment of the Be nucleus is equivalent to the presence of a certain effective local field [10]. For metals with low critical fields,  $H_{c0} \ll h$ , one may set  $\lambda = 0$  in Eq. (15), because the reduced moment  $M_n^*(H_c)$  in this case is necessarily small [see Eq. (16)],

$$H_c^* \cong \left[ 1 + \frac{4\pi M_{n0}}{h} B_s(X) \right]^{-1}. \quad (18)$$

The correctness of Eq. (16) in a weak  $H_c$  field is questionable. The statement that the local field  $h$  is identical for all observables needs refinement. The definition of effective field  $H_{\text{eff}} = (H^2 + h^2)^{1/2}$  contradicts the experiments on measuring zero-field  $H$  nuclear specific heat at  $T > T_{cn}$ . For several very different substances  $\text{He}^3$ ,  $\text{AuIn}_2$ , and  $\text{PrNi}_5$ , the  $c_n \sim 1/T$  law is observed at  $H \ll h$  instead of the expected  $c_n \sim (H^2 + h^2)/T^2$  dependence [18]. In this connection, the inverse problem of determining  $M_n$  from the experimental dependence of  $H_c$  on the initial conditions of nuclear demagnetization and the problem of determining the  $M_n^*/B_s$  ratio in Eq. (16) seem to be more topical than the revelation of the interconnection between  $H_c$  and  $M_n$ . One has from Eq. (15)

$$M_n^* = \frac{[\epsilon^2 + 2\lambda^2(1 - H_c^{*2})]^{1/2} - \epsilon H_c^*}{2\lambda^2 + \epsilon^2}. \quad (19)$$

The domain of applicability of Eqs. (15) and (19) is restricted by the condition  $\sqrt{2}\lambda M_n^* < 1$ . For Be, the  $\lambda$  parameter is very small, while only  $\lambda_0$  from Eq. (14) can be determined for Rh resulting in  $\lambda_0 = 2.5$ . At  $\sqrt{2}M_n^*\lambda > 1$ , conventional superconductivity is impossible [11, 12].

**4.** At negative nuclear temperatures, the external magnetic field  $H$  and the nuclear magnetization  $M_n$  have different signs. Because of this, Eq. (10) can have two solutions  $H_{c\pm}$ . In the reduced variables  $H_c/H_{c0} = H_c^*$ ,  $4\pi M_{n0}/H_{c0} = \epsilon$ , and  $h^* = h/H_{c0}$ , one obtains from Eqs. (10) and (16)

$$H_{c\pm}^* = |\epsilon| M_n^* \pm (1 - 2\lambda^2 M_n^{*2})^{1/2},$$

$$M_n^* = \frac{H_{c\pm}^*}{\sqrt{H_{c\pm}^{*2} + h^{*2}}} B_s(X), \quad X = \frac{\mu_n H_i}{ST}. \quad (20)$$

The first solution  $H_{c+}^*$  exists at any ratio between the parameters  $\epsilon$  and  $h^*$ , at least for small  $X = \mu_n H_i / ST$  when  $2\lambda^2 M_n^{*2} < 1$ . The domain of existence of the second solution is restricted by the condition  $H_{c-} > 0$ . The solution does not exist, e.g., if  $h^* > |\epsilon|$  because  $B_s(X) < 1$ :

$$H_{c-}^* = \frac{(1 - 2\lambda^2 M_n^{*2})^{1/2}}{|\epsilon| B_s(X) / (H_{c-}^{*2} + h^{*2})^{1/2} - 1}. \quad (21)$$

Hence, the relation between  $4\pi M_{n0}$  and  $h$ , i.e., between  $|\epsilon|$  and  $h^*$ , becomes important. For Rh, the measured value  $h = 0.34$  Hz [17],  $4\pi M_{n0} = 0.4$  Hz, and  $H_{c0} = 0.049$  Hz [16]; i.e.,  $\epsilon \gg 1$ ,  $h^* \gg 1$ , and  $\epsilon \approx h^*$ . The dependences of the critical field  $H_c^*$  of Rh on the reduced temperature  $TS/\mu_n H_i = 1/X$  are presented in Fig. 1 for different values of parameter  $\lambda$ .

For Be, one has  $4\pi M_{n0} = 9.1$  Hz and  $H_{c0} = 1.1$  Hz [16]. The local field  $h$  in Be is unknown because the contribution from the quadrupolar effects is indeterminate. Figure 2 shows the dependence of  $H_c^*$  on  $1/X$  for  $\lambda = 0$  and different values of  $h^*$  in Be. Note that the strong inequality  $h \ll 4\pi M_{n0}$ , i.e.,  $h^* \ll \epsilon$ , cannot occur. Indeed, the local field  $h$  cannot be smaller than the dipolar contribution  $h_{\text{dip}}$ , for which the following expression is given in [10]:

$$h_{\text{dip}}^2 = \mu_n^2 \frac{S+1}{S} \sum \frac{1}{R_i^6}, \quad (22)$$

where  $R_i$  are the reciprocal lattice vectors. For example, in a cubic lattice

$$h_{\text{dip}}^2 \cong \mu_n^2 \frac{S+1}{S} 6n_n^2, \quad (23)$$

where  $n_n$  is the nuclear concentration. Since  $M_{n0} = \mu_n n_n$ , the  $h/4\pi M_{n0}$  ratio can only be small numerically. It is pointed out in [16] that the experimental observation of the effect of nuclear ferromagnetism on the superconductivity of Be and Rh is hampered. Because of a large Koringa constant  $\kappa \approx 1.8 \times 10^4$  Ks, it is difficult to carry out an experiment on nuclear demagnetization in Be. The critical field  $H_{c0}$  in Rh is low, and it is hard to pre-

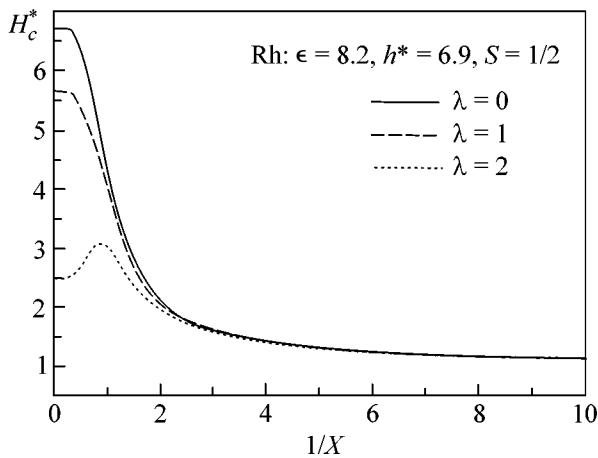


**Fig. 1.** Reduced critical field  $H_c^*$  of Rh vs. effective temperature  $1/X$  for different values of parameter  $\lambda$ . The reduced local field  $h/H_{c0} = 6.9$ . The parameter  $\epsilon = 8.2$ . Nuclear spin  $1/2$ .

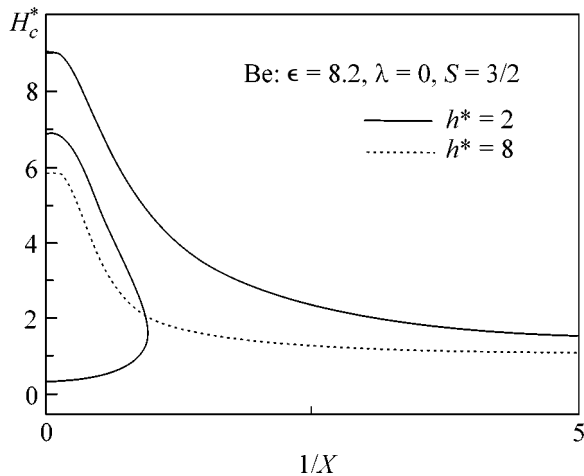


**Fig. 2.** Reduced critical field  $H_c^* = H_c/H_{c0}$  of Be vs.  $1/X$  for different values of local field  $h^*$ ;  $\lambda = 0$  and  $\epsilon = 8.2$ . Nuclear spin  $3/2$ .

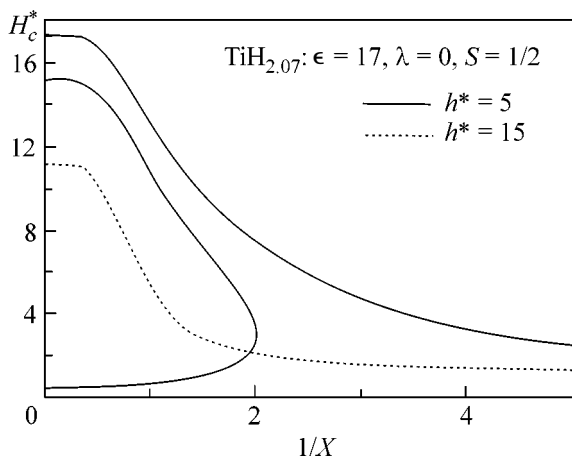


**Fig. 3.** Temperature dependences of the critical field  $H_c^*$  of  $\text{TiH}_{2.07}$  hydrate for two values of local field  $h^* = 5$  and  $15$ ;  $\lambda = 0$  and  $\epsilon = 17$ . Nuclear spin  $1/2$ .

pare a sample with a low concentration of magnetic impurities. It is argued in [16] that the experimental study of  $\text{TiH}_{2.07}$  hydrate, whose critical field  $H_{c0} = 1$  G and nuclear magnetization  $4\pi M_{n0} \approx 17$  G, i.e., for which  $\epsilon = 17 \gg 1$ , holds much promise. Because the other characteristics of  $\text{TiH}_{2.07}$  are unknown to us, we calculated the  $H_c^*$  ( $1/X$ ) dependence for this metal for several values of the reduced local field  $h^*$  at  $\lambda = 0$  (Fig. 3). One can see from Figs. 1–3 that nuclear ferromagnetism “enhances” superconductivity at negative nuclear temperatures rather than suppressing it. This is the key result of this work.

This work was supported by the Russian Foundation for Basic Research, project no. 00-02-17729.

## REFERENCES

1. S. Rehmman, T. Herrmannsdörfer, and F. Pobell, *Phys. Rev. Lett.* **78**, 1122 (1997).
2. A. M. Dyugaev, I. D. Vagner, and P. Wyder, *Pis'ma Zh. Éksp. Teor. Fiz.* **64**, 193 (1996) [*JETP Lett.* **64**, 207 (1996)].
3. V. L. Ginzburg, *Zh. Éksp. Teor. Fiz.* **31**, 202 (1957) [*Sov. Phys. JETP* **4**, 153 (1957)].
4. M. L. Kulic, A. I. Buzdin, and L. N. Bulaevskii, *Phys. Rev. B* **56**, R11415 (1997).
5. E. B. Sonin, *J. Low Temp. Phys.* **110**, 411 (1998).
6. A. M. Dyugaev, I. D. Vagner, and P. Wyder, *Pis'ma Zh. Éksp. Teor. Fiz.* **65**, 772 (1997) [*JETP Lett.* **65**, 810 (1997)].
7. L. N. Bulaevskii, A. I. Buzdin, M. L. Kulic, and S. V. Panyukov, *Agv. Phys.* **34**, 175 (1985).
8. M. Seibold, T. Herrmannsdörfer, and F. Pobell, *J. Low Temp. Phys.* **110**, 363 (1998).
9. T. Herrmannsdörfer, *Physica B (Amsterdam)* **280**, 368 (2000).
10. L. C. Hebel, *Solid State Phys.* **15**, 409 (1963).
11. A. I. Larkin and Y. N. Ovchinnikov, *Zh. Éksp. Teor. Fiz.* **47**, 1136 (1964) [*Sov. Phys. JETP* **20**, 762 (1965)].
12. P. Fulde and R. A. Ferrell, *Phys. Rev.* **135**, 1550 (1964).
13. A. A. Abrikosov, L. P. Gor'kov, and E. I. Dz'yaloshinski, *Methods of Quantum Field Theory in Statistical Physics* (Fizmatgiz, Moscow, 1962; Prentice-Hall, Englewood Cliffs, 1963).
14. A. Abragam, *The Principles of Nuclear Magnetism* (Clarendon Press, Oxford, 1961; Inostrannaya Literatura, Moscow, 1963).
15. A. S. Oja and O. V. Lounasmaa, *Rev. Mod. Phys.* **69**, 1 (1997).
16. T. Herrmannsdörfer, S. Rehmman, M. Seibold, and F. Pobell, *J. Low Temp. Phys.* **110**, 405 (1998).
17. P. J. Hakonen, R. T. Vourinen, and J. E. Martikainen, *Phys. Rev. Lett.* **70**, 2818 (1993).
18. T. Herrmannsdörfer and F. Pobell, *J. Low Temp. Phys.* **100**, 253 (1995).

*Translated by V. Sakun*

# Application of the Monte Carlo Method to the Problem of Surface Segregation Simulation

L. V. Poyurovskii<sup>1,2</sup>, A. V. Ruban<sup>3</sup>, I. A. Abrikosov<sup>2</sup>,  
Yu. Kh. Vekilov<sup>1</sup>, and B. Johansson<sup>2</sup>

<sup>1</sup> Moscow Institute of Steel and Alloys, Leninskiĭ pr. 4, Moscow, 117419 Russia

<sup>2</sup> Physics Department, Uppsala University, SE-75121 Uppsala, Sweden

e-mail: leonid@fysik.uu.se

<sup>3</sup> University of Denmark, DK-2800 Lyngby, Denmark

Received January 30, 2001; in final form, March 12, 2001

A generalization of the Monte Carlo method to the case of grand canonical ensemble allowing the elimination of the problem of determination of the chemical potential of alloy components was proposed. The method is particularly convenient for the calculations of surface segregations because it excludes time-consuming calculation of the temperature-dependent bulk chemical potential  $\mu(T)$ . The new method was used for calculating segregations at the (100), (110), and (111) surfaces of the Ni<sub>50</sub>Pd<sub>50</sub> alloy using the Ising model with *ab initio* effective interatomic interaction potentials. © 2001 MAIK “Nauka/Interperiodica”.

PACS numbers: 64.75+g; 02.70.Uu; 75.10.Hk

The concentration of components at the surface of an alloy can strongly differ from the bulk concentration because of the existence of surface segregations. However, the experimental determination of the concentration profile at the surface is an extremely difficult problem [1]; therefore, of particular value are theoretical methods for the simulation of surface segregations.

For determining the equilibrium concentration profile at the surface of a binary alloy, it is necessary to find the surface free energy  $F(T) = -kT \ln \sum_s (-E_{\text{surf}}(\sigma_s)/kT)$  of a system with a surface, where  $\sigma = \{\sigma_1 \dots \sigma_N\}$  is the surface configuration,  $\sigma_1 \dots \sigma_N$  are occupation numbers for  $N$  lattice sites at the surface ( $\sigma_i = 1$  if the  $i$ th site is occupied by an atom of type A, and  $\sigma_i = -1$  if the  $i$ th site is occupied by an atom of type B),  $E_{\text{surf}}(\sigma)$  is the surface energy corresponding to a given configuration, and summation is over all  $s$  possible configurations  $\sigma$ . Modern *ab initio* methods [2–4] provide sufficiently accurate determination of surface energy  $E_{\text{surf}}$  for the given surface configuration  $\sigma$ ; however, because of the huge number of possible surface configurations, direct calculation of surface free energy as a logarithm of the partition function is practically impossible.

Therefore, for the calculation of the segregation profile, the dependence of surface energy  $E_{\text{surf}}$  or total surface energy  $E_{\text{surf}}^{\text{tot}}$  on the surface configuration  $\sigma$  is usually written in the form of an effective Hamiltonian of the Ising type [5] as a function of occupation numbers  $\sigma_1 \dots \sigma_N$  and configurationally independent one-, two-, and many-body effective potentials of interatomic interaction. Next, statistical mechanics methods are

used for finding the equilibrium segregation profile corresponding to the given effective Hamiltonian at temperature  $T$  and bulk concentration  $c$ . Thus, the theoretical calculation of the equilibrium concentration profile is carried out in two steps: calculation of effective interatomic interaction potentials in the Hamiltonian, which can be performed by *ab initio* methods [6–9], and statistical calculation of the equilibrium segregation profile.

In this work, we focus on the application of the Monte Carlo (MC) method to the calculation of surface segregations within the Ising model.

For the MC calculation of the thermodynamically stable configuration of an alloy, the dependence of total energy  $E_{\text{tot}}(\sigma)$  on configuration  $\sigma$  can be represented as an effective Hamiltonian of the Ising type. In the bulk, this Hamiltonian has the form

$$E_{\text{tot}}(\sigma) = V^{(0)} + \sum_i \left[ V^{(1)} \sigma_i + \frac{1}{2!} \sum_{j \neq i} V^{(2,s)}(s^{ij}) \sigma_i \sigma_j + \frac{1}{3!} \sum_{k \neq j \neq i} V^{(3,s)}(s^{ijk}) \sigma_i \sigma_j \sigma_k + \dots \right], \quad (1)$$

where summation is over all  $N$  atoms of the alloy,  $V^{(0)}$  is the energy of a completely disordered equiatomic alloy,  $V^{(1)}$  is the one-body effective potential, and  $V^{(m,s)}(s^{ijk\dots})$  are effective  $m$ -body interatomic interaction potentials depending only on the spatial configuration of the corresponding  $m$ -atomic cluster  $s^{ijk\dots}$ . Only a finite number of effective interactions is included in

Hamiltonian (1), i.e.,  $V^{(m,s)}(s^{ijk\dots}) \neq 0$  only for some of the clusters  $s^{ijk\dots}$ , usually those involving neighboring atoms. Because of the existence of some maximum interaction radius  $R_{\max}$ , all potentials  $V^{(m,s)}(s^{ij\dots})$  for atoms  $i$  and  $j$  separated by distances larger than  $R_{\max}$  are zero.

In bulk MC calculations, one can use a canonical ensemble; then the one-body contribution  $\sum_i V^{(1)} \sigma_i = NV^{(1)}\langle\sigma\rangle$  is constant and can be neglected. In this case, the MC steps are performed as follows: using effective Hamiltonian (1), a change in the energy of the alloy (trial energy)  $\Delta E$  is calculated for the exchange of two atoms of types  $A$  and  $B$  chosen at random in the  $N$ -atomic three-dimensional crystal lattice (with periodic boundary conditions). Next, one of the MC algorithms (e.g., asymmetric Metropolis algorithm [13]) is used to decide on the atom exchange. Successive steps are performed until the total energy  $E_{\text{tot}}(\sigma)$  at the given temperature  $T$  becomes stable.

The dependence of total surface energy  $E_{\text{surf}}^{\text{tot}}(\sigma)$  on the surface configuration  $\sigma$  of the alloy can also be represented in the form of an effective Hamiltonian [6, 8] similar to Hamiltonian (1):

$$E_{\text{surf}}^{\text{tot}}(\sigma) = V^{(0)} + \sum_i \left[ V_{\lambda}^{(1)} \sigma_i + \frac{1}{2!} \sum_{j, j \neq i} V_{\lambda\lambda'}^{(2,s)}(s_{\lambda\lambda'}^{ij}) \sigma_i \sigma_j + \dots \right], \quad (2)$$

where effective potentials depend now not only on the order of the corresponding cluster  $s$  and mutual arrangement of its atoms, as in the bulk case, but also on the position of the cluster  $\lambda\lambda'\dots$  with respect to the surface ( $\lambda$  and  $\lambda'$  denote the layers in which the cluster atoms are located). In this case, effective potentials  $V$  are considered renormalized because surface affects only a few near-surface layers, whereas in the deeper layers the potentials are fixed at bulk values.

Because the concentration of components in the near-surface region is not fixed, it is reasonable to perform the MC simulation at the surface using the grand canonical ensemble approximation. In this case, only a change of the atom type from  $A$  to  $B$  in the  $i$ th site is considered, and, hence, the trial energy  $\Delta E$  is equal to  $\Delta E_{\text{surf}}^{\text{tot}} - \mu$ , where  $\Delta E_{\text{surf}}^{\text{tot}}$  is a change in the total surface energy upon the replacement, as calculated by Eq. (2), and  $\mu = \mu_A - \mu_B$  is the bulk chemical potential. The bulk chemical potential  $\mu$  at temperature  $T$  is equal to  $dF(T, \langle\sigma\rangle)/d\langle\sigma\rangle$ , where  $F(T, \langle\sigma\rangle)$  is the free energy of alloy per atom,  $\langle\sigma\rangle = 2c - 1$  is the average over occupation numbers, and  $c$  is concentration. Correspondingly,  $\mu$  depends on temperature  $T$  and cannot be obtained

from the *ab initio* results for  $T = 0$ , contrary to effective potentials  $V$ .

Several techniques were proposed in the literature for avoiding the problem associated with the calculation of bulk chemical potential  $\mu(T)$  [10–12] by the simulation of surface segregations in the canonical ensemble approximation with fixed concentrations of components in the sample or by the calculation of chemical potential  $\mu(T)$  using the bulk MC method.

However, in the case of canonical ensemble, a great number of layers must be included in the MC cell. In the case of grand canonical ensemble, the difficulties are associated with the calculation of temperature-dependent chemical potential  $\mu(T) = dF(T)/d\langle\sigma\rangle$ .

In this work, we propose a version of the MC method that makes it possible to avoid the calculation of chemical potential without expanding the size of the MC cell. Let us consider in the canonical ensemble approximation the atom exchange between the thermodynamically equilibrium thermostat (bulk) and a subsystem small compared to the thermostat (surface). In this case, the alloy atoms in the bulk are characterized by a certain distribution function  $\rho(E_{at})$  over the spectrum of possible energy values. The energy of the  $i$ th atom  $E_{at}(\sigma', \sigma_i)$  in the model with effective Ising Hamiltonian (1) has the form

$$E_{at}(\sigma', \sigma_i) = \frac{V^{(0)}}{N} + V^{(1)} \sigma_i + \frac{1}{2!} \sum_{j \neq i} V^{(2,s)} \sigma_i \sigma_j + \dots, \quad (3)$$

where  $\sigma' = \sigma_1, \dots, \sigma_{i-1}, \sigma_{i+1}, \dots, \sigma_{Z+1}$  is the configuration of the alloy at all  $Z$  sites with which the central  $i$ th atom interacts.

On going from the surface to the bulk, an atom of type  $\sigma$  with the probability  $\rho(E_{at})$  will occur in the state with energy  $E_{at}(\sigma', \sigma)$  and the change in the energy of the entire system will be

$$\Delta E = \Delta E_{\text{bulk}}(\sigma_i \longrightarrow -\sigma_i) + \Delta E_{\text{surf}}(-\sigma_i \longrightarrow \sigma_i) = E_{at}(\sigma', -\sigma) - E_{at}(\sigma', \sigma) + \Delta E_{\text{surf}}, \quad (4)$$

where  $\Delta E_{\text{bulk}}(\sigma_i \longrightarrow -\sigma_i)$  and  $\Delta E_{\text{surf}}(-\sigma_i \longrightarrow \sigma_i)$  are the changes in energy upon atom exchange in the bulk and at the surface, respectively. Note that the distribution  $\rho(E_{at})$  is (a) constant in time (because the contribution of fluctuations in the thermostat can be neglected) and (b) independent of the surface configuration (because the bulk is much larger in size than the surface,  $N_{\text{bulk}} \gg N_{\text{surf}}$ ).

When applying the above technique of atom exchange between the bulk “reservoir” and the surface to practical calculations, one can actually use a reservoir with the number of atoms  $N \sim 10^3$ – $10^5$ , which, by the order of magnitude, is equal to the number of atoms in the surface calculation, and, thus, the condition

$N_{\text{bulk}} \gg N_{\text{surf}}$  is not fulfilled. Nevertheless, this bulk reservoir can be used if the distribution function of atoms over energies in the reservoir  $\rho_{\text{res}}(E_{at})$  is close to the bulk (with  $N \rightarrow \infty$ ) distribution function  $\rho(E_{at})$  and, in addition, the following conditions are fulfilled for the function  $\rho_{\text{res}}(E_{at})$ : it is (a) constant in time and (b) independent of the surface configuration. This idea is at the basis of the proposed method.

The scheme of the algorithm of the surface MC method is shown in the panel in Fig. 1.

The simulation of surface segregations by the new MC method is accomplished as follows: the bulk MC calculation is performed for the temperature  $T$ , and, after attaining the thermodynamically equilibrium state, the bulk configuration of atoms is retained as a reservoir for the surface MC simulation. Next, the surface MC calculation is performed at the same temperature  $T$ ; in this calculation, the atom exchange between the surface and the bulk reservoir is treated according to the algorithm described above. In the surface MC calculation, periodic boundary conditions are imposed only in the directions perpendicular to the surface plane. Several atomic layers of the bulk MC sample parallel to the surface plane were used as a boundary between surface and bulk. Bulk periodic boundary conditions were employed (if necessary) for increasing the area of these layers so that they covered the whole bulk–surface boundary. The calculation went on until

the total surface energy  $E_{\text{surf}}^{\text{tot}}$  became stable. Unlike the method proposed in [11, 12], the new method requires only one preliminary bulk calculation for a given temperature. The method can be generalized without substantial changes to the case of a multicomponent alloy; in this case, only one preliminary bulk calculation is also necessary.

With the aim to illustrate the application of the new MC method to the problem of simulation of surface segregations in real systems, we carried out a calculation of the equilibrium segregation profile at the (100), (110), and (111) surfaces of the  $\text{Ni}_{50}\text{Pd}_{50}$  alloy.

The method used in this work for the calculation of effective potentials was described in detail in [8, 9]. Effective potentials were considered renormalized in the first three layers of the (100) and (111) surfaces and in the first four layers of the (110) surface; in deeper layers, the bulk values were used for effective potentials. For the  $\text{Ni}_{50}\text{Pd}_{50}$  system, effective many-body potentials were found to be very small (about several kelvin) and, hence, were not included in MC calculations. Pair potentials were included up to the fourth coordination sphere.

The bulk reservoir was generated using the bulk MC calculation; in this case, the sample was a cell with linear size  $L = 32$  atoms (of a total of  $L^3 = 32768$  atoms located at the fcc lattice sites). A random distribution of Ni and Pd atoms was the initial configuration at a temperature of 1500 K. Next, temperature  $T$  was lowered

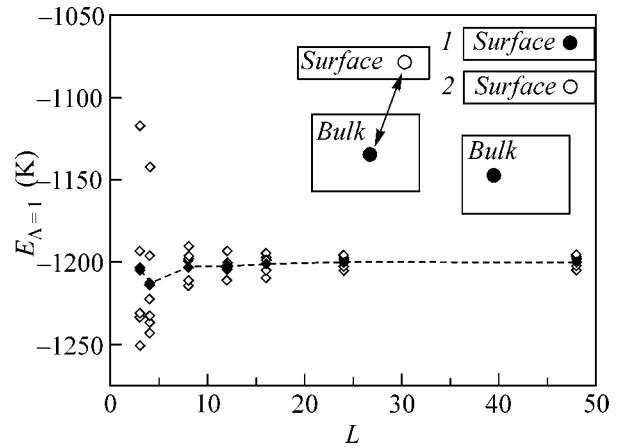


**Fig. 1.** Total energy per atom in the first layer at the (100) surface of the  $\text{Ni}_{50}\text{Pd}_{50}$  alloy versus linear size of the bulk reservoir  $L$ . Results are presented for several random configurations of the bulk reservoir. The dashed line is drawn through the values averaged over reservoir configurations. Panel: algorithm of the surface MC method. Calculation of the change in energy  $\Delta E$  upon exchanging atoms of different sorts chosen at random at the surface and in the bulk reservoir. If the exchange is accepted, the atom sort is changed only at the surface. To the right, two possible surface configurations after the surface MC step are shown: the type of atom at the surface (1) was changed and (2) was not changed. Configuration in the bulk reservoir remains unchanged.

with a step of 50 to 400 K, 5000 MC steps per atom (tries at exchanging atom pairs) were performed at each temperature, and the total energy and the short-range order parameters were averaged over the last 1000 steps. The equilibrium bulk configuration at each  $T$  was stored as a bulk reservoir for the subsequent use in the surface MC calculation.

In the MC calculations at the (100) and (111) surfaces, we used cells with a surface area of  $32 \times 32$  atoms and a thickness of 28 atomic layers, whereas for the (110) surface the thickness of the cell was increased to 40 atomic layers and the surface area was decreased to  $28 \times 28$  atoms. Temperature ranges and the number of steps at the surface were the same as in the bulk.

The calculated bulk pair effective potentials at the first to fourth coordination spheres of the fcc lattice were 279.00, 0.34,  $-9.95$ , and  $-12.59$  K, respectively. The bulk MC calculation involving the local relaxation effect has demonstrated that the long-range order is absent in the alloy down to the temperature 400 K, in agreement with the bulk phase diagram of the Ni–Pd system [17]. The calculated surface effective potentials (2) for the  $\text{Ni}_{50}\text{Pd}_{50}$  system are presented in the table. The value of the one-body potential at the surface  $V_{\lambda}^{(1)}$  is given with reference to the one-body bulk potential  $V_{\text{bulk}}^{(1)}$ . The table also presents the pair potentials at the first coordination sphere  $V_{\lambda\lambda'}^{(2,1)}$  multiplied by the num-

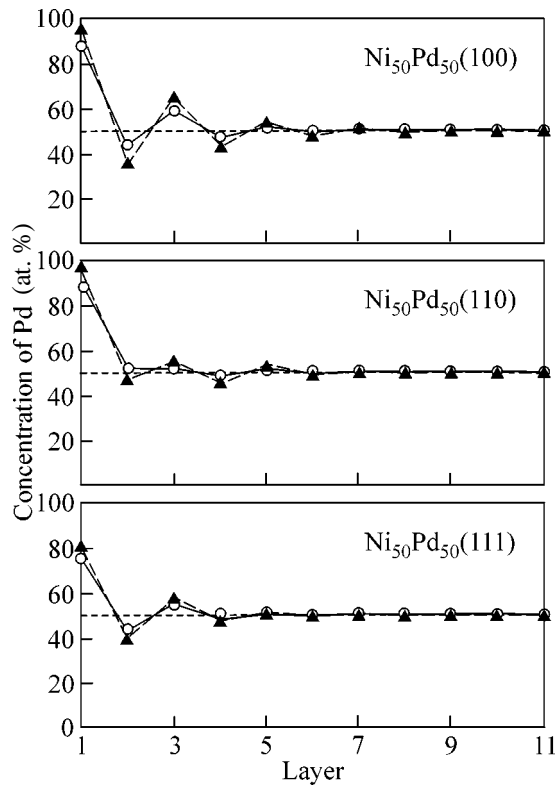


**Fig. 2.** Calculated surface segregation profiles at temperatures 1000 (solid line) and 600 K (dashed line) at the (100), (110), and (111) surfaces of the  $\text{Ni}_{50}\text{Pd}_{50}$  alloy.

ber of corresponding clusters  $Z_{\lambda\lambda'}^{(2,1)}$  per surface atom. In our calculations,  $\sigma = 1$  corresponds to the Pd atom, and  $\sigma = -1$  corresponds to the Ni atom.

Before calculating the segregation profile, we carried out several tests with the aim to examine the influence of the size of bulk reservoir on the surface results.

The segregations at the (100) surface of  $\text{Ni}_{50}\text{Pd}_{50}$  were calculated using several instantaneous configurations of reservoirs with linear sizes  $L = 3, 4, 8, 12, 16, 24,$  and  $48$ . Figure 1 presents the resulting total energies per atom in the first layer  $E_{\lambda=1}$  at a temperature of 600 K for seven random configurations of reservoirs for each  $L$  value. Obviously, the scatter of  $E_{\lambda=1}$  decreases rapidly with increasing  $L$ ; it is no larger than 20 K for  $L \geq 8$ , and the corresponding scatter of concentrations in the first layer is less than 1 at. %. Thus, one can state that at  $L \leq 8$  the instantaneous configurations of the reservoir are quite close to equilibrium.

The segregation profiles of the (100), (110), and (111) surfaces at temperatures 1000 and 600 K are presented in Fig. 2. The root-mean-square deviation of concentrations in layers, as calculated for the last 1000 steps per atom, is no larger than 1.5 at. %. The strong segregation of palladium to the surface layer is due to the sign of one-body potential  $V_1^{(1)} - V_{\text{bulk}}^{(1)}$ ; the largest segregation amplitude for the (110) surface and the smallest segregation amplitude for the (111) surface are also in agreement with the largest absolute value of the one-body potential  $V_1^{(1)} - V_{\text{bulk}}^{(1)}$  at the (110) surface and its smallest absolute value at the (111) surface. The segregation of Pd into the second layer at the (110) surface is nearly absent, although it was expected to occur on the basis of the analysis of one-body potentials. This is so because of a strong tendency to interlayer ordering at the (110) surface. In the situation when the surface layer contains nearly pure palladium, the pair interactions will favor the segregation of nickel into the sub-surface layer, thus acting against the one-body potential  $V_2^{(1)} - V_{\text{bulk}}^{(1)}$ . A decrease in temperature to 600 K enhances concentration oscillations, especially, at the (100) surface; at the other surfaces, oscillations are

Effective one-body and pair potentials (in K) for the (100), (110), and (111) surfaces of the  $\text{Ni}_{50}\text{Pd}_{50}$  alloy

Layers $\lambda$		1	2	3	4	5
(100)	$V_{\lambda}^{(1)} - V_{\text{bulk}}^{(1)}$	-1389.19	-197.67	-157.56	0.0	-
	$Z_{\lambda\lambda}^{(2,1)} V_{\lambda\lambda}^{(2,1)}$	446.28	583.60	585.31	557.99	-
	$Z_{\lambda\lambda+1}^{(2,1)} V_{\lambda\lambda+1}^{(2,1)}$	1085.19	1176.34	1115.99	1115.99	-
(110)	$V_{\lambda}^{(1)} - V_{\text{bulk}}^{(1)}$	-1612.88	-647.59	-126.03	35.41	0.0
	$Z_{\lambda\lambda}^{(2,1)} V_{\lambda\lambda}^{(2,1)}$	223.74	262.41	279.31	280.08	279.00
	$Z_{\lambda\lambda+1}^{(2,1)} V_{\lambda\lambda+1}^{(2,1)}$	1016.66	1097.45	1132.03	1115.99	1115.99
	$Z_{\lambda\lambda+2}^{(2,1)} V_{\lambda\lambda+2}^{(2,1)}$	260.55	295.70	279.00	279.00	279.00
(111)	$V_{\lambda}^{(1)} - V_{\text{bulk}}^{(1)}$	-1117.93	2.30	-60.31	0.0	-
	$Z_{\lambda\lambda}^{(2,1)} V_{\lambda\lambda}^{(2,1)}$	819.59	854.22	870.64	836.99	-
	$Z_{\lambda\lambda+1}^{(2,1)} V_{\lambda\lambda+1}^{(2,1)}$	920.53	861.35	836.99	836.99	-

smoothed either because of the presence of a negative one-body potential in the second layer for the (110) surface or due to relatively weak interlayer interactions for the (111) surface.

The calculated segregation profiles at the (100) surface are in qualitative agreement with the experiment [14]. The segregation profiles at the (110) and (111) surfaces of the Ni<sub>50</sub>Pd<sub>50</sub> alloy were not measured. Experiments were performed at the (110) and (111) surfaces of the Ni<sub>92</sub>Pd<sub>8</sub> alloy [15], where, similarly to our calculations, a higher concentration of palladium was observed at the (110) surface, as compared to the (111) surface. On the whole, the calculations of surface segregations in the Ni<sub>50</sub>Pd<sub>50</sub> alloy by the new surface MC method yield reasonable results that are in good agreement with previous studies of this system [14, 15, 16].

This work was supported by the Swedish Foundation for International Cooperation in Research and Higher Education (STINT), the Swedish Royal Academy of Sciences (KVA), and the Russian Foundation for Basic Research. We are grateful to É. Isaev for assistance in the preparation of the article.

#### REFERENCES

1. T. T. Tsong, *Phys. Today* **46** (5), 24 (1993).
2. I. A. Abrikosov and H. L. Skriver, *Phys. Rev. B* **47**, 16532 (1993).
3. A. V. Ruban and H. L. Skriver, *Comput. Mater. Sci.* **15**, 119 (1999).
4. H. L. Skriver and N. M. Rosengaard, *Phys. Rev. B* **46**, 7157 (1992).
5. J. M. Sánchez, F. Ducastelle, and D. Gratias, *Physica A (Amsterdam)* **128**, 334 (1984).
6. A. V. Ruban, I. A. Abrikosov, D. Ya. Kats, *et al.*, *Phys. Rev. B* **49**, 11383 (1994).
7. A. Pasturel, V. Drchal, J. Kudrnovský, and P. Weinberger, *Phys. Rev. B* **48**, 2704 (1993).
8. L. V. Pourovskii, A. V. Ruban, I. A. Abrikosov, *et al.*, *Phys. Rev. B* (in press).
9. A. V. Ruban and H. L. Skriver, *Phys. Rev. B* (in press).
10. K. S. Lee, S. H. Kim, H. G. Min, *et al.*, *Surf. Sci.* **377–379**, 918 (1997).
11. S. M. Foiles, *Phys. Rev. B* **32**, 7685 (1985).
12. D. Udler and D. N. Seidman, *Acta Metall. Mater.* **42**, 1959 (1994).
13. *Monte Carlo Methods in Statistical Physics*, Ed. by K. Binder (Springer-Verlag, Berlin, 1979; Mir, Moscow, 1982).
14. G. N. Derry, C. B. McVey, and B. J. Rous, *Surf. Sci.* **326**, 59 (1995).
15. A. C. Michel, L. Lianos, J. L. Rousset, *et al.*, *Surf. Sci.* **416**, 288 (1998).
16. A. Cristensen, A. V. Ruban, and H. L. Skriver, *Surf. Sci.* **383**, 235 (1997).
17. R. Hultgren, P. D. Desal, D. T. Hawkins, *et al.*, *Selected Values of the Thermodynamic Properties of Binary Alloys* (American Society of Metals, Metals Park, 1973).

*Translated by A. Safonov*

## S–N–D Corner Junctions in Magnetic Field

Yu. S. Barash and A. M. Bobkov

*Lebedev Physical Institute, Russian Academy of Sciences, Moscow, 117924 Russia*

*e-mail: bobkov@lpi.ru*

Received March 7, 2001; in final form, March 14, 2001

The dependence of the critical current of a highly transparent S–N–D corner junction on the applied magnetic field is determined for different orientations of a *d*-wave superconductor relative to the interface plane. It is shown that this dependence exhibits characteristic plateaus in a certain range of magnetic fields at low temperatures. These plateaus do not appear in the S–N–S corner junctions, indicating the presence of a superconductor with a sign-variable order parameter. © 2001 MAIK “Nauka/Interperiodica”.

PACS numbers: 74.50.+r; 74.80.Fp

The experimental studies of S–I–D (isotropic superconductor–insulator–*d*-wave superconductor) corner tunneling junctions in a magnetic field provide strong evidence for a sign-variable order parameter corresponding (at least approximately) to the *d*-wave pairing in high- $T_c$  superconductors [1–4]. This method proves to be less sensitive to the effects of magnetic flux capture and sample asymmetry than the experiments with corner-type SQUIDs [1, 5]. In the absence of a magnetic field, the Josephson critical current  $I_c$  in an S–I–D corner tunneling junction has a minimum (in an ideal case, it becomes zero), whereas, in an S–I–S tunneling junction, the quantity  $I_c$  has a maximum in zero magnetic field. This fact was used as the key feature for the identification of *d*-wave superconductors on the basis of the aforementioned method [1–4]. Its explanation lies in the mutual compensation of the two contributions of different sign from the two sides of the corner in an S–I–D tunneling junction to the Josephson current in the absence of a magnetic field. In the case of an S–I–S corner junction, these currents in the absence of a magnetic field are in phase, and when they add together, the resulting current becomes twice as great in the case of a symmetric junction. However, the aforementioned compensation occurs only in the tunneling limit, and, for junctions with a sufficiently large transparency, it does not take place. In junctions with high transparency, the dependence of the Josephson current on the phase difference  $\varphi$  is essentially nonsinusoidal (contains higher harmonics), and, as a result, one obtains  $j_s(\varphi + \pi) \neq -j_s(\varphi)$ . In this connection, it is of interest to consider the corner junctions with high transparency and to study their behavior in the presence of a *d*-wave superconductor.

In this paper, we consider totally transparent S–N–D (isotropic superconductor–normal-metal interlayer–*d*-wave superconductor) corner junctions with the width of the pure normal metal layer  $d \gg \xi_0$  (Fig. 1). We

determine the critical current for such systems in the presence of an external magnetic field. We show that, at sufficiently low temperatures, the presence of a plateau in a certain interval of magnetic fields is the characteristic feature of the interference dependences of critical current on magnetic field in corner junctions with high transparency. The plateau is most pronounced in the characteristics of S–N–D corner junctions with the (100) and (010) orientations of the boundary of the *d*-wave superconductor. As the temperature increases, the plateau is distorted and then disappears. For the (110) boundary orientation, the plateau is absent, including the case  $T = 0$ . In this case, as one would

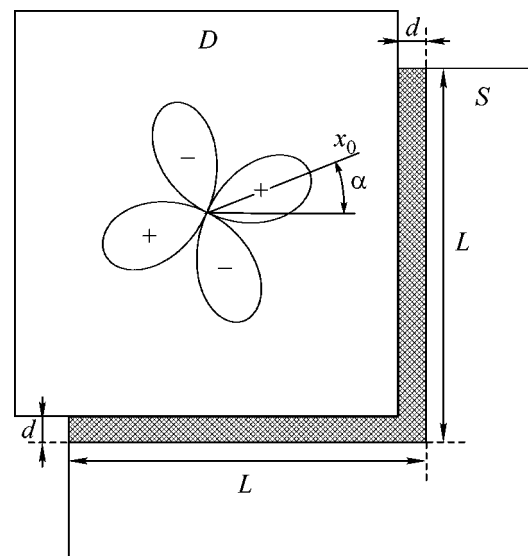


**Fig. 1.** Schematic representation of the corner junction under study. The magnetic field is directed normally to the plane of the figure;  $\alpha$  is the angle between the  $x_0$  axis of the superconductor with  $d_{x^2-y^2}$  pairing (D) and the normal to the boundary.

expect, the minima (zeros, in the ideal case) of the interference dependence of the critical current on magnetic field occur with a period half as large as in the case of an S-N-S junction.

Let two pure superconductors with singlet order parameters  $\Delta_l(\mathbf{p}_f, l)$  and  $\Delta_r(\mathbf{p}_f, r)$  occupy the regions  $x < -d/2$  and  $x > d/2$ , respectively, and the region  $-d/2 < x < d/2$  be occupied by a normal metal. To solve the Eilenberger equations for quasiclassical retarded Green's functions,

$$\begin{aligned} (2\omega + i v_{f,x} \partial_x) f(\mathbf{p}_f, x, \omega) \\ + 2\Delta(\mathbf{p}_f, x) g(\mathbf{p}_f, x, \omega) = 0, \\ (2\omega - i v_{f,x} \partial_x) f^+(\mathbf{p}_f, x, \omega) \\ - 2\Delta^*(\mathbf{p}_f, x) g(\mathbf{p}_f, x, \omega) = 0, \end{aligned} \quad (1)$$

$$\begin{aligned} i v_{f,x} \partial_x g(\mathbf{p}_f, x, \omega) - \Delta(\hat{\mathbf{p}}, x) f^+(\mathbf{p}_f, x, \omega) \\ - \Delta^*(\mathbf{p}_f, x) f(\mathbf{p}_f, x, \omega) = 0 \end{aligned}$$

with allowance made for the normalization condition

$$g^2 + f f^+ = -\pi^2, \quad (2)$$

we use the following ansatz, which automatically satisfies normalization condition (2):

$$\begin{aligned} f(\mathbf{p}_f, x, \omega) &= (-i\pi \operatorname{sgn}(x v_{f,x}) \\ &- g(\mathbf{p}_f, x, \omega)) e^{i\eta(\mathbf{p}_f, x, \omega)}, \\ f^+(\mathbf{p}_f, x, \omega) &= (-i\pi \operatorname{sgn}(x v_{f,x}) \\ &+ g(\mathbf{p}_f, x, \omega)) e^{-i\eta(\mathbf{p}_f, x, \omega)}. \end{aligned} \quad (3)$$

The substitution of Eqs. (3) into Eqs. (1) leads to an equation for the quantity  $\eta(\mathbf{p}_f, x, \omega)$

$$-\frac{v_{f,x}}{2} \partial_x \eta(\mathbf{p}_f, x, \omega) + \omega \quad (4)$$

$$-|\Delta(\mathbf{p}_f, x)| \cos(\eta(\mathbf{p}_f, x, \omega) - \phi(\mathbf{p}_f, x)) = 0$$

with the asymptotic conditions

$$v_{f,x} \sin(\eta_\infty(\mathbf{p}_f, \omega) - \phi_\infty(\mathbf{p}_f)) \operatorname{sgn} x > 0, \quad (5)$$

which provide the finiteness of the Green's function  $g(\mathbf{p}_f, x, \omega)$  when  $x \rightarrow \pm\infty$ . We do not present here the cumbersome explicit expression for the Green's function  $g(\mathbf{p}_f, x, \omega)$  in terms of  $\eta(\mathbf{p}_f, x, \omega)$ , which can be readily derived using the aforementioned substitution. In Eq. (4) and below, we introduce the magnitude and the phase of the order parameter:  $\Delta(\mathbf{p}_f, x) = |\Delta(\mathbf{p}_f, x)| e^{i\phi(\mathbf{p}_f, x)}$ .

For simplicity, we assume that the Fermi surfaces of the superconductors and the metal between them are identical. Then, we have the conventional boundary conditions for the Green's functions at the totally transparent boundaries:  $g_l(-d/2, \mathbf{p}_f) = g_N(\mathbf{p}_f) = g_r(d/2, \mathbf{p}_f)$ ,  $f_l(-d/2, \mathbf{p}_f) = f_N(-d/2, \mathbf{p}_f)$ , and  $f_N(d/2, \mathbf{p}_f) = f_r(d/2, \mathbf{p}_f)$ .

With these relationships, we obtain from Eqs. (3)–(5) the following expression for the temperature Green's function  $g_N^M(\mathbf{p}_f, \omega_n)$  in the region occupied by the normal metal:

$$\begin{aligned} g_N^M(\mathbf{p}_f, \omega_n) &= -i\pi \operatorname{sgn}(v_{f,x}) \\ &\times \coth \left[ i \frac{\eta(\mathbf{p}_f, d/2, \omega_n) - \eta(\mathbf{p}_f, -d/2, \omega_n)}{2} + \frac{\omega_n d}{v_{f,x}} \right]. \end{aligned} \quad (6)$$

This formula is valid for all temperatures and for a coordinate-dependent self-consistent profile of the order parameter  $\Delta(\mathbf{p}_f, x)$ . Neglecting the suppression of the order parameter, we obtain from Eqs. (4) and (5) in the low-temperature region  $T \ll \Delta_{\max}$ :  $\eta(\mathbf{p}_f, d/2, \omega_n) - \eta(\mathbf{p}_f, -d/2, \omega_n) = \phi(\mathbf{p}_f) + \pi \operatorname{sgn}(v_{f,x})$ , where  $\phi(\mathbf{p}_f) = \phi_r(\mathbf{p}_f) - \phi_l(\mathbf{p}_f)$  is the phase difference of the order parameters for a given momentum direction. In this approximation, the calculation of the Josephson current  $j_x$  with the use of the Green's function derived above leads to the following expression on condition that  $T \ll v_f/d \ll \Delta_{\max}$  [6, 7]:

$$j_x = \frac{e}{d} \int \frac{d^2 S}{(2\pi)^3 v_f} v_{f,x}^2 \operatorname{saw}(\phi(\mathbf{p}_f)). \quad (7)$$

Here, we introduced the sawtooth function  $\operatorname{saw}(\phi)$ :  $\operatorname{saw}(\phi) = \phi$  on the segment  $\phi \in [-\pi, \pi]$  and  $\operatorname{saw}(\phi + 2\pi) = \operatorname{saw}(\phi)$ . The condition  $v_f/d \ll \Delta_{\max}$  can be represented in the form  $\xi_0 \ll d$ , where  $\xi_0 = v_f/\Delta_{\max}$ .

Separating the constant phases  $\phi_{l,r}$  that do not depend on the momentum direction, we describe the superconductors by real sign-variable order parameters. In particular, this is possible for  $d$ -wave superconductors. Let us assume that  $S_f^+$  ( $S_f^-$ ) is the part of the Fermi surface  $S_f$  within which the order parameters  $\Delta_{l,r}(\mathbf{p}_f, 0)$  are of the same (opposite) sign. Then, denoting the constant phase difference by  $\phi = \phi_r - \phi_l$ , we obtain  $\phi(\mathbf{p}_f) = \phi$  for  $\mathbf{p}_f \in S_f^+$  and  $\phi(\mathbf{p}_f) = \phi + \pi$  for  $\mathbf{p}_f \in S_f^-$ . Now, we determine the quantities  $a^\pm$  by the expressions

$$a^\pm = \frac{A\{S_f^\pm\}}{A\{S_f\}}, \quad \text{where } A\{S_f^\pm\} = \int_{S_f^\pm} \frac{d^2 S_f v_{f,x}^2}{(2\pi)^3 v_f}, \quad (8)$$

and  $A\{S_f^-\}$  and  $A\{S_f\}$  are determined in a similar way.

Evidently, we have  $S_f^+ + S_f^- = S_f$ , which yields  $a^+ + a^- = 1$ . The quantities  $a^\pm$  strongly depend on the type of pairing and the mutual orientation of the superconducting crystals, as well as on the shape of the Fermi surface. At the same time, they are insensitive to the specific form of the basis functions of the corresponding point group representation of the superconducting crystal. For superconductors whose order parameters have constant

signs on the entire Fermi surface (an anisotropic  $s$  pairing), the quantities  $a^\pm$  take the values  $a^+ = 1$  and  $a^- = 0$  (or  $a^- = 1$  and  $a^+ = 0$  when the constant signs of the two order parameters are opposite).

Generally speaking, the problem on the current through a corner junction is two-dimensional. However, we will assume that the characteristic length of the junction  $L$  satisfies the conditions  $\lambda_{l,r} \ll L \ll \lambda_j$ , where  $\lambda_{l,r}$  and  $\lambda_j$  are the penetration depths of the magnetic field in the bulk superconductors and in the Josephson junction, respectively. Then, in magnetic fields  $H \ll H_{c1} \sim \Phi_0/\lambda_{l,r}^2$ , the magnetic flux through the corner-containing region with a characteristic area of the order of  $\lambda_{l,r}^2$  is much less than the flux quantum, and the problem can be approximately considered as one-dimensional. In this case, the self-magnetic field in the junction can be neglected.

In these conditions, we consider a planar junction in a magnetic field directed parallel to the  $S$ - $N$  boundary along the  $z$  axis. We assume that, along the  $y$  direction, the junction consists of two parts, which, in the one-dimensional problem under study, correspond to the two sides of the corner. As compared to the region  $0 < y < L$ , the quantity  $\pi$  should be added to the phase difference in the junction for each of the momentum direc-

tions in the region  $-L < y < 0$ . This takes into account the change of sign of the order parameter in the  $d$ -wave superconductor when the momentum of a quasiparticle is rotated through  $\pi/2$  about the  $z$  axis, which coincides with the tetragonal axis of the crystal. Below, by the term corner junction is meant such a one-dimensional model.

To take into account the effect of magnetic field  $H$  on the Josephson current, we use the substitution  $\phi(\mathbf{p}_f) \rightarrow \phi(\mathbf{p}_f) + (2eHy/c)(d + \lambda_l + \lambda_r)$  in Eq. (7), where  $d$  is the thickness of the normal metal interlayer and  $\lambda_{l,r}$  represents the penetration depths of the magnetic field in the left and right superconductors, respectively. The magnetic flux  $\Phi = 2HL(d + \lambda_l + \lambda_r)$  through the normal metal layer and the surface layers of the superconductors ( $2L$  is the length of the boundaries of the junction under study along the  $y$  axis) is conveniently measured in the flux quantum units  $n = \Phi/\Phi_0 \equiv |e|\Phi/\pi c$ . We assume that, in a small-size junction, both the current distribution along the field (along the  $z$  axis) and the magnetic field itself are homogeneous. Then, for the Josephson critical current in a common  $S$ - $N$ - $D$  planar junction, we obtain the same result as was reported in [8]. Calculating the total current through the  $S$ - $N$ - $D$  corner junction and determining its maximal values depending on the magnetic field, we arrive at the following relationships:

$$\frac{j_{c0}(H)}{j_{c0}(0)} = \frac{2}{n} \begin{cases} \left\{ \frac{n}{2} \right\} \max \left[ \left( 1 - 4 \left\{ \frac{n}{2} \right\} \right), |a^+ - a^-| \right], & \left\{ \frac{n}{2} \right\} \leq \frac{1}{4} \\ \max \left[ \left\{ \frac{n}{2} \right\} |a^+ - a^-|, \left( 4 \left\{ \frac{n}{2} \right\} - 1 \right) \left| a^\pm - \left\{ \frac{n}{2} \right\} \right| \right], & \frac{1}{4} \leq \left\{ \frac{n}{2} \right\} \leq \frac{1}{2} \\ \max \left[ \left( 1 - \left\{ \frac{n}{2} \right\} \right) |a^+ - a^-|, \left( 3 - 4 \left\{ \frac{n}{2} \right\} \right) \left| a^\pm - \left\{ \frac{n}{2} \right\} \right| \right], & \frac{1}{2} \leq \left\{ \frac{n}{2} \right\} \leq \frac{3}{4} \\ \left( 1 - \left\{ \frac{n}{2} \right\} \right) \max \left[ |a^+ - a^-|, \left( 4 \left\{ \frac{n}{2} \right\} - 3 \right) \right], & \frac{3}{4} \leq \left\{ \frac{n}{2} \right\} \leq 1. \end{cases} \quad (9)$$

Here,  $\{n/2\}$  is the fractional part of the magnetic flux through the corner junction on one of the two sides of the corner.

From Eqs. (9) and Fig. 2, one can see that, in the field region  $(1 - |a^+ - a^-|)/2 < n < \max(a^+, a^-)$ , the curve  $j_{c0}(H)$  has a plateau: the critical current is  $j_{c0}(0)|a^+ - a^-|$  and does not depend on the magnetic field. Since such plateaus never occur in the magnetic-field dependences of the critical current in  $S$ - $N$ - $S$  junctions [6, 9], their presence in the curves at low temperatures testifies that the junction contains a superconductor with a sign-variable order parameter.

Assuming that, the  $d_{x^2-y^2}$  pairing takes place in one of the superconductors and the  $z_0$  crystal axis of this superconductor is parallel to the junction plane, whereas the second superconductor is characterized by an isotropic  $s$  pairing, we obtain  $a^\pm = 1/2 \pm \cos 2\alpha/\pi$ , where  $\alpha$  is the angle between the  $x_0$  axis of the crystal and the normal to the  $S$ - $N$  boundary. In this case, the plateau is in the field interval  $(\pi - 2|\cos 2\alpha|)/2\pi < n < (\pi + 2|\cos 2\alpha|)/2\pi$  at the level  $2|\cos 2\alpha|/\pi$  of the critical current in zero field. For the orientation  $\alpha = 0$ , the plateau has the maximal length, and for  $\alpha = 45^\circ$  the plateau is absent. In the latter case,  $a^+ = a^- = 1/2$ . As in an ordinary

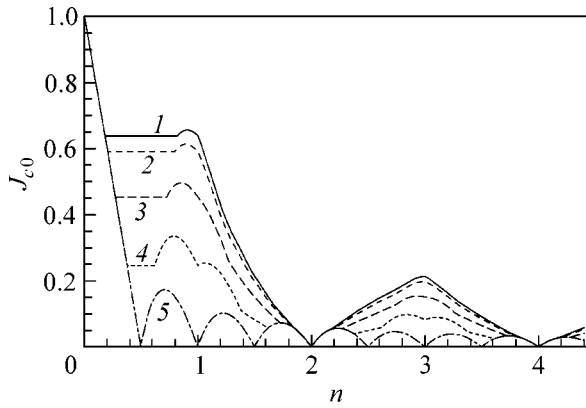


**Fig. 2.** Dependence of  $J_{c0} = j_{c0}(H)/j_{c0}(0)$  on  $n = \Phi/\Phi_0$  obtained from Eqs. (9) at zero temperature for different orientations of the superconductor with  $d_{x^2-y^2}$  pairing; the tetragonal axis of the superconductor is parallel to the magnetic field. The angle between the  $x_0$  axis of the crystal and the normal to the surface is  $\alpha = (1) 0, (2) \pi/16, (3) \pi/8, (4) 3\pi/16, (5) \pi/4$ . The plateau of maximal length corresponds to the (100) orientation.

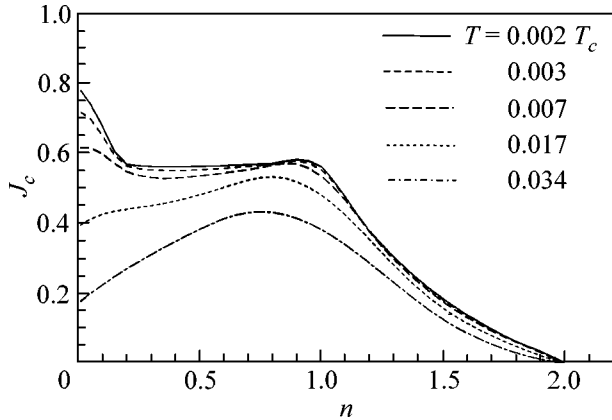


**Fig. 3.** Dependence of  $J_c = j_c(H)/j_{c0}(0)$  on  $n$  for an S-N-D corner junction with orientation  $\alpha = 0^\circ$  at different temperatures;  $\xi_0/d = 0.1$ .

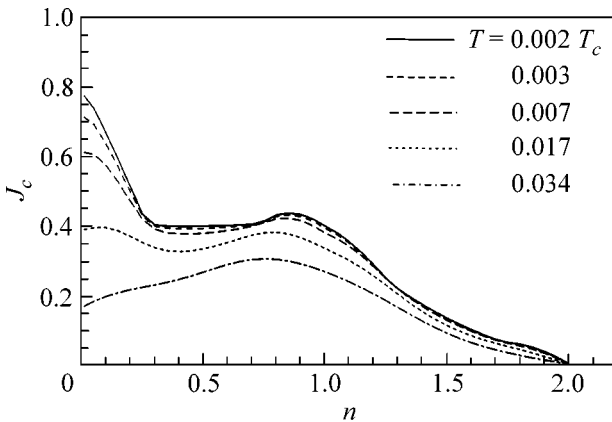


**Fig. 4.** Dependence of  $j_c(H)/j_{c0}(0)$  on  $n$  for the orientation  $\alpha = 22.5^\circ$  and for different temperatures;  $\xi_0/d = 0.1$ .

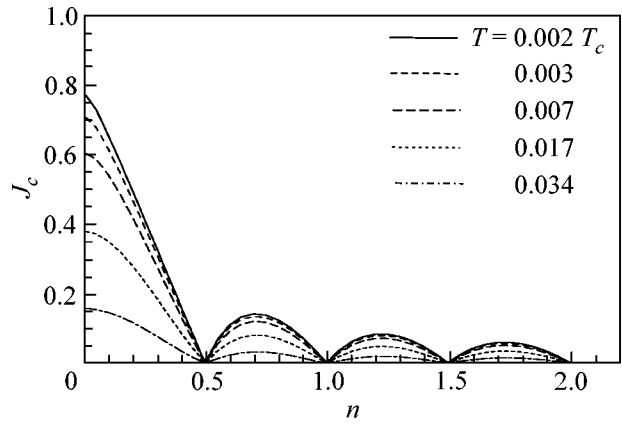


**Fig. 5.** Dependence of  $j_c(H)/j_{c0}(0)$  on  $n$  for the orientation  $\alpha = 45^\circ$  and for different temperatures;  $\xi_0/d = 0.1$ .

S-N-D planar junction [8], the critical current in the corner junction becomes zero at every half flux quantum ( $n = 0.5, 1, 1.5, \dots$ ), i.e., with a period two times shorter than usual. Such a behavior is caused by the specific symmetry of the problem at  $\alpha = 45^\circ$  and should manifest itself not only for metal but also for insulator interlayers [10].

The revealed characteristic behavior of the critical current of S-N-D corner junctions in a magnetic field, including, first of all, the presence of a plateau and linear dependences on the magnetic field, is closely related to the initial sawtooth dependence of the Josephson current on the phase difference in the systems under study [6, 7, 11]. As compared to an S-N-S junction, in an S-N-D junction the sawtooth dependence of the Josephson current on the phase difference is more complex, namely,  $j_x(\varphi) \neq j_x(-\varphi)$ , and a discontinuity occurs at  $\varphi = 0$ . Therefore, in the ground state of a superconducting ring containing an S-N-D junction, a spontaneous current is present [7]. The spontaneous current occurs along the surface of the S-N-D junction, and it is mainly localized in the interlayer [12, 13]. This current is screened by the Meissner currents arising in the superconductors. Generally speaking, in the presence of a spontaneous current, the appearance of a small asymmetry of the critical current with respect to the change of sign of the external field is possible. However, this fact does not introduce any significant changes in the main results obtained above for the dependence of the critical current on the external magnetic field.

The described behavior of the critical current is distorted with increasing temperature to the same extent as the aforementioned sawtooth dependence. Figures 3-5 show the dependences of the critical current of an S-N-D junction on the magnetic field for different temperatures and orientations of the superconductor with  $d$  pairing. The width of the normal metal interlayer is taken to be  $10\xi_0$ . The suppression of the order parameter near the transparent boundary is neglected. From these figures, one can see that, in the case of high- $T_c$  superconductors

with  $T_c \sim 100$  K, the appearance of the plateau characteristic of  $S$ - $N$ - $D$  corner junctions should be expected at temperatures about 0.1–0.5 K.

This work was supported by the Russian Foundation for Basic Research, project no. 99-02-17906.

#### REFERENCES

1. D. A. Wollman, D. J. van Harlingen, W. C. Lee, *et al.*, Phys. Rev. Lett. **71**, 2134 (1993).
2. D. A. Wollman, D. J. van Harlingen, J. Giapintzakis, and D. M. Ginzberg, Phys. Rev. Lett. **74**, 797 (1995).
3. D. J. van Harlingen, Rev. Mod. Phys. **67**, 515 (1995).
4. J. H. Miller, Jr., Q. Y. Ying, Z. G. Zou, *et al.*, Phys. Rev. Lett. **74**, 2347 (1995).
5. B. M. Hinaus, M. S. Rzchowski, N. Heinig, *et al.*, Phys. Rev. B **54**, 6770 (1996).
6. A. V. Svidzinskiĭ, *Space-Inhomogeneous Problems of Theory of Superconductivity* (Nauka, Moscow, 1982).
7. Yu. S. Barash, A. V. Galaktionov, and A. D. Zaikin, Phys. Rev. B **52**, 665 (1995).
8. A. M. Zagoskin, J. Phys.: Condens. Matter **9**, L419 (1997).
9. T. N. Antsygina, E. N. Bratus', and A. V. Svidzinskiĭ, Fiz. Nizk. Temp. **1**, 49 (1975) [Sov. J. Low Temp. Phys. **1**, 23 (1975)].
10. E. Il'ichev, V. Zakosarenko, R. P. J. Ijsselsteijn, *et al.*, Phys. Rev. B **60**, 3096 (1999).
11. C. Ishii, Prog. Theor. Phys. **44**, 1525 (1970).
12. A. Huck, Anne van Otterlo, and M. Sigrist, Phys. Rev. B **56**, 14163 (1997).
13. A. M. Zagoskin and M. Oshikawa, J. Phys.: Condens. Matter **10**, L105 (1998).

*Translated by E. Golyamina*

# Mechanism of Low-Temperature Ion-Bombardment-Activated Surface Self-Diffusion

T. I. Mazilova, I. M. Mikhailovskii, and E. V. Sadanov

National Scientific Center “Kharkov Physicotechnical Institute,” Kharkov, 61108 Ukraine

Received March 14, 2001

Elementary events of low-temperature surface erosion induced by the bombardment with accelerated helium atoms and ions were studied at the atomic level. It is established that the regular arrangement of surface atoms is disturbed due to the release of energy of formation of interstitial atoms emerging at the surface and to the expenditure of part of this energy on the formation of surface defects in excited states. The adatom excitation energy allowing the short-range diffusion processes was determined experimentally. © 2001 MAIK “Nauka/Interperiodica”.

PACS numbers: 68.49.Sf; 61.80.Jh; 66.30.Hs

In recent years, rapid development of nanotechniques has quickened interest in radiation-induced phenomena at solid surfaces. The studies of ion-bombardment-activated surface self-diffusion were first initiated in connection with the problem of high-voltage vacuum discharge and radiation resistance of field emitters [1, 2]. At present, this phenomenon has found wide use in developing methods of preparing chemically clean surfaces with minimum roughnesses; in analyzing the evolution of surface wall microtopography of thermoelectric devices subject to low-energy ion bombardment, in the activation of surface chemical reactions, and in the design of various systems with local ion or electron field emission [3–5]. It is known that, upon ion bombardment, the initially perfectly flat surface assumes atomic roughness which can be removed by low-temperature annealing. The annealing temperature is lowered because of the enhanced mobility of the radiation-induced adatoms [5, 6]. This work is devoted to studying the mechanism of adatom formation and the origin of high adatom mobility at low temperatures.

Experiments were carried out using a field ion microscope with samples cooled to 21–80 K. Helium at a pressure of  $10^{-2}$ – $10^{-3}$  Pa was used as an imaging gas. Needle-shaped samples with radius of curvature 20–100 nm were prepared from a tungsten wire of 99.98% purity by electrochemical etching. After mounting in the microscope, the samples were subjected to low-temperature field evaporation until an atomically flat surface was formed. The field strength necessary for the microscope operation was created by simultaneously feeding a dc voltage of 3–25 kV and an ac voltage of 4–15 kV to the sample. The ac voltage amplitude was chosen so that the field-emission current density lay in the range  $10^8$ – $10^{10}$  A/m<sup>2</sup>. The net current through the tips of needle-shaped samples was  $10^{-7}$ – $10^{-6}$  A.

The tips were bombarded by helium ions that were formed upon passing electron flow through the imaging gas. The bombardment intensity was determined from the relationships obtained in [7]. Those ions formed at a distance shorter than five radii of curvature  $R_0$  of the tip fell on the emitting surface from a conical region. For larger distances, the bombardment proceeded from a cylindrical region coaxial with the sample. The ion energy distribution was close to Maxwellian with a mean energy of  $eER_0$ , where  $e$  is the electron charge. The electric field during the process of ion bombardment was  $(3–5) \times 10^9$  V/m. The electric field strength was determined from the ratio of operating voltage to the threshold evaporation voltage for the tungsten face {110} at 21 K. The latter corresponds to an electric field of  $5.8 \times 10^{10}$  V/m. The average energy of the ion flow incident on the sample area under study was 150–500 eV; the fluence varied in the range  $10^8$ – $10^{20}$  ion/m<sup>2</sup>.

Field ion microscopy can be used to reveal the character of defect structure produced by ion bombardment. The phenomenon of controlled low-temperature field evaporation allows the layer-by-layer analysis of the defect distribution in depth under the sample surface. The location of point defects is usually determined from the disturbance of regular arrangement of surface atoms or from the appearance of points with enhanced brightness [8]. However, in most cases, one fails to distinguish between the contrasts produced by the subsurface point defects and adatoms. Therefore, the conventional method of interpreting point defects in field ion images cannot be applied to the microcrystal surfaces subjected to intense ion bombardment. With the aim of minimizing the uncertainty in the interpretation of surface point defects, part of the experiments were carried out using a two-chamber field ion microscope equipped with a source of monoenergetic helium atoms. The samples were bombarded with neutral helium atoms

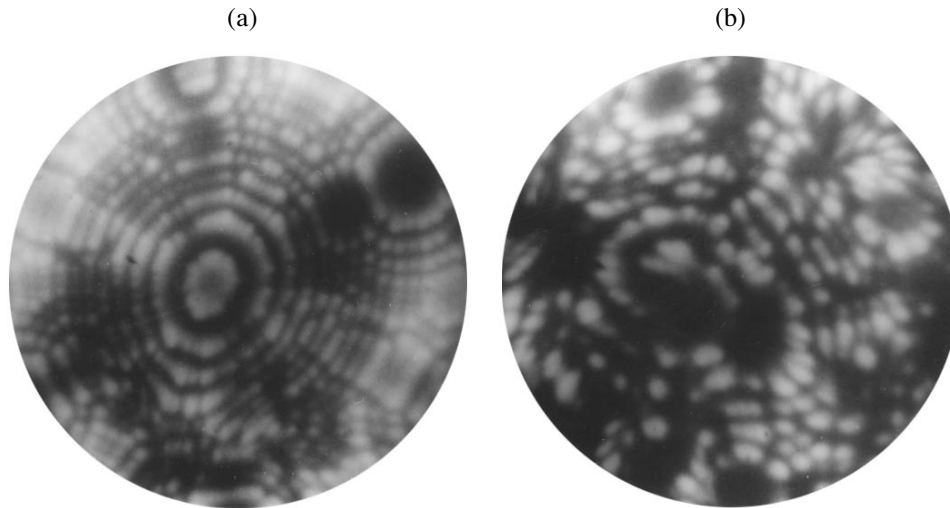


**Fig. 1.** Field ion microscopy images of the surface of tungsten microcrystals (a) before and (b) after the bombardment with helium ions with average energy 180 eV and fluence  $2 \times 10^{19}$  ion/m<sup>2</sup>.

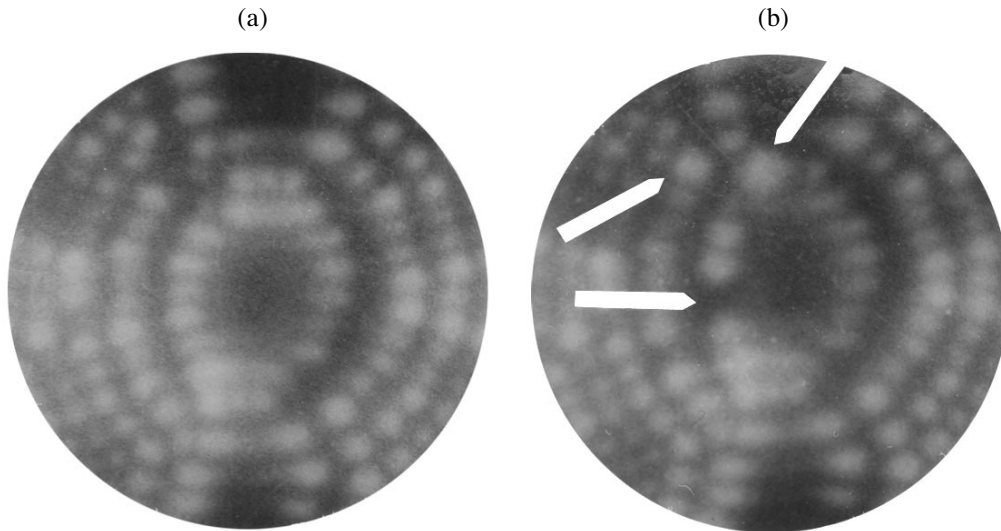
with an energy of 2–7 keV and a fluence of  $(5\text{--}20) \times 10^{15}$  atom/(m<sup>2</sup> s). The bombardment was accomplished in the direction perpendicular to the  $\langle 110 \rangle$  axis, which in most cases coincides with the sample axis. After completion of irradiation, the appearance of new emission centers was observed for 1–5 min at the surface areas not subjected to the bombardment.

Figure 1 demonstrates the ion microscopy images of a surface of tungsten single crystals before and after exposure to helium ions with an average energy of 180 eV and a fluence of  $2 \times 10^{19}$  ion/m<sup>2</sup> at a temperature of 70 K. The regular arrangement of the surface atoms contributing to the formation of the field emission image is disturbed by the ion bombardment. The configuration of atomic steps at the faces with low Miller indices is altered. In particular, the shape of the central face  $\{110\}$  in Fig. 1 changed substantially; the concentric steps (a) assumed a spiral shape (b) after the bombardment. The removal of a monolayer by controlled field evaporation almost completely recovered the regular atomic structure over the whole temperature range studied (21–80 K). The direct field ion microscopy observations indicate that in the absence of ion bombardment the surface atoms at all faces are immobile at temperatures as low as those. In this connection, the character of observed changes in the microtopography suggests that the main contribution to the change of shape comes from low-temperature radiation-stimulated surface migration.

With the aim of elucidating the atomic mechanism of the radiation-stimulated surface self-diffusion, a source of accelerated helium atoms was used. Since the neutral atoms do not deflect in the electric field of the samples, the possibility exists of examining the elementary events of surface erosion. Figure 2 shows the

ion microscopy images of the nonirradiated (dark) surface area of the single crystal before (a) and after (b) exposure to the helium atoms with an energy of 7 keV and a fluence of  $3 \times 10^{16}$  atom/m<sup>2</sup> in an electric field of  $3 \times 10^{10}$  V/m. Analysis of the radiation-induced changes in the surface morphology suggests that, apart from the single adatoms, the defect complexes of the type “surface vacancy–pair of adatoms” also make a sizable contribution to the disturbance of regular arrangement of surface atoms. For instance, the distances between the radiation-induced surface vacancy and adatoms (marked by arrows in Fig. 2b) are 2.6 and 2.8 nm. For visual monitoring, the formation of this group of surface point defects is perceived as simultaneous. The distances between the correlated radiation-induced surface point defects did not depend on the energy of incident helium atoms and lay in the range 2–6 nm. The formation of single adatoms and correlated pairs was observed directly in the field ion microscope both in the course of irradiation and for 1–5 min after switching off the source of accelerated helium atoms. This provides evidence for the nondynamic character of the surface damage process. In the temperature range studied, only the interstitial tungsten atoms are mobile [9]. One can thus conclude that the formation of adatoms and correlated pairs after switching off the source of accelerated atoms is the result of the diffusion of radiation-induced interstitial atoms to the surface.

The number of new emission centers formed upon irradiation depends on the electric field strength at the sample. For an electric field weaker than  $4.9 \times 10^{10}$  V/m, the density of emission centers was approximately equal to the density in the absence of a field. With increasing field strength to  $(4.9\text{--}5.3) \times 10^{10}$  V/m in the vicinity of the  $\{211\}$  face, the surface density of the



**Fig. 2.** Field ion microscopy images of the {211} face of a microcrystal (a) before and (b) after the bombardment with helium atoms with average energy 7 keV and fluence  $3 \times 10^{16}$  atom/m<sup>2</sup>. Arrows indicate the surface point defects.

emission centers newly formed during the course of bombardment and immediately after switching off the source of accelerated helium atoms drops by two orders of magnitude. These values are appreciably smaller than the threshold evaporation field of the ground-state surface atoms at the {211} face at 21 K ( $6.38 \times 10^{10}$  V/m). This indicates that the release of energy of formation of interstitial atoms emerging at the surface is accompanied by the formation of surface defects in the excited state.

The desorption field  $F$  for the atoms occurring in the excited state immediately after they overcome the barrier is different from the desorption field for the atoms relaxed to the ground state at the same surface sites. To determine the threshold evaporation field for the ground-state surface atoms, the bombardment with neutral helium atoms was performed at  $F = 0$ , after which the positive potential was raised until the bright emission centers disappeared. It turned out that the ground-state atoms can be removed from the {211} face only in rather high fields  $F = (5.5\text{--}5.9) \times 10^{10}$  V/m.

The difference between the threshold evaporation fields for the excited-state ( $F_e$ ) and ground-state ( $F_0$ ) atoms was observed not only during the bombardment but also after switching off the ion source. This, in particular, points to the fact that the displacements of surface atoms were of nondynamic nature. In the temperature range studied (21–80 K), the interstitial tungsten atoms are the only mobile radiation distortions. As the interstitial atom executes diffusion to the surface, the energy of formation  $E_i^f$  decreases because of the action of image forces. However, a decrease in energy is of the same order as the activation energy  $E_i^m$  for migration of interstitial atoms [10] and, hence, is appreciably lower

than  $E_i^f$ . One can thus conclude that the energy released by the interstitial atoms emerging at the surface is close to the total energy of formation  $E_i^f$ . The energy of formation of the interstitial tungsten atom (4.7–4.9 eV [9, 10]) is considerably higher than the energy necessary for displacing surface atoms to the adsorption state. As a result, the displaced surface atom may occur in the excited state and, hence, reduce the desorption field. Within the image force model [8], the excitation energy of the displaced surface atom is determined by the difference between the evaporation fields for the ground-state and excited-state atoms

$$\Delta E_e = (ne)^{3/2} (F_0^{1/2} - F_e^{1/2}).$$

In this expression,  $n$  is the ion multiplicity. At low temperatures, tungsten is evaporated as three- and fourfold ionized atoms. A barrier produced by the image forces is the highest for the quadrivalent ions. By setting  $n = 4$ , one obtains  $\Delta E_e = 3.9$  eV for the maximum excitation energy of the displaced surface atom. Thus, the fact that the evaporation fields for the atoms in the nascent adsorption state and in the relaxed state are different is evidence that the atoms in the adsorption state bear an excess energy. The lifetime of the excited-state atom is comparable with the characteristic time of nonactivation field evaporation. The excess energy of the adatoms in this state permits short-range surface diffusion with characteristic diffusion length on the order of the distance between the point defects in the correlated pairs.

We are grateful to A.S. Bakař and V.I. Gerasimenko for discussion and E.I. Lugovskaya for assistance in experiments.

## REFERENCES

1. Zh. I. Dranova and I. M. Mikhaïlovskii, *Fiz. Met. Metalloved.* **31**, 1108 (1971).
2. J. Y. Cavaille and M. Drechsler, *Surf. Sci.* **75**, 342 (1978).
3. T. I. Mazilova, *Zh. Tekh. Fiz.* **70** (2), 102 (2000) [*Tech. Phys.* **45**, 243 (2000)].
4. S. N. Magonov and M. H. Whangbo, *Surface Analysis with STM and AFM* (Springer-Verlag, Berlin, 1996).
5. A. Knoblauch, Ch. Miller, and S. Kalbitzer, *Nucl. Instrum. Methods Phys. Res. B* **139**, 20 (1998).
6. V. I. Gerasimenko, Zh. I. Dranova, and I. M. Mikhaïlovskii, *Fiz. Tverd. Tela (Leningrad)* **25**, 2456 (1983) [*Sov. Phys. Solid State* **25**, 1410 (1983)].
7. P. A. Bereznyak and V. V. Slezov, *Radiotekh. Élektron.* **2**, 354 (1972).
8. M. K. Miller, A. Cerezo, M. G. Hetherington, and G. D. W. Smith, *Atom Probe Field Ion Microscopy* (Clarendon Press, Oxford, 1996).
9. V. V. Kirsanov, A. L. Suvorov, and Yu. V. Trushin, *Formation of Radiation Defects in Metals* (Énergoatomizdat, Moscow, 1985).
10. V. I. Gerasimenko, T. I. Mazilova, I. M. Mikhaïlovskii, and E. V. Sadanov, *Pis'ma Zh. Éksp. Teor. Fiz.* **59**, 323 (1994) [*JETP Lett.* **59**, 344 (1994)].

*Translated by V. Sakun*

# Superconductivity of $\kappa$ -(BEDT-TTF)<sub>2</sub>Cu[N(CN)<sub>2</sub>]I Under Pressure<sup>1</sup>

N. D. Kushch<sup>1,2</sup>, M. A. Tanatar<sup>3,4,5</sup>, E. B. Yagubskii<sup>1</sup>, T. Ishiguro<sup>3,4</sup>

<sup>1</sup> Institute of Problems of Chemical Physics, Russian Academy of Sciences,  
Chernogolovka, Moscow region, 142432 Russia

<sup>2</sup> Walther-Meissner-Institut, D-85748 Garching, Germany

<sup>3</sup> Department of Physics, Kyoto University, Kyoto 606-8502, Japan  
e-mail: tanatar@scphys.kyoto-u.ac.jp

<sup>4</sup> CREST, Japan Science and Technology Corporation, Kawaguchi, Saitama 332-0012, Japan

<sup>5</sup> Institute of Surface Chemistry, National Academy of Sciences of Ukraine, 03164 Kiev, Ukraine  
Received March 19, 2001

The insulating state of  $\kappa$ -(BEDT-TTF)<sub>2</sub>Cu[N(CN)<sub>2</sub>]I salt appearing at ambient pressure at low temperatures is suppressed by hydrostatic pressure. The resistive measurements showed that the emerging metallic state reveals superconductivity in high-quality crystals. The superconducting state with the transition temperature of about 8 K is stable at pressures higher than 0.1 GPa. © 2001 MAIK "Nauka/Interperiodica".

PACS numbers: 74.62.Fj; 74.10.+v; 74.70.Kn

The  $\kappa$ -(BEDT-TTF)<sub>2</sub>Cu[N(CN)<sub>2</sub>]X salts, with X standing for halogen atoms Cl, Br, and I (in what follows, we designate salts according to their X as Cl, Br, and I), form a homologous series of compounds [1]. All three salts are isostructural at room temperature and possess metallic electronic structure, according to band structure calculation [2]. In reality, the ground states of the salts are drastically different. The Cl and Br salts are the highest  $T_c$  quasi-two-dimensional organic superconductors under hydrostatic (X = Cl,  $T_c$  = 12.8 K at 0.03 GPa) and ambient (X = Br,  $T_c$  = 11.6 K) pressure, respectively. The third member of the family, I salt, is an insulator at low temperatures and ambient pressure, similar to Cl salt, but does not undergo superconducting transition under hydrostatic pressure up to 0.5 GPa [1]. For I salt, however, traces of a superconducting phase with a  $T_c$  of about 8 K were found in the modulated microwave absorption experiments [3, 4]. Since the volume fraction of these inclusions increases upon prolonged annealing of the crystals [3], it was assumed that they represent an impurity phase of  $\beta_H$ -(BEDT-TTF)<sub>2</sub>I<sub>3</sub> that is formed due to the thermolysis of  $\kappa$ -(BEDT-TTF)<sub>2</sub>Cu[N(CN)<sub>2</sub>]I.

In order to understand the mechanism of formation of the insulating state, we have recently studied the electronic transport properties and X-ray diffuse scattering in I salt [5]. We have found that the high-temperature metallic state of I salt is in agreement with the band structure calculation, while the insulating state is

formed as a result of the structural transformation due to ordering of the terminal ethylene groups in the BEDT-TTF molecules.

The studies of mixed Br–Cl salts [6] and Br–I salts [7] indeed showed a correlation between the electronic properties and the conformational disorder in the crystals [8]. Simultaneously, it was found that the degree of conformational order may be influenced by the method of sample preparation. A similar effect of the crystal growth procedure on the conformational state of the BEDT-TTF molecule in lattice was first reported for  $\beta$  phases [9]. This effect may also be important for closely related  $\kappa$ -(BEDT-TTF)<sub>2</sub>Cu(NCS)<sub>2</sub>, for which the growth conditions strongly influence the temperature dependence of resistivity [10–13]. Since the electrochemical synthesis of I salt is not easy, the typical crystals (in what follows we call them standard crystals) are of a rather low quality. This difficulty of sample preparation is the main reason why the studies of I compound are scarce compared to the Cl and Br salts. Therefore, we considered the growth of high-quality single crystals of  $\kappa$ -(BEDT-TTF)<sub>2</sub>Cu[N(CN)<sub>2</sub>]I to be our important goal.

In this letter, we report observation of superconductivity in high-quality crystals of I salt under moderate hydrostatic pressures of about 0.1 GPa. This observation shows that the superconducting properties of the compound are in line with the other members of the  $\kappa$ -(BEDT-TTF)<sub>2</sub>Cu[N(CN)<sub>2</sub>]X family. The transition temperature for I salt, as determined from resistive measurements, is ~8 K. A small value of the critical pressure required for inducing superconductivity

<sup>1</sup> This article was submitted by the authors in English.

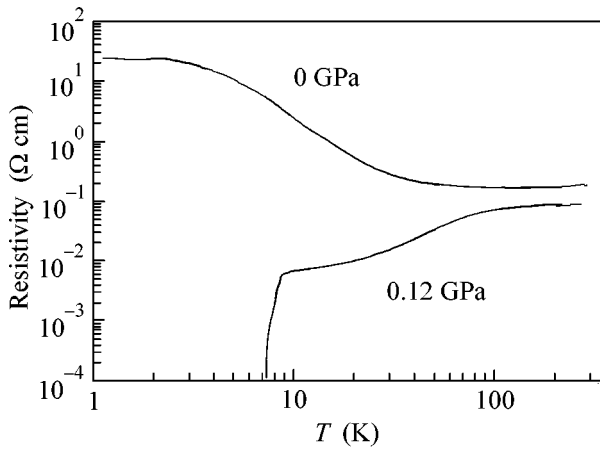


**Fig. 1.** Temperature dependence of resistivity for sample 1 at ambient pressure and under a pressure of 0.12 GPa.

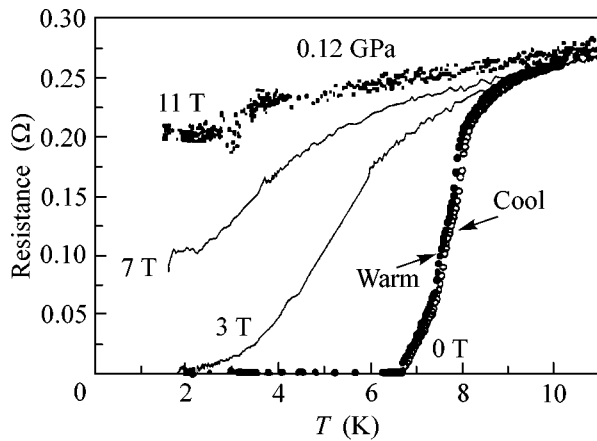


**Fig. 2.** Temperature dependence of resistance for sample 1 under a hydrostatic pressure of 0.12 GPa in the vicinity of the superconducting transition as a function of magnetic field applied in the arbitrary direction with respect to the sample.

allows us to reinterpret previously observed superconducting inclusions in the salt [3, 4] as intrinsic and caused by local strains.

The crystals of  $\kappa$ -(BEDT-TTF)<sub>2</sub>Cu[N(CN)<sub>2</sub>]I were synthesized by electrochemical oxidation of BEDT-TTF in a 1,1,2-trichloroethane medium. A mixture of (PPh<sub>4</sub>)[N(CN)<sub>2</sub>] and CuI was used as an electrolyte. Starting salts used for the preparation of the electrolyte were of high purity and did not contain the Cl or Br anions as adulterants.<sup>2</sup> The typical current density was 3–5  $\mu$ A/cm<sup>2</sup>. The current density was reduced approximately twice after the nucleation of the crystals on the Pt electrode. The growth was carried out for a period of 3 to 4 weeks. Below, we refer to the crystals obtained by this route as “new crystals.” The resultant new crys-

<sup>2</sup> The absence of Cl and Br impurities was confirmed by electron probe microanalysis of the crystals.

tals had usual shapes of a rhombus or a distorted hexagon; however, contrary to the standard samples, they were free of layered defects [5]. Two crystals studied had sizes  $0.5 \times 0.5 \times 0.1$  mm and  $0.6 \times 0.5 \times 0.12$  mm. The resistance of the samples was measured by the standard four-probe technique with a current flowing along the highly conducting *ac* plane. All four terminals were attached to the same sample surface. Measurements under quasi-hydrostatic pressure were performed in a beryllium copper clamp pressure cell with silicon oil as a pressure medium. A pressure of up to 0.4 GPa was applied at room temperature. The pressure at low temperatures was calculated using the results [14]. The in-plane resistance of the sample was found to decrease by a factor of 2 on loading from 0 to 0.4 GPa; no special features that could be attributed to phase transitions under pressure were detected.

In Fig. 1, we show the temperature dependence of resistivity at ambient pressure and under a pressure of 0.12 GPa on a log–log scale. At ambient pressure, the resistivity decreases upon cooling from room temperature to 60 ~ 80 K (depending on the sample) and then shows a notable increase at low temperatures. It is worth noting that no resistivity decrease was found at ambient pressure down to 1.1 K. Under a pressure of 0.12 GPa, the sample shows a resistive transition into the superconducting state with the onset of transition at 8.2 K, midpoint at 7.7 K, and zero-resistivity state being achieved at 6.8 K (see expanded view in Fig. 2). To confirm the superconducting nature of this behavior, we show in Fig. 2 the temperature dependence of resistivity in the vicinity of the superconducting transition in magnetic fields of different strength.

In order to understand the striking difference between our results and those previously reported for this compound, it is instructive to compare the properties of the two different sets of crystals with each other. Both crystals were studied by X-ray analysis and were found to be isostructural at room temperature. The elemental composition of the crystals was studied using the electron probe microanalysis technique, and no deviation from the chemical formula was found within the accuracy of the method. Besides, the ESR spectra of the new crystals were typical for  $\kappa$ -phase salts [3]. They show no detectable inclusions of the  $\beta$  phase possessing notably different ESR spectrum.

A slight difference in the properties of the two sets of I crystals suggests that the main effect comes from the improved quality of the new samples. Although the temperature dependence of resistivity for the new crystals is basically similar to that of the standard crystals [1, 5, 15], some small differences should be noticed. In the standard samples, the resistivity starts to increase just below ~200 K, although this increase is very small down to 70 K. In addition, the overall resistance increase on cooling to 1.2 K in the standard samples (amounting to ~1000 times the room-temperature value) is notably higher than in the new samples (200

to 500 times). Since both of the above-mentioned features in the standard samples are due to disorder [2, 5], we conclude that the new crystals are characterized by a much higher degree of ordering at low temperature.

As can be seen from Fig. 1, on applying pressure, the temperature dependence of resistance changes in a way very similar to that observed for Cl salt [16]. A resistivity maximum appears, signaling ethylene reordering taking place under pressure [17]. It is known that the resistance of Cl and Br salts is sensitive to thermal cycling, mainly in 50 to 100 K range [15, 17], because of the proximity to structural instability [18]. For the standard I salt, this sensitivity is very small, indicating much higher lattice stability. In the samples under study, the resistance hysteresis has almost the same magnitude as in Cl salt. This finding shows that the samples are characterized by a soft lattice prone to the structural transformation into the superconducting phase.

In conclusion, high-quality single crystals of I salt show a clear superconducting transition under pressure, in contrast to the previous reports on this compound. This finding demonstrates the crucial importance of crystal perfection for the occurrence of superconductivity in this family of materials.

This work was supported by the NWO (grant no. FN4359), the Russian Foundation for Basic Research (project no. 00-02-04019DFG\_a), and by the CREST, Japan Science and Technology Corporation.

#### REFERENCES

1. H. H. Wang, K. D. Carlson, U. Geiser, *et al.*, *Synth. Met.* **42**, 1983 (1991).
2. U. Geiser, A. J. Shultz, H. H. Wang, *et al.*, *Physica C (Amsterdam)* **174**, 475 (1991).
3. V. Kataev, G. Winkel, N. Knauf, *et al.*, *Physica B (Amsterdam)* **179**, 24 (1992).
4. H. S. Lee, D. O. Cowan, R. Fainchtein, *et al.*, *Bull. Am. Phys. Soc.* **41**, 15 (1996).
5. M. A. Tanatar, S. Kagoshima, T. Ishiguro, *et al.*, *Phys. Rev. B* **62**, 15561 (2000).
6. N. D. Kushch, L. I. Buravov, A. G. Khomenko, *et al.*, *Synth. Met.* **53**, 155 (1993).
7. N. D. Kushch, L. I. Buravov, A. G. Khomenko, *et al.*, *Synth. Met.* **72**, 181 (1995).
8. R. P. Shibaeva, S. S. Khasanov, N. D. Kushch, *et al.*, in *Supramolecular Engineering of Synthetic Metallic Materials, Conductors and Magnets*, Ed. by J. Veciana, C. Rovira, and D. B. Amabilino (Kluwer, Dordrecht, 1999), NATO ASI Ser., Ser. C **518**, 409 (1999).
9. R. P. Shibaeva, E. B. Yagubskii, E. E. Laukhina, and V. N. Laukhin, in *Physics and Chemistry of Organic Superconductors*, Ed. by G. Saito and S. Kagoshima (Springer-Verlag, Berlin, 1990), p. 342.
10. L. I. Buravov, A. V. Zvarykina, N. D. Kushch, *et al.*, *Zh. Éksp. Teor. Fiz.* **95**, 322 (1989) [*Sov. Phys. JETP* **68**, 182 (1989)].
11. H. Mori, S. Tanaka, H. Yamochi, *et al.*, in *Physics and Chemistry of Organic Superconductors*, Ed. by G. Saito and S. Kagoshima (Springer-Verlag, Berlin, 1990), p. 150.
12. H. Anzai, T. Itoh, N. Kinoshita, *et al.*, *J. Cryst. Growth* **141**, 119 (1994).
13. H. Muller, C.-P. Heidmann, D. Kellner, *et al.*, *Synth. Met.* **39**, 261 (1990).
14. J. D. Thompson, *Rev. Sci. Instrum.* **55**, 231 (1984).
15. K. Andres, H. Posselt, N. D. Kushch, *et al.*, *Acta Phys. Pol. A* **87**, 761 (1995).
16. J. E. Schirber, D. L. Overmyer, K. D. Carlson, *et al.*, *Phys. Rev. B* **44**, 4666 (1991); Yu. V. Sushko, V. A. Bondarenko, R. A. Petrosov, *et al.*, *J. Phys. II* **1**, 1015 (1991); H. Ito, T. Ishiguro, M. Kubota, *et al.*, *J. Phys. Soc. Jpn.* **65**, 2987 (1996).
17. M. A. Tanatar, T. Ishiguro, T. Kondo, and G. Saito, *Phys. Rev. B* **59**, 3841 (1999).
18. T. Ishiguro and M. A. Tanatar, in *Studies of High Temperature Superconductors (Advances in Research and Applications)*, Ed. A. Narlikar (Nova Science, Com-mack, 2000), Vol. 34, p. 55.

## Explosive Ice Instability

E. G. Fateev

*Institute of Applied Mechanics, Ural Division, Russian Academy of Sciences, Izhevsk, 426001 Russia*

*e-mail: fateev@ipm.uni.udm.ru; e@fateev.udm.ru*

Received January 25, 2001; in final form, March 21, 2001

Explosive ice instability under strong uniaxial compression at high pressures is observed over a wide temperature range from 244 K down to 100 K. The critical dependence of the threshold instability pressure on temperature in the region of expected *Ih–II* and *IX–VI* transitions displays features with minima. It is conjectured that explosive instabilities may occur on cosmic bodies such as the Jupiter satellites Europa and Ganymede. © 2001 MAIK “Nauka/Interperiodica”.

PACS numbers: 62.50.+p; 64.70.Kb; 96.35.-j

The problem of explosive ice instability attracts interest because of the discovery of many-kilometer glacial shells on some satellites of big planets in the solar system [1, 2]. Estimates show [3] that the ice crust on the Jupiter satellites Europa and Ganymede may be as deep as 100–150 km. Moreover, when it is considered that these satellites are covered by a network of giant cracks [4], then it becomes clear that a body of ice crust contains vast compression areas where conditions are far from hydrostatic. It is believed that, in conjunction with open boundaries, these conditions can generate giant explosive instabilities in the depths of ice crust. As is well known, such instabilities (Bridgman effect) can be excited in the laboratory for many solid insulators through slow uniaxial compression at a rate  $dP/dt < 0.1$  GPa/s at high pressures ( $P < 20$  GPa) between anvils with open boundaries [5–13]. This effect is accompanied by shock waves and high-speed ( $v \sim 0.5$ – $2$  km/s) ejection of a destructed microdispersed substance beyond the compression system. This phenomenon evolves when the elastic energy of a strongly compressed body converts into mechanical work, resulting in an ultrahigh-speed volume relief after the system has reached certain critical  $P$ – $T$  parameters [9, 10]. The possible pressure-induced phase and polymorphic transitions in solid insulators can reduce substantially the excitation threshold for such explosion phenomena [10]. Note also that the explosion effect is accompanied by energetic electromagnetic radiation over a wide spectral range up to the X-ray range [8] and by electron emission [9]. The  $P_c$  threshold (or the average critical pressure inducing the Bridgman effect in a substance) decreases with increasing temperature and compression rate [11]; it correlates with the parameters of the substance and shows size dependence [10]. It was also established that a weak ultralow-frequency electric field influences the threshold  $P_c$  in crystal hydrates [12, 13].

In this work, a direct experiment was conducted to demonstrate that a strongly compressed ice may exhibit

explosive instability over a wide temperature range. Bridgman anvils with gaskets made from superhard VK-8 alloy and shaped like a truncated cone with a working area of diameter  $d = 10$  mm were used in the experiment. The loading rate for uniaxial compression was fixed at  $dP/dt \approx 0.02$  GPa/s. The temperature near the sample was measured by a Cu–Copel thermocouple whose junction was brought immediately to the sample edge. At the first (preliminary) step, the anvils were cooled directly by liquid nitrogen to a temperature of 230–240 K. Then, a batch of distilled water was poured as a thin layer onto the working area of one of the anvils and moulded into a thin ice disk of thickness  $d \approx 0.4$  mm through lightly pressurizing the solidifying water with a dielectric sheet. At the second step, the ice disk on the anvil could be cooled down to any required temperature in the range from 273 to 100 K. The cooling rate was  $dT/dt \sim (5$ – $10)$  K/s. There seems to be no other feasible way of obtaining an ice disk that would have standard thickness and could be pressurized between anvils at any temperature.

Inasmuch as statistically significant values of excitation threshold  $P_c$  can be obtained only by conducting many experimental runs at a fixed temperature  $T$ , the required  $T$  was achieved in the following way. The anvils were cooled together with the sample down to a temperature slightly lower than the required one. Then the system was put under a press, where, after attaining the required temperature and on a slight natural heating at a rate  $dT/dt \approx 0.01$  K/s, the compression procedure began and lasted up to the occurrence of the explosive instability.

The experimental results are presented in the figure, where each point was obtained in ten experiments with explosive instabilities. One can see from the figure that the ice instability occurs practically over the whole temperature range studied. Baric ice explosion was observed only at temperatures  $T \leq 244$  K, while above

this limiting value a plastic extrusion of ice from the anvils was observed.

In the remaining temperature range, the critical conditions  $P_c(T)$  for explosive instability do not obey any certain law. For instance, one could expect that the  $P_c(T)$  dependence would obey the empirical rule  $\log(P_c) \approx A \log(T) + B$  in the low-temperature range, with  $A = -5.35$  and  $B = 28.9$  for ice, as was earlier observed in [10] for ordinary compounds. However, this rule is fulfilled more or less satisfactorily only in the interval from 144 to 244 K. At  $T < 144$  K, the critical dependence has quite a different character. It should be noted that the standard deviation from the mean threshold value does not exceed  $\sim 10\%$  in the range from 196 to 244 K, whereas at  $T < 196$  K the deviations are as large as  $\sim 25\%$ . In the temperature range 206–218 K, the critical curve displays a feature with a minimum at  $T \approx 211$  K.

Earlier, it was shown in [10] that the initial destruction processes in the volume, which eventually initiate the Bridgman effect, to a first approximation can be rationalized in terms of the theory of thermal fluctuations [14]. The temperature dependence  $P_c(T)$  obtained for the ice instability threshold in this work is no exception. No doubt, ice may contain various microinhomogeneities just before the explosion effect, as usually occurs upon strong compression of ice [15]. Evidently, the initial microfractures in a strongly compressed ice start with rupturing hydrogen bonds in the microvolumes that are mechanically loosened by lattice defects. This implies that the critical curve  $P_c(T)$  can, in principle, be used to derive a certain curve that correlates with the temperature dependence of hydrogen bond energy in ice in these microvolumes. It is quite logical to assume that the temperature dependence of hydrogen bond energy in the defect microvolumes correlates with the analogous dependence in the defect-free volume. As is well known, it is hard to obtain such a dependence by other experimental methods or by model calculations. This can be judged if only from a large scatter of temperature curves obtained for the ice sublimation energy in different models [16].

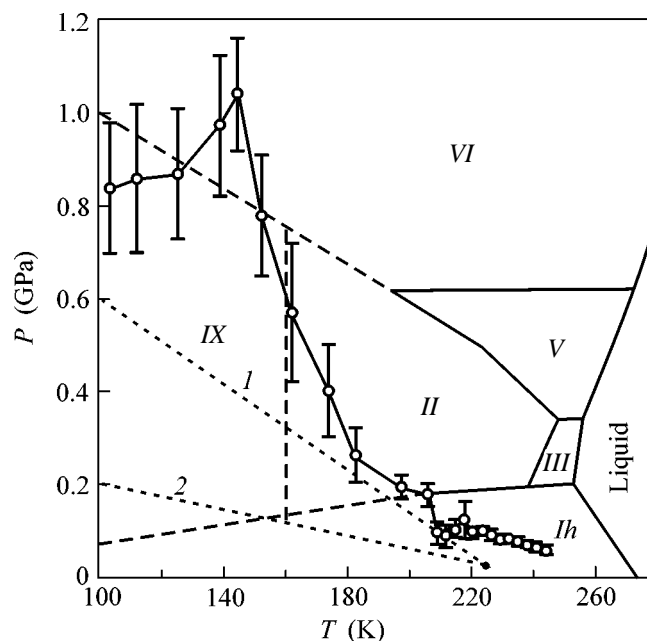
Let us determine the threshold rupture stress using the following relationship of the theory of thermal fluctuations [14]:

$$\sigma = \gamma^{-1} [U_0 - kT \ln(\tau/\tau_0)], \quad (1)$$

where

$$\gamma = V\sigma_l/\sigma. \quad (2)$$

Here,  $T$  is the temperature,  $k$  is the Boltzmann constant,  $U_0$  is the initial interatomic bond dissociation energy,  $\tau_0 \sim 10^{-13}$  s is the period of interatomic thermal vibrations,  $\tau$  is the expectation time for the critical nucleus appearance,  $\gamma$  is a structure-sensitive multiplier,  $V \approx a^3$  is the activation volume,  $\sigma_l$  is the local stress in the fracture nucleus, and  $a$  is the interatomic distance. Notice that the parameters  $\sigma$ ,  $\gamma$ ,  $U_0$ , and  $\tau$  may depend on pres-



Critical temperature dependence of the ice explosive instability threshold ( $\circ$ ) and the known [34, 35] ice equilibrium phase diagram. The regions of metastable phases in the equilibrium diagram are shown by the dashed lines. The dotted lines 1 and 2 corresponding to the  $Ih$ - $hda$  and  $Ia$ - $hda$  transitions in the metastable  $P$ - $T$  ice phase diagram with a critical point at  $T \sim 225$  K and  $P \sim 0.03$  GPa [28–30].

sure. However, the accuracy of the results obtained from Eq. (1) is limited because the character of the  $P$  dependence is not known with certainty for these parameters. Nevertheless, it is known [17] that the breaking radial stress  $\sigma$  in the disk between the Bridgman anvils correlates with the average pressure at any distance from the disk center,

$$\sigma \propto \xi P, \quad (3)$$

where parameter  $\xi$  weakly changes with compression. Let us assume that the activation volume coincides with the volume of a molecular unit cell in water. Assuming  $\tau$  to be pressure-independent, one obtains the correlation relationship for the hydrogen bond energy in the form

$$U_H \propto \gamma \xi P + kT \ln(\tau/\tau_0), \quad (4)$$

where  $\tau$  and  $\gamma$  can be estimated from the known (see, e.g., [16, 18–20]) value  $U_H \sim 0.5$  eV  $\approx 8 \times 10^{-20}$  J/(hydrogen bond) for ice I at  $240 < T < 273$  K and  $P = 0$ . One has  $\tau \sim 2 \times 10^{-3}$  s. For  $\xi \sim 1$  and temperatures from  $T = 100$  K to  $T = 273$  K and  $P \sim 0.1$  GPa, one obtains  $\gamma \sim 10^{-28} - 10^{-27}$  m<sup>3</sup>. In the range of moderate pressures below  $P \sim 1.5$  GPa, the latter value may prove to be 30–45% smaller by virtue of the multiplication coefficient [7, 17, 21]  $M = \sigma_z/P \sim 2-3$  and corresponding axial stress  $\sigma_z \sim 3-4.5$  GPa in the disk between the anvils for the ice isothermal compressibility  $\sim 10^{-10}$  Pa<sup>-1</sup> [22].

Then, one finds from Eq. (2) that the local stresses in the fracture microvolume may exceed the stresses in the multiplication zone by a factor of 3–15. Such a considerable local overstresses may evolve at the preexplosion stage of ice compression because of the parametric onset of oscillations in the system of hydrogen-bonded water molecules [23]. Hence, it is assumed that the temperature dependence of the critical hydrogen bond energy, Eq. (4), can correlate with the  $P_c(T)$  dependence. One can expect that the energy will increase from  $U_H \approx 0.5$  eV to  $U_H \approx 1.8$  eV at the maximum at  $T \approx 145$  K.

The following features of the  $P_c(T)$  curve are noteworthy. The local minimum in the range of temperatures 206–218 K and critical pressures 0.1–0.2 GPa can naturally be assigned to the phase transition from polycrystalline ice *Ih* to phase *II*. This transition can be expected to occur in the indicated region, as follows from the equilibrium phase diagram of ice, where the critical curve  $P_c(T)$  is also plotted (figure). This feature is likely evidence for a strong (by ~50–70%) weakening of the lattice bonds during the process of phase transition. Accordingly, the bond strengths in the range 100–140 K at critical pressures 0.8–1.1 GPa are, apparently, affected by the *IX–VI* phase transition, during which the bonds also weaken by ~50–70%. This estimate of the relative hydrogen bond weakening is consistent with the relevant theoretical assumption [24].

A slight discordance between the phase-transition curves and the coordinates of the above-mentioned minima on the critical curve  $P_c(T)$  in the ice phase diagram is probably due to the following reasons. In practice, pressure is distributed nonuniformly along the diameter of Bridgman anvils [7, 17, 21]. For this reason, the explosive ice instability is most likely activated in the regions where the pressure is approximately twice its critical threshold value  $P_c$ , as follows from the ratio of pressures corresponding to the *Ih–II* phase transition and to the  $P_c(T)$  curve at the minimum at  $T \approx 212$  K (figure). For the second phase transition, the critical curve  $P_c(T)$  intersects the phase equilibrium curve in the metastability region at  $T \sim 100$ –140 K and critical pressures  $P_c \approx 0.8$ –1.1 GPa, where the phase equilibrium curve is rather conventional. The authors of [28–30] have used recent experimental data [25–27] to construct the metastable ice diagram, which is drawn in the figure as two dotted lines labeled 1 and 2 and intersecting with each other at the critical point  $T \approx 225$  K and  $P \approx 0.03$  GPa. One can see that the local minimum in the  $P_c(T)$  curve coincides with the phase equilibrium curve *lda–hda*. There is evidence that the ice structure in the vicinity of this phase transition may be unstable [15, 31, 32]. However, taking into account the pressure multiplication in the Bridgman anvils and the fact that the  $P_c(T)$  curve goes almost parallel to the equilibrium curve *lda–hda* over a rather wide range of temperatures from 180 to 225 K and drops only in the narrow interval from 206 to 218 K, one can conclude that this drop for

disk thicknesses  $h \leq 0.4$  mm is most likely unrelated to the phase transitions of the *lda–hda* type.

The critical dependence  $P_c(T)$  is obtained in this work only for the disk thickness  $h \approx 0.4$  mm. However, the critical parameters  $P_c(T)$  for larger sizes must be smaller because of the well-known size effect [11]. The corresponding change can be estimated from the dependence of the multiplication coefficient  $M$  on the ratio  $d/h$  [17]. For example, with a decrease in the  $d/h$  ratio from 25 (this work) to 10, the critical pressure is expected to decrease also by a factor of 2–3 over the whole  $P_c(T)$  dependence. Because of this, the features with minima in the region of phase equilibria may undergo an appreciable shift to lower temperatures. The resultant shifted  $P_c(T)$  curve may be affected by the phase transitions of the *lda–hda* type to a much greater extent.

It follows from the experiments described in this work that the explosive instability may, in principle, take place on cosmic bodies of the Europa and Ganymede type. Ice crusts in these Jupiter satellites have thicknesses up to  $h \sim 150$  km (at free fall acceleration  $g \sim 1.5$  m<sup>2</sup>/s). It is quite possible that their temperatures and pressures lie in the ranges  $130 < T < 273$  K and  $0 < P < 0.25$  GPa [33], respectively, which is sufficient for the occurrence of the explosion effects considered in this work.

In summary, explosive ice instability induced by strong uniaxial compression has been observed in this work experimentally over wide temperature and pressure ranges. The corresponding dependence of the instability critical pressure on temperature is found to display features with minima in the regions of ice phase transitions. It is assumed that this dependence correlates with the corresponding temperature dependence of hydrogen bond strength in ice. The phase transitions in ice may result in an additional (by ~50–70%) decrease in the mechanical stability of ice.

I am grateful to Yu.I. Prokhorov for useful discussions.

## REFERENCES

1. D. Morrison and D. P. Cruikshank, *Space Sci. Rev.* **15**, 641 (1974).
2. J. D. Anderson, E. L. Lau, W. L. Sjorgen, *et al.*, *Science* **276**, 1236 (1997).
3. M. H. Carr, M. J. Belton, C. R. Chapman, *et al.*, *Nature* **391**, 363 (1998).
4. R. Sullivan, R. Greeley, K. Homan, *et al.*, *Nature* **391**, 371 (1998).
5. P. W. Bridgman, *Phys. Rev.* **48**, 825 (1935).
6. P. W. Bridgman, *Proc. Am. Acad. Arts Sci.* **71**, 9 (1937); **71**, 387 (1937).
7. P. W. Bridgman, *Studies in Large Plastic Flow and Fracture with Special Emphasis on the Effects of Hydrostatic Pressure* (McGraw-Hill, New York, 1952).

8. T. Ya. Gorazdovskii, Pis'ma Zh. Éksp. Teor. Fiz. **5**, 78 (1967) [JETP Lett. **5**, 64 (1967)].
9. M. A. Yaroslavskii, *Rheological Explosion* (Nauka, Moscow, 1982).
10. E. G. Fateev and V. P. Khan, Pis'ma Zh. Tekh. Fiz. **17** (20), 52 (1991) [Sov. Tech. Phys. Lett. **17**, 736 (1991)].
11. N. S. Enikolopyan, A. A. Khzardzhyan, É. É. Gasparyan, *et al.*, Dokl. Akad. Nauk SSSR **294**, 1151 (1987).
12. E. G. Fateev, Dokl. Akad. Nauk **354**, 252 (1997).
13. E. G. Fateev, Pis'ma Zh. Éksp. Teor. Fiz. **65**, 876 (1997) [JETP Lett. **65**, 919 (1997)].
14. S. N. Zhurkov, Fiz. Tverd. Tela (Leningrad) **25** (10), 3119 (1983) [Sov. Phys. Solid State **25**, 1797 (1983)].
15. O. V. Stal'gorova, E. L. Gromnitskaya, and V. V. Brazhkin, Zh. Éksp. Teor. Fiz. **112**, 1 (1997) [JETP **85**, 109 (1997)].
16. D. R. Hamann, Phys. Rev. B **55**, R10157 (1997).
17. V. I. Levitas, *Large Elastoplastic Deformations of Materials at High Pressures* (Naukova Dumka, Kiev, 1987).
18. J. D. Bernal and R. H. Fowler, J. Chem. Phys. **1**, 515 (1933).
19. M. Weissman and N. V. Cohan, J. Chem. Phys. **43**, 119 (1965).
20. L. Pauling, *The Nature of the Chemical Bond* (Cornell Univ., Ithaca, 1960, 3rd ed.), p. 468.
21. J. Prins, High Temp.-High Press. **15**, 21 (1983).
22. A. J. Leadbetter, Proc. R. Soc. London, Ser. A **205**, 155 (1965).
23. A. A. Kusov, Fiz. Tverd. Tela (Leningrad) **21**, 3095 (1979) [Sov. Phys. Solid State **21**, 1781 (1979)].
24. J. Koike, Phys. Rev. B **47**, 7700 (1993).
25. O. Mishima, L. D. Calvert, and E. Whalley, Nature **310**, 393 (1984).
26. O. Mishima, L. D. Calvert, and E. Whalley, Nature **314**, 76 (1985).
27. O. Mishima, L. D. Calvert, and E. Whalley, J. Chem. Phys. **84**, 2766 (1986).
28. P. H. Pool, U. Essmann, F. Scortino, *et al.*, Phys. Rev. E **48**, 4605 (1993).
29. H. E. Stanley, C. A. Angel, U. Essmann, *et al.*, Physica A (Amsterdam) **205**, 122 (1994).
30. E. G. Ponyatovskii, V. V. Sinitsyn, and T. A. Pozdnyakova, Pis'ma Zh. Éksp. Teor. Fiz. **60**, 352 (1994) [JETP Lett. **60**, 360 (1994)].
31. O. V. Stal'gorova, E. L. Gromnitskaya, and V. V. Brazhkin, Pis'ma Zh. Éksp. Teor. Fiz. **62**, 334 (1995) [JETP Lett. **62**, 356 (1995)].
32. J. M. Besson, S. Klotz, G. Hamel, *et al.*, Phys. Rev. Lett. **78**, 3141 (1997).
33. R. T. Pappalardo, J. W. Head, R. Greeley, *et al.*, Nature **391**, 365 (1998).
34. P. W. Bridgman, J. Chem. Phys. **3**, 597 (1935).
35. C. Lobban, J. L. Finney, and W. F. Kuhs, Nature **391**, 268 (1998).

*Translated by V. Sakun*